Growth of Spinel Oxide Thin Films for High Efficiency Room Temperature Spin Filtering

Salvatore Mesoraca

Hughes Hall, University of Cambridge

A dissertation submitted for the degree of Doctor of Philosophy

at the University of Cambridge

December 2017

Declaration

I hereby declare that this dissertation, submitted for the Degree of Doctor of Philosophy at the University of Cambridge, is a result of my own work carried out in the Device Materials Group, Department of materials science and metallurgy, University of Cambridge, under the supervision of Prof. Mark Blamire since September 2013. The dissertation includes nothing which is the outcome of work done in collaboration except as specified and referenced in the text.

It is not substantially the same as any that I have submitted, or, is being concurrently submitted for a degree or diploma or other qualification at the University of Cambridge or any other University or similar institution. I further state that no part of my dissertation has already been submitted, or, is being concurrently submitted for any such degree, diploma or other qualification at the University of Cambridge or any other University of similar institution.

The length of the dissertation is within the limit of 60,000 words, which does not exceed the prescribed word limit for the relevant Degree Committee.

Salvatore Mesoraca

December 2017
Cambridge, UK

To those who inspired it

and will not read it.

Abstract

In this thesis, the potential of all-spinel oxide tunnel junctions in the field of spintronics has been investigated. In particular, the suitability of the metallic and superconducting $LiTi_2O_4$ as non-magnetic electrode in an almost defect-free $CoFe_2O_4$-based spin-filter tunnel junction has been explored. For this purpose, high quality spinel $LiTi_2O_4$ and $CoFe_2O_4$ thin films have been deposited by pulsed laser deposition on $MgAl_2O_4$ substrates. Both films were extensively characterised in terms of structural, surface, magnetic and transport properties. The $LiTi_2O_4$ showed metallic and superconducting properties, and the $CoFe_2O_4$ had insulating and ferromagnetic properties. A careful tuning of the different growth conditions of these oxides followed in order to grow $CoFe_2O_4/LiTi_2O_4$ bilayers in which $LiTi_2O_4$ maintains its metallic and superconducting properties and $CoFe_2O_4$ its insulating ferromagnetic characteristics.

Transport measurements at low temperature have been carried out to explore details of the tunnelling in symmetric tunnel junctions of the form $LiTi_2O_4/CoFe_2O_4/LiTi_2O_4$. The measured current–voltage characteristics of these junctions revealed clear Josephson junction behaviour due to superconductivity of the $LiTi_2O_4$ electrodes. This conclusive evidence of the tunnel nature of these junctions proves that $LiTi_2O_4$ can be used as bottom electrode in all-spinel oxide tunnel junctions.

Some of the work reported in this dissertation has been published or submitted for publication and presented as listed below.

Publications

"All-spinel oxide Josephson junctions for high efficiency spin-filtering",

S. Mesoraca, S. Knudde, D.C. Leitao, S. Cardoso and M.G. Blamire,

J. Phys. Condens. Matter, 30 015804, 2018

"Lithium out-diffusion in $LiTi_2O_4$ thin films grown by pulsed laser deposition",

S. Mesoraca, J.E. Kleibeuker, B. Prasad, J.L. MacManus-Driscoll, M.G. Blamire

J. of Crystal Growth, Vol. 454, 134-138, 2016

Presentations

"*Growth of spinel bilayers for a high efficiency room temperature spin-filter device*"

*Contributed Talk***,** S. Mesoraca and M.G. Blamire, 2016 MRS Fall Meeting, Boston, USA - November 2016

"*AR-XPS study of $LiTi_2O_4$ thin films grown by pulsed laser deposition*"

Contributed Talk**,** S. Mesoraca and M.G. Blamire, 2016 MRS Fall Meeting, Boston, USA - November 2016

"*Growth of spinel bilayers for a high efficiency room temperature spin-filter device*",

Poster Presentation, S. Mesoraca and M.G. Blamire, 23rd International Workshop on Oxide Electronics, Nanjing, China - October 2016

"*Lithium out-diffusion in $LiTi_2O_4$ thin films grown by pulsed laser deposition*"

Poster Presentation**,** S. Mesoraca and M.G. Blamire, 23rd International Workshop on Oxide Electronics, Nanjing, China - October 2016

"*Growth of spinel bilayers for a high efficiency room temperature spin-filter device*"

Contributed Talk**,** S. Mesoraca, B. Prasad, M. G. Blamire, E-MRS 2016 Fall Meeting, Warsaw University of Technology, Poland - September 2016

"*Lithium out-diffusion in $LiTi_2O_4$ thin films grown by pulsed laser deposition*"

Poster presentation**,** S. Mesoraca, J. E. Kleibeuker, B. Prasad, J. L. MacManus-Driscoll, M.G. Blamire, E-MRS 2016 Fall Meeting, Warsaw University of Technology, Poland - September 2016

"*Growth of spinel bilayers for a high efficiency room temperature spin-filter device*",

Contributed Talk**,** S. Mesoraca and M. G. Blamire, Joint European Magnetic Symposia Conference, Glasgow, UK - August 2016

"*Growth of spinel bilayers for a high efficiency room temperature spin-filter device*",

Poster Presentation**,** S. Mesoraca, B. Prasad, M. G. Blamire, SpinIcur Summer School, International Iberian Nanotechnology Laboratory, Braga, Portugal - September 2015

Acknowledgments

"Experience does not ever err, it is only your judgement that errs
in promising itself results which are not caused by your experiments."
Leonardo Da Vinci (c. 1510)

During the last four years there have been many people who have walked alongside me, I would like to thank each and every one of them. Firstly, I'd like to thank my supervisor Prof. Mark Blamire for having offered me the opportunity to work on this project. His stimulating questions and constructive criticism have guided me in the moment of need.

I would like to thank the entire Device Material Group (Ravi, Thomas, Mario, Stefania, Josée, Nadia, Abhijeet, Bhagwati, Dave, Angelo, David, Dòvid, Claire, Olly) because our lunch breaks, coffee breaks, pub trips and social activities made life in the lab much more enjoyable. Among them, a few people deserve to be thanked individually. Thank you to Dr. Bhagwati Prasad, for all the knowledge he shared with me and the immense help he gave during my first months at Cambridge. Thank you to Dr. Josée Kleibeuker for her help in the PLD/XPS experiments and for having been there at every early morning coffee break. Thank you to Dr. Nadia Stelmashenko, for every day great technical support. Last but not least, I warm thank you goes to Dr. Mario Amado Montero. The number of things we shared together in the lab and outside the lab is countless. As are countless the reasons I'd like to thank him for. In particular, I would like to express to him my sincere gratitude for having showed me that after all you can find friends, true friends, in this tough environment.

Thank you to all those who helped to proofread this thesis: Nadia, Mario and Elisa.

Thank you to Prof. Susana Cardoso for giving me the chance to carry out device fabrication at INESC-MN and sincere gratitude to Ana and Diana: without your expert advices during my breakdowns in the cleanroom, the microfabrication would have not succeeded. Thanks also to Simon and Anastasiia for keeping me company during my stays in Lisbon.

Thank you to all the SpinIcur people, for insightful comments and inputs during our meetings across Europe. In particular I would like to thank my Marie Curie fellows (Thomas, Simon, Benedikt, George, Andre, Anastasiia) for all we shared during the related social activities.

I am lucky enough to have been given the supportive gift of amazing people in my life outside the work environment and without all of them, this work would have not been completed. In particular, I would have not survived without my Cambridge friends: Niccolò, Lorena, Alain, Eloise, Stef, Kim, Eoin, a warm thank you goes to you all and to all the fun we had together in Cambridge. It will always be remembered. A special thank you goes also to my Italian friends for the great moments we had throughout these four years in Bologna, in Milan and in Rome. Thank you also to all my Hughes Hall fellows for all the enjoyable time we shared in college, especially during the first two years. In particular, I'd like to thank my Hughes Hall Boat Club fellows: it has been a pleasure to row over the Cam in the early mornings with you all.

Thank you to my mother and my sisters (Rossella, Teresa and Elisa) because they don't need a reason to be thanked for.

Finally and without hesitation I would like to thank from the bottom of my heart Guenda, without our weekends together, our trips around the World and without her encouragement, this long road would have seemed a very lonely place.

Contents

List of symbols

$\boldsymbol{A}$	*Magnetic vector potential*	H_a	*External applied magnetic field*
a	*Unit cell parameter*	H_C	*Superconducting critical field*
BE	*Binding Energy*	H_{C1}	*Superconducting lower critical field*
β	*Absorption*	H_{C2}	*Superconducting upper critical field*
C	*Curie constant*	H_{co}	*Magnetic coercive field*
χ	*Susceptibility*	H_m	*Weiss molecular field*
χ_P	*Paramagnetic susceptibility*	H_s	*Magnetic saturation field*
d	*XPS emission depth*	$\mathcal{H}$	*Hamiltonian*
δ	*Dispersion*	$\mathcal{H}_{int}$	*Interaction Hamiltonian energy*
ΔE_{ex}	*Exchange interaction energy*	$\mathcal{H}_T$	*Tunnelling perturbation Hamiltonian*
Δ, Δ_k	*Superconductor energy gap*	I	*Electrical current*
Δ_0	*Zero temperature energy gap*	I_c	*Josephson critical current*
$\Delta\phi$	*Barrier height asymmetry*	$\mathbb{I}$	*Intensity*
e	*Electron charge*	J	*Electrical current density*
E	*Kinetic Energy*	J_{ex}	*Exchange energy integral*
E_a	*Activation Energy*	J_c	*Josephson critical density of current*
E_{BCS}	*BCS total energy*	J_n	*Normal density of current*
E_g	*Band gap*	$\mathcal{J}_s$	*Coulomb exchange interaction*
E_F	*Fermi energy*	$\mathcal{K}$	*XPS transmission factor*
E_{vac}	*Vacuum energy level*	k_B	*Boltzmann constant*
$\boldsymbol{\mathcal{E}}$	*Electric field*	$\mathcal{K}_{EH}$	*Polaron-hopping constant*
ε_k	*BCS free parameter*	l	*Integer number*
F	*XPS sensitivity factor*	L	*Tunnel junction lateral size*
f	*Fermi-Dirac distribution*	λ	*Wavelength*
f_0	*Resonance frequency*	λ_{GL}	*Ginzburg-Landau penetration depth*
$\mathcal{F}_s$	*Superconductor free energy*	λ_{IMFP}	*Electron inelastic mean free path*
G	*Electrical conductance*	λ_L	*London penetration depth*
G_0	*Zero bias conductance*	Λ	*London parameter*
G_{0n}	*Zero bias normal conductance*	m	*Magnetic moment*
G^*	*Paramagnetic conductance*	m^*	*Effective mass*
G_{SF}	*Spin-filtering conductance*	m_e	*Electron mass*
Γ	*Dynes parameter*	M	*Magnetisation*
$\Gamma_{L\to R}$	*Tunnelling rate per unit of time*	M_r	*Remanent magnetisation*
h	*Planck constant*	M_s	*Saturation magnetisation*
$\hbar$	*Plank constant (reduced)*	$\mathbb{M}$	*Tunnelling matrix element*
$\boldsymbol{H}$	*Magnetic field*	μ_B	*Bohr magneton*

μ_0	*Magnetic vacuum permeability*
n	*Refractive index*
n_{air}	*Air refractive index*
n_{film}	*Film refractive index*
N	*Number of electrons*
$N_\uparrow, N_\downarrow$	*Number of up, down electrons*
N_j	*Atomic concentration of element j*
η	*Density of states*
η_n	*Normal density of states*
η_s	*Superconducting density of states*
ω_D	*Debye frequency*
ω_s	*Superconductor AC frequency*
P	*Polarisation*
P_{O2}	*Oxygen partial pressure*
P_F	*Ferromagnet polarisation*
P_{SF}	*Spin-filter polarisation*
Φ	*Magnetic flux*
Φ_0	*Magnetic flux quantum*
ϕ	*Potential energy, barrier height*
$\bar{\phi}$	*Average barrier height*
ϕ_0	*Average paramagnetic barrier height*
φ	*Superconductors phase difference*
ψ_{BCS}	*BCS wavefunction*
ψ_{GL}	*GL order parameter*
q	*Spacing between probes*
R	*Electrical resistance*
R_J	*Junction resistance*
R_n	*Normal state resistance*
R_{SF}	*Spin-filtering resistance*
RRR	*Residual resistivity ratio*
ρ	*Electrical resistivity*
ρ_0	*Residual electrical resistivity*
$\hat{s}$	*Spin operator*
σ	*Scofield photoelectron cross section*
t	*Thickness*
T	*Temperature*
t'	*Effective barrier thickness*
T_{Curie}	*Curie Temperature*
T_C	*Superconducting critical temperature*
$\mathbb{T}$	*Transmission probability*
τ_e	*Quasiparticle lifetime*
θ	*Angle*
θ_c	*Critical reflection angle*
θ_s	*Superconductor phase factor*
v	*Photon wave frequency*
v_F	*Fermi velocity*
$\boldsymbol{v}_n$	*Electron mean velocity*
V	*Bias voltage*
V_{kl}	*BCS attractive interaction potential*
w	*Weiss constant*
W_0	*Work function*
x	*Li/Ti concentration*
ξ_0	*BCS intrinsic coherence length*
ξ_s	*BCS coherence length*
ξ_{GL}	*Ginzburg-Landau coherence length*
y	*Spinel inversion parameter*
z	*XPS analysis depth*

Acronyms

AC	Alternating current
AF	Antiferromagnetic
AP	Antiparallel
APB	Antiphase boundary
AFM	Atomic force microscopy
BCS	Barden-Cooper-Schrieffer
BDR	Brinkam Dynes Rowell
CFS	Cryogenic-free system
DoS	Density of states
DC	Direct current
DWL	Direct write laser
fcc	Face-centered-cubic
FI	Ferromagnetic Insulator
F	Ferromagnetic, Ferromagnet
FET	Field-effect transistors
FIB	Focused Ion Beam
GMR	Giant magnetoresistance
GL	Ginzburg-Landau
HMDS	Hexamethyldisilazane
INESC-MN	Institute for systems and computer engineering - microsystems e nanotechnologies
I	Insulator
IBD	Ion beam deposition
IPA	Isopropyl alcohol
LED	Light emitting diode
MTJ	Magnetic tunnel junction
N	Normal metal
NIN	Normal metal/insulator/normal metal
P	Parallel
PR	Photoresist
PVD	Physical vapour deposition
PLD	Pulsed laser deposition

QMTJ	Quasi-magnetic tunnel junctions
RF	Radiofrequency
RSM	Reciprocal space map
RRR	Resistivity ratio
RMS	Root mean square
SEM	Scanning electron microscopy
SVG	Silicon Valley Group coating system
S	Superconductor, Superconducting
SF	Spin-filter
SIN	Superconductor/insulator/normal metal
SIS	Superconductor/insulator/superconductor
TM	Tedrow-Meservey
TMR	Tunnelling magnetoresistance
UHV	Ultra High Vacuum
UV	Ultra-Violet
VTI	Variable temperature insert
VSM	Vibrating sample magnetometer
WKB	Wentzel Kramers Brillouin
XRD	X-ray diffraction
XPS	X-ray photoemission spectroscopy
XRR	X-ray reflectivity
ZBC	Zero bias conductance
ZBP	Zero bias peak

List of tables

List of figures

Chapter 1. Introduction

The exponential growth in the amount of electronic devices in recent years has revolutionised modern information technology. Nowadays, conventional semiconductor devices rely on the manipulation of charge currents, ignoring the spin of the electrons. The research field aimed at developing electronic devices that exploits the additional degree of freedom provided by the electron spins is called spintronics. This spin-based electronics offers the potential for creating circuits in which more complex logic operations controlled by spin currents can be performed faster and with greater efficiency [1].

The discovery of giant magnetoresistance (GMR) in Fe/Cr multilayer structures in 1988 by A. Fert and P. Grünberg [2,3] launched the field of spintronics. These magnetic superlattices had two distinct, parallel and antiparallel, magnetic states when an external magnetic field was applied. Experimentally this resulted in two distinct resistance states with high and low values of the resistance measured by transport measurements, as shown in Figure 1. These two distinct states were then straightaway used as the (0,1) logic states in data storage and, within 10 years, IBM introduced GMR technology into the market for read heads in hard disks. Since then, GMR became so pivotal in the advancement of data storage that Fert and Grünberg were awarded the 2007 Nobel Prize in Physics.

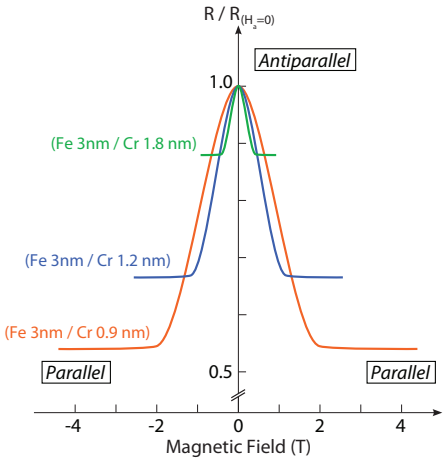

Figure 1 – GMR curves of Fe/Cr superlattices measured at 4.2 K showing two distinct resistance states for parallel and antiparallel configurations. Adapted from [2].

Even before the discovery of GMR, there had been many reports on spin-polarised electron tunnelling, another spin-dependent transport phenomena, which was demonstrated experimentally by Tedrow and Meservey [4,5] in the early 1970s. From this pioneering work, Jullière theoretically predicted a second magnetoresistive phenomenon, called tunnel magnetoresistance (TMR), which involved tunnelling between two ferromagnetic electrodes separated by a non-magnetic insulating barrier [6]. In these magnetic tunnel junctions (MTJs) the high and low resistance states are related to the relative magnetic configuration of the electrodes. According to

Jullière's analytical model, the magnitude of TMR in a MTJ is directly related to the spin-polarisation of the two ferromagnetic electrodes. The first observation of room temperature TMR was demonstrated by Moodera [7] in Al_2O_x-based MTJs with polycrystalline transition metal electrodes (NiFe, CoFe, Co). The magnetoresistance values obtained were higher with respect to GMR and evidenced the importance of TMR in spintronics. Indeed, since this discovery, there have been an enormous number of experimental and theoretical investigations in this field and nowadays reported TMR values are as high as 470% at room temperature and 800% at 5K [8]. These large TMR effects observed at room temperature enabled MTJs to be implemented in spintronics devices such as hard disk drives read-heads, non-volatile magnetic memories and magnetic field sensors. Future spintronics applications aim at integrating spins into other semiconductor technologies such as ultra sensitive spin detectors, spin field-effect transistors (spin-FET) and spin light emitting diodes (spin-LED) [1,9]. The successful implementation of these applications requires the maximization of spin-polarisation in order to obtain higher efficiency.

Recently, a new phenomenon of spin-polarised electron tunnelling based on ferromagnetic insulators (FI) has been investigated due to its capability of generating nearly 100% spin-polarised currents. This occurs due to the selective filtering of the electrons according to their spins while tunnelling across the ultrathin FI barrier [10], in contrast to the classic MTJs, in which the tunnel barrier is a non-magnetic insulator. Moreover, spin-filtering opens up to the integration of semiconductor electrodes for efficient spin injection [11] as the electrodes in such tunnel junctions are non-magnetic. The majority of FIs have Curie temperatures well below room temperature and so, although high efficiency (~100%) spin-filtering has already been reported in a wide range of materials [12], potential applications are limited by the low temperatures required. In the last few years, interest has focused on spinel ferrites FI oxides (e.g. $NiFe_2O_4$, $CoFe_2O_4$, $MnFe_2O_4$) due to their excellent magnetic properties and Curie temperatures well above room temperature [13–15]. However, the integration of these complex oxides into multilayer structures for tunnel junctions has been rather challenging. Lattice mismatch, structural differences and different optimum growth conditions between the oxide layers are known issues that hamper the epitaxial growth of heterostructures. As a consequence, spin-polarisation at room temperature has been reported in spinel ferrite $CoFe_2O_4$-based tunnel junctions [16,17] only with a very low efficiency ~4-8%. The likely reason for these low values of spin-filtering efficiency at room temperature is the formation of antiphase boundaries (APBs) in the spinel thin film barrier [18,19], which are detrimental to spin-filter efficiency as they dramatically affect the electronic and magnetic properties of the spinel ferrite [20,21]. Such defects are formed due to spinels having a lattice parameter ($a \approx 0.83$-0.85 nm) [12], almost double that of the metallic layers (Au, Pt, $LaNiO_3$, $La_{2/3}Sr_{1/3}MnO_3$) and substrates conventionally used in spin-filter devices. Achieving high spin-filter efficiencies at room temperature may therefore be dependent on overcoming structural and chemical defects in ultra-thin (<5 nm) epitaxial spinel ferrites films to be used in complex oxide heterostructures.

The objective of this thesis is to explore the use of a spinel substrate ($MgAl_2O_4$) and a spinel electrode ($LiTi_2O_4$) in fully isostructural all-spinel spin-filter tunnel junctions as a way to reduce APBs.

$LiTi_2O_4$ is one of the few conducting spinels that also has superconducting properties (critical temperature T_C ~ 13 K) and, more importantly, its lattice parameter is closely-lattice matched to those of the spinel ferrites.

The study of $LiTi_2O_4$ as potential non-magnetic electrode in all-spinel oxide tunnel junctions will be presented in this thesis as follows:

1. An introduction to spintronics and the important role it plays in modern information technology.
2. A second chapter reviewing the fundamentals of ferromagnetism, superconductivity, electron tunnelling process both in normal and superconducting tunnel junctions and spin-polarised tunnelling.
3. A third chapter describing the background of spin-filter effect, the related wide range of materials and the issues hampering high efficiency spin-filtering at room temperature. $LiTi_2O_4$ will be introduced as potential candidate for high efficiency room temperature spin-filtering in $CoFe_2O_4$-based tunnel junctions.
4. A fourth chapter briefly describing the complex spinel crystal structure and the physical properties of $LiTi_2O_4$ and $CoFe_2O_4$.
5. A fifth chapter describing the wide range of experimental techniques used throughout the research carried out for this thesis. Oxide thin films growth, structural analysis, surface chemical composition, magnetic measurements and transport measurements are among the techniques described.
6. A sixth chapter describing the two methods adapted to microfabricate tunnel junctions and the related experimental techniques.
7. A seventh chapter reporting an extensive study of the properties of the as-deposited high quality metallic-superconducting $LiTi_2O_4$ and ferromagnetic insulator $CoFe_2O_4$ thin films grown on $MgAl_2O_4$ substrates. Moreover, the crucially important optimisation growth of these two spinel oxides in the form of $CoFe_2O_4/LiTi_2O_4$ bilayers is described in this chapter.
8. An eighth chapter presenting the results for $LaNiO_3/CoFe_2O_4/LiTi_2O_4$ tunnel junctions. More importantly, transport measurements of the fully isostructural all-spinel oxides $LiTi_2O_4/CoFe_2O_4/LiTi_2O_4$ Josephson junction are discussed in detail.
9. A ninth chapter that includes the conclusions of the thesis and suggestions for future research.

Chapter 2. Theory and Fundamentals

The following chapter reviews the phenomenological and microscopic theories of ferromagnetism and outlines the fundamental theory of superconductivity. Furthermore, the theoretical basics of spin-polarised electron tunnelling are presented by initially introducing the tunnelling models for a metal/insulator/metal hetero-structure and for a superconducting tunnel junction. Next, the phenomena of spin-polarisation and the Jullière's model for magnetic tunnel junctions are presented.

2.1 Ferromagnetism

A ferromagnet (F) has a spontaneous magnetisation arising from the alignment in some favourable direction of the magnetic moments located on the lattice. This ferromagnetic order appears only at temperatures below a critical temperature, called Curie temperature T_{Curie}, and is due to the spin of the electrons aligning together and becoming correlated over a macroscopically large area: the size of a magnetic domain. Above T_{Curie}, the moments are randomly oriented (paramagnet), resulting in a zero net magnetisation M. The regions separating magnetic domains are called domain walls, where the magnetisation rotates coherently from the direction in one domain to that in the next domain. The magnetisation of a ferromagnetic sample tends to lie along certain easy directions, or easy axes, determined by crystal structure, atomic-scale texture or sample shape. Transition metals like Fe, Co and Ni are well-known examples of ferromagnets.

2.1.1 Curie-Weiss Law

The susceptibility of a material χ is a dimensionless proportionality constant that indicates the degree of magnetisation of a material in response to an externally applied magnetic field H_a:

$$M = \chi H_a \,. \tag{1}$$

Therefore, there should be a change in the ferromagnetic susceptibility at temperatures above T_{Curie}, as the material becomes paramagnetic. This behaviour of the susceptibility in the paramagnetic region is given by the Curie-Weiss Law [22]:

$$\chi = \frac{C}{T - T_{\text{Curie}}}, \tag{2}$$

where C is a material-specific Curie constant. This law, which predicts a singularity in the susceptibility at T_{Curie}, is derived from the assumption that in addition to any H_a, there is an internal

molecular field H_m responsible for the spontaneous alignment of the electron spins. In a ferromagnet such a field is proportional to its magnetisation M:

$$H_m = wM \,, \tag{3}$$

with w being the Weiss constant.

By defining χ_P as the paramagnetic susceptibility and by considering that H_m is in addition to the externally magnetic field H_a, the induced magnetisation is given by:

$$M = \chi_P(H_m + H_a) = \chi_P(wM + H_a)\,. \tag{4}$$

The magnitude of the magnetisation can be obtained from the previous self-consistent equation, resulting in:

$$M = \frac{\chi_P H_a}{1 - \chi_P w}. \tag{5}$$

Recalling the Curie law $\chi_P = C/T$, the susceptibility of the ferromagnetic material reads:

$$\chi = \frac{M}{H_a} = \frac{C}{T - Cw} = \frac{C}{T - T_{\text{Curie}}}\,, \tag{6}$$

which is the Curie-Weiss law. The singularity at T_{Curie} appears because, below this temperature, there can exist a finite M for zero applied field. The Curie-Weiss law describes fairly well the observed susceptibility variation in the paramagnetic region above the Curie point. Only in the vicinity of T_{Curie} notable deviations are observed. This due to the fact that strong fluctuations of the magnetic moments close to the phase transition temperature cannot be described by the Weiss mean field theory.

2.1.2 Microscopic description of ferromagnetism

The molecular field that Weiss used in his calculation does not really exist, but it is a useful way of approximating the effect of the quantum mechanical interatomic Coulomb interaction and the Pauli exclusion principle. In other words, if one considers two electrons, there are two possible arrangements for the spins of the electrons: either parallel or antiparallel. If they are parallel, the exclusion principle requires the electrons to remain far apart. If they are antiparallel, the electrons may come closer together and their wave functions overlap considerably. The exchange interaction is short range and therefore, only nearest neighbour atoms are responsible for producing the molecular field. Moreover, according to the Weiss-Curie model the magnitude of the molecular

(exchange) field must be enormously large (~10^3 T) to induce a significant spontaneous magnetisation at room temperature. The origin of these huge fields has been unravelled in 1928 when Heisenberg [23] postulated the quantum relation between the molecular field and the exchange interaction. The Hamiltonian describing the exchange interaction for two localized spins $\boldsymbol{s_i}$ and $\boldsymbol{s_j}$ on adjacent atoms is

$$\mathcal{H}_{ex} = -2J_{ex}\hat{\boldsymbol{s}}_{\boldsymbol{i}} \cdot \hat{\boldsymbol{s}}_{\boldsymbol{j}} \,, \tag{7}$$

where J_{ex} is the exchange integral and $\hat{\boldsymbol{s}}_{\boldsymbol{i}}$ and $\hat{\boldsymbol{s}}_{\boldsymbol{j}}$ are the two spin operators.

For positive values of J_{ex}, the exchange energy is minimal when there is a parallel alignment between the two spins, i.e. ferromagnetic alignment. For negative values of J_{ex}, instead, the most energetic-favourable orientation is for antiparallel spins, i.e. antiferromagnetic (AF) alignment [24]. Also, at temperatures approaching T_{Curie} the thermal energy k_BT (k_B is the Boltzmann constant) overcomes the exchange energy, eventually destroying the magnetic order for higher temperatures ($T > T_{\text{Curie}}$) [25].

2.1.3 Stoner model

First principles calculation using Equation (7) is not possible for more complex materials. Ferromagnetism can only be explained by a complex balance of energies, which are strongly dependent on the band-structure of a given material. Stoner applied Weiss's molecular field idea to the free-electron gas to give a phenomenological justification for the appearance of ferromagnetism. In the three-dimensional free-electron model, the density of states (DoS) $\eta(E)$ is

$$\eta(E) = \frac{1}{4\pi^2}\left(\frac{2m_e}{\hbar^2}\right)^{\frac{3}{2}}\sqrt{E} \,, \tag{8}$$

where m_e is the free electron mass, E the kinetic energy, $\hbar$ is the reduced Planck constant.

In an unpolarised electron gas with N electrons, the number of up (↑) and down (↓) spins are equal: $2N_\uparrow = 2N_\downarrow = N$. Thus, the polarisation

$$P = \frac{N_\uparrow - N_\downarrow}{N} \tag{9}$$

is null. Instead, in a polarised electron gas, $N_\uparrow$ and $N_\downarrow$ are not the same and $P \neq 0$.

A spontaneous magnetisation necessarily generates a difference between the total kinetic energy of the up spins and down spins [26], which is:

$$\Delta E = \frac{(N_\uparrow - N_\downarrow)^2}{2\eta(E_F)} = \frac{N^2P^2}{2\eta(E_F)}, \tag{10}$$

where E_F is the Fermi energy level.

This is balanced by a gain in potential energy $\Delta\phi$ when a spin is flipped due to the exchange interaction [26]:

$$\Delta\phi = -\frac{\mathcal{J}_s}{2}(N_\uparrow - N_\downarrow)^2 = -\frac{N^2\mathcal{J}_s}{2}P^2\,, \tag{11}$$

where $\mathcal{J}_s$ is the potential energy gain caused by reversing a spin, which is the phenomenological equivalent of the exchange integral J_{ex} in Equation (7). Finally, spontaneous ferromagnetism is only possible when the sum $\Delta E + \Delta\phi$ is negative (i.e. negative total change in energy), which gives a criterion for spontaneous ferromagnetism linking the Coulomb exchange interaction ($\mathcal{J}_s$) and the DoS at the Fermi level $\eta(E_F)$:

$$\mathcal{J}_s\,\eta(E_F) > 1\,. \tag{12}$$

This criterion, called Stoner's criterion [24,27,28], involving microscopic aspects of exchange, through the term $\mathcal{J}_s$, and the number of participating electrons, through the term $\eta(E_F)$, is fairly universal and its dependence on the model under consideration is little. In a ferromagnet the exchange parameter has to be comparable to the width of the band to observe spontaneous band splitting. This is why transition metal ferromagnets like Fe, Co and Ni have narrow bands and a peak in η near E_F (Figure 2). Lastly, it can be shown [29] that exchange energy ΔE_{ex} is related to the exchange field H_{ex} and the bulk saturation magnetisation M_s by the relation:

$$\Delta E_{ex} = \mathrm{M}_s H_{ex}\,. \tag{13}$$

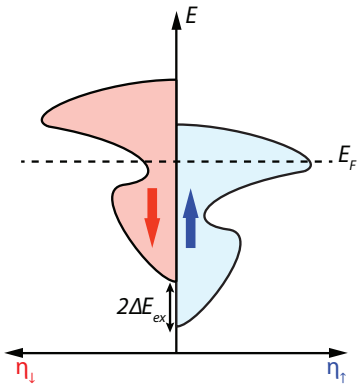

Figure 2 - Illustration of the energy splitting of the electron spin bands in a ferromagnet due to a Weiss molecular field.

2.1.4 Ferromagnetic hysteresis loop

The response of the magnetisation to an external applied magnetic field gives the characteristic of any ferromagnetic material and has the shape of a hysteresis loop, shown in Figure 3. The applied field must be comparable in magnitude to the magnetisation in order to trace a hysteresis loop.

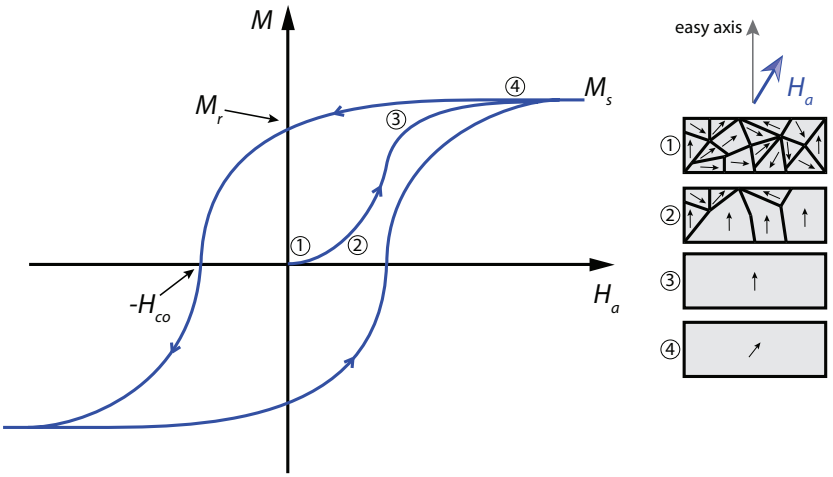

Figure 3 – The $M(H)$ hysteresis loop and the schematic illustration of the evolution of the domain structures of a ferromagnet. The saturation moment M_S, the remanent moment M_r and the coercive field H_{co} are marked on the loop.

When magnetised from a zero field value, a ferromagnetic material follows a non-linear magnetisation curve. In an unmagnetised sample, the orientation of the domains cancels out and there is zero net magnetisation. Conversely, in the presence of an applied field, domains with magnetisation antiparallel to the applied field tend to switch orientation by moving domains walls, instead of flipping spontaneously in the direction of the field, as this process is energetically cheaper. The result is a sharp increase in M until the whole sample is aligned along an easy axis as a single magnetic domain. For higher applied fields, the moment is pulled away from the easy axis and aligned with the external field and the magnetisation reaches saturation (M_S). The evolution of the domain structures is illustrated schematically in Figure 3.

If the applied field to a saturated ferromagnet is reduced, the moment relaxes back to the easy crystallographic axis and the domain remains stable as the field is reduced further, resulting in a residual magnetisation, or remanent magnetisation M_r, at zero applied field. To drive the magnetisation to zero again, the magnetic field needs to be reversed and increased to a value known as the coercive field H_{co}.

2.2 Superconductivity

The superconductivity phenomenon was discovered by Onnes [30] in 1911 by measuring a drop in electrical resistance of mercury when cooled down below 4.1 K. Later on, this superconductivity

property of showing zero resistivity below a certain critical temperature T_C, as shown in Figure 4, was observed in other materials.

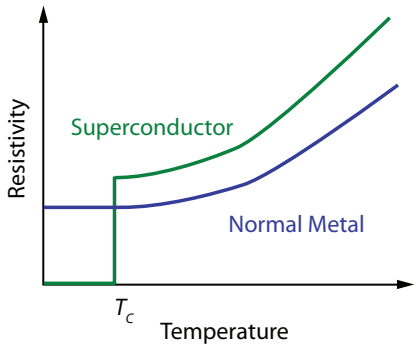

Figure 4 - Temperature dependence of a superconductor compared to a normal metal.

Later on, Meissner [31] found also that superconductors exhibit perfect diamagnetism, ejecting magnetic field lines from the interior as they approach the superconducting state. In such regard, two types of superconductors exist. In type I superconductors, the superconducting state and the Meissner screening only occur at magnetic fields below a critical field H_C (Figure 5a). Type II superconductors, instead, show perfect diamagnetism only for applied fields lower than a critical field H_{C1}. For higher fields, vortices arise when the magnetic field starts to penetrate the materials in the form of quantized flux. This mixed state, along with the superconductivity state, is eventually suppressed until another higher critical field H_{C2} is reached (Figure 5b).

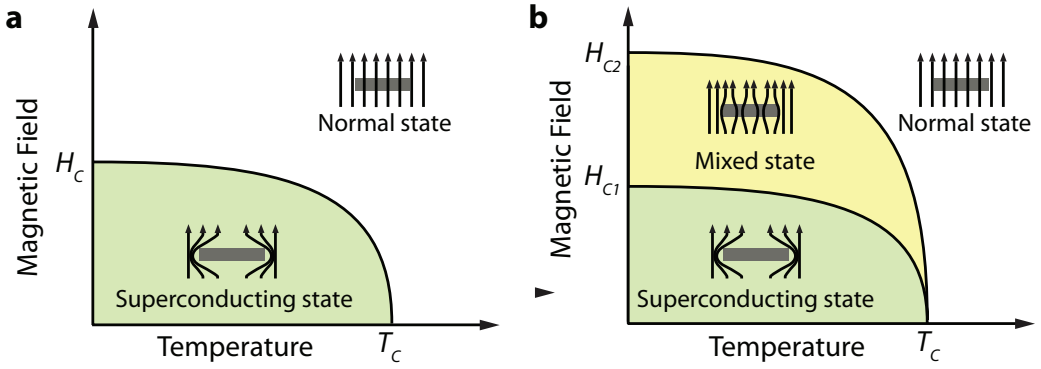

Figure 5 - Phase diagrams for type I and type II superconductors. (a) Below its T_C and for fields lower than the critcal field H_C, a type I superconductor completely expels magnetic lines of force from its interior. (b) Type II superconductors show two critical magnetic field values, one at the onset of a mixed superconducting and normal state (H_{C1}), and one where superconductivity ceases (H_{C2}).

2.2.1 Two-fluid model and London theory

The two-fluid theory [32,33] considers the free electrons in a superconductor as two separate fluids. In this phenomenological model, one fluid is formed by normal electrons, with a DoS η_n, and behave exactly as the electrons in a normal metal: they are affected by impurities and defects scattering leading to a constant normal density of current $\boldsymbol{J}_n$ in a constant electric field $\boldsymbol{\mathcal{E}}$:

$$\boldsymbol{J}_n = -\eta_n e \boldsymbol{v}_n = \frac{e^2 \eta_n \tau_e}{m_e} \boldsymbol{\mathcal{E}} \,, \tag{14}$$

where

$\boldsymbol{v}_n$ is the electron mean velocity, i.e. $\boldsymbol{v}_n = \frac{-e\tau_e}{m_e}\boldsymbol{\mathcal{E}}$,

τ_e is the mean time between scattering events,

e is the electron charge.

The other fluid of the two-fluid model consists of superconducting electrons with a DoS η_s, which is non-zero only below T_c. These electrons are not scattered while travelling through the ion lattice and their current density is $\boldsymbol{J}_s$=-$\eta_s e \boldsymbol{v}_s$. Recalling that $\partial \boldsymbol{v}/\partial t = -e\boldsymbol{\mathcal{E}}/m$ and defining m^* as the electron effective mass, then one obtains the following equation for the superconducting current density:

$$\frac{\partial \boldsymbol{J}_s}{\partial t} = \frac{\eta_s e^2}{m^*} \boldsymbol{\mathcal{E}} \,. \tag{15}$$

At temperatures below T_c, a superconductor has zero resistivity ρ thus the electric field must be zero, according to Ohm's Law, $\boldsymbol{\mathcal{E}} = \rho \boldsymbol{J}$. Hence, the normal current density must be zero and the superconducting electrons with constant current density $\boldsymbol{J}_s$ carry the dissipation-less current.

In order to also describe phenomenogically the Meissner effect in a superconductor, Fritz and Heinz London, attempted to describe the electrodynamics of a superconductor by adding restrictions on Maxwell's equations, obtaining the so called London equations [34]

$$\nabla \times \boldsymbol{\mathcal{E}} = -\frac{\partial \boldsymbol{H}}{\partial t} \,, \tag{16}$$

$$\frac{\partial \boldsymbol{J}_s}{\partial t} = \frac{1}{\Lambda} \boldsymbol{\mathcal{E}} \,, \tag{17}$$

$$\nabla \times \boldsymbol{J}_s = -\frac{1}{\Lambda} \boldsymbol{H} \,, \tag{18}$$

and by introducing $\Lambda = \frac{m^*}{\eta_s e^2}$, the London phenomenological parameter. Recalling the simplified Maxwell-Ampere's Law

$$\nabla \times \boldsymbol{H} = \mu_0 \boldsymbol{J} \,, \tag{19}$$

where μ_0 is the vacuum magnetic permeability, Equation (18) can be rewritten as

$$\nabla \times (\nabla \times \boldsymbol{H}) = -\frac{\mu_0}{\Lambda} \boldsymbol{H} \,, \tag{20}$$

which simplifies to:

$$\nabla^2 \boldsymbol{H} = \frac{\boldsymbol{H}}{{\lambda_L}^2}. \tag{21}$$

The previous differential equation introduces the London penetration depth λ_L and states that the only uniform magnetic field ($\nabla^2 \boldsymbol{H} = 0$) in a superconductor is the field identically zero ($\boldsymbol{H} = 0$ everywhere) otherwise $\boldsymbol{H}$ would depend on position. In other words, the Meissner effect is due to the suppression of the applied external field by an equal but opposite magnetic field generated by the supercurrent density at the superconductor surface. Moreover, the solution of Equation (21), for a simple one-dimensional case, is

$$H(x) = H_{ext} e^{-x/\lambda_L}, \tag{22}$$

therefore the London equations imply that an applied magnetic field H_{ext} decays exponentially within the superconductor, as shown in Figure 6, over a length scale given by λ_L.

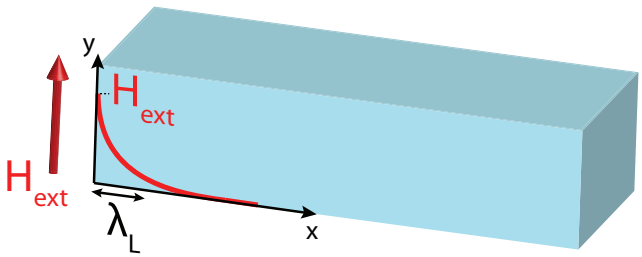

Figure 6 – The penetration of a magnetic field into a superconducting material.

In a similar manner, London equations lead to a solution for the supercurrent density that has the same solution as the field, see Equation (21). Thus the supercurrent, which screens the interior of the superconductor from an external field, runs within a thin layer in a direction perpendicular to the magnetic field.

2.2.2 Ginzburg-Landau theory

While the London phenomenological theory explains rather well a few aspects of the physics of a superconductor, it does not provide an explanation for the superconductivity phenomenon or an explanation for the conduction process at the microscopic level. In 1950 Ginzburg and Landau [35] considered superconductivity as a phase transition and introduced an order parameter ψ_{GL} to describe the phenomenon. Such a parameter was set to be zero for temperatures above the critical temperature and non-null in the superconducting state:

$$\psi_{GL} = \begin{cases} 0 & T > T_c \\ \psi_{GL}(r,T) & T < T_c \end{cases}. \tag{23}$$

Moreover, according to this theory, ψ_{GL} should also be related to the density of superconducting electrons in the London equations:

$$\eta_s = |\psi_{GL}|^2 . \tag{24}$$

Next, building on the general theory of second order transitions introduced by Landau [36], GL assumed the free energy density of the superconductor $\mathcal{F}_s$ to be an expansion in powers of ψ_{GL}:

$$\mathcal{F}_s = \mathcal{F}_n + \alpha|\psi_{GL}|^2 + \frac{\beta}{2}|\psi_{GL}|^4 , \tag{25}$$

where $\mathcal{F}_n$ is the free energy density of the normal state. By adding a few constraints such as a slowly varying $|\psi_{GL}|$ near T_c, i.e. not taking into account any not-physically possible rapid changes of the order parameter, and adding also a magnetic vector potential $\boldsymbol{A}$ (such that $\boldsymbol{B} = \nabla\times\boldsymbol{A}$) with a proper gauge, the free energy reads:

$$\mathcal{F}_s = \mathcal{F}_n + \alpha|\psi_{GL}|^2 + \frac{\beta}{2}|\psi_{GL}|^4 + \frac{1}{2m^*}|(-i\hbar\nabla - 2eA)\psi_{GL}|^2 + \cdots , \tag{26}$$

where α is proportional to $(T - T_c)$ and β a finite and positive constant.
Minimising the free energy, Equation (26), with respect to ψ_{GL}, the GL equation is obtained:

$$\alpha\psi_{GL} + \beta|\psi_{GL}|^2\psi_{GL} + \frac{1}{2m^*}(-i\hbar\nabla - 2eA)^2\psi_{GL} = 0 . \tag{27}$$

The previous equation resembles a Schrödinger-like equation, with ψ_{GL} as quantum wavefunction, from which the GL penetration depth λ_{GL} and coherence length ξ_{GL} can be estimated:

$$\lambda_{GL} = \sqrt{\frac{m^*\beta}{4\mu_0 e^2|\alpha|}} , \tag{28}$$

$$\xi_{GL} = \sqrt{\frac{\hbar^2}{2m^*|\alpha|}} . \tag{29}$$

The first parameter sets the exponential law to which an external magnetic field decays inside the superconductor and resembles the penetration depth previously introduced by the London

brothers; the latter sets the exponential law according to which small perturbations of superconducting electrons recover their equilibrium value ψ_{GL_0}.

2.2.3 Bardeen Cooper Schrieffer theory of superconductivity

The first microscopic theory of superconductivity originated from the discovery of the change of the critical temperature with isotope [37,38], pointing to the fact that there should be an interaction between the electrons and the lattice of the superconducting materials. Later on, in 1956, Cooper showed that, in the presence of an attractive interaction, the Fermi sea becomes unstable and that two electrons of opposite momentum near the Fermi surface tend to pair in a bound state of lower energy [32,41]. These so-called Cooper pairs act like bosons, which can condense into the same energy level.

Building on these findings, Bardeen Cooper Schrieffer (BCS) [39,40] postulated, in 1957, that the basic interaction responsible for superconductivity is an attractive interaction between electrons generated by an exchange of virtual phonons that can overcome the Coulomb repulsion. While moving in a superconductor, an electron with, for example, momentum and spin $(k, \uparrow)$ generates a deformation of the nearby positive charges in the lattice. For weak interactions, the lattice relaxes in a time much slower than the electron moves away, allowing another electron, with momentum l and opposite spin $\downarrow$, to be attracted by the potential well, which effectively creates a coupling between the electrons, as shown in Figure 7a. In the normal state of a metal, electrons move independently, whereas in the condensed state they are bound into Cooper pairs by the attractive interaction. In this BCS state, the breaking of one pair changes the energy of the whole condensate. Thus, the energy needed to break any single pair is related to the energy to break all of the pairs of the collective state, meaning that there should be an energy gap for single-particle excitation.

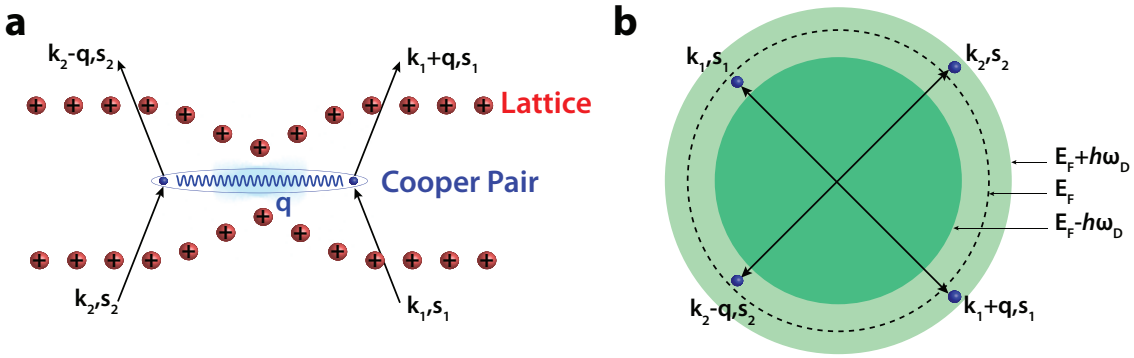

Figure 7 –(a) Electron-electron interaction mediated by a phonon q which scatters two electrons with (k_1, s_1) and (k_2, s_2) into $(k_1 + q, s_1)$ and $(k_2 - q, s_2)$ in the momentum-spin space. (b) As the receiving states must be free (due to the Pauli exclusion principle) and as the electron energies must differ by no more than the phonon energy (due to the BCS assumption), the electron-electron interaction is only possible in a vicinity of $\hbar\omega_D$ of the Fermi surface.

The formalism of BCS theory is based on the reduced potential for the attractive interaction of the electrons. The related interaction Hamiltonian

$$\langle l_\uparrow, -l_\downarrow | \mathcal{H}_{int} | k_\uparrow, -k_\downarrow \rangle = V_{kl} \,, \tag{30}$$

describes a transition of a Cooper pair with momentum $k_\uparrow, -k_\downarrow$ to a state $l_\uparrow, -l_\downarrow$, and is considered isotropic and constant for energies of the electrons that differ from the Fermi surface by no more than the highest-energy phonon $(\hbar\omega_D)$ [42] (Figure 7b), while it vanishes elsewhere:

$$V_{kl} = \begin{cases} -V & |E_k - E_F| \leq \hbar\omega_D \\ 0 & otherwise \end{cases} \,, \tag{31}$$

here ω_D is the Debye frequency of the superconducting material and V is positive in order to have an attractive potential. Applying a variational ansatz for the wavefunction, BCS theory is able to provide an approximation for the quantum-mechanical many-body state for such a system of attractively interacting electrons. Further details about the BCS formalism can be found elsewhere [42].

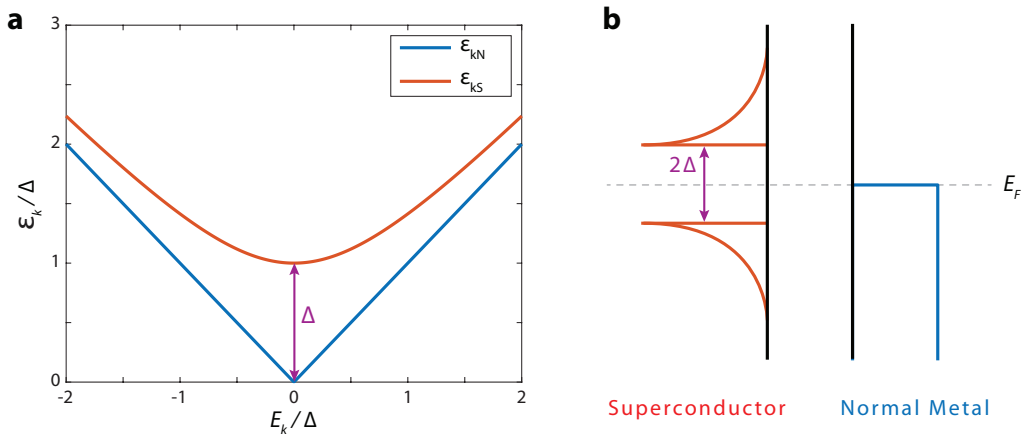

Figure 8 – (a) Normalised energy eigenvalues ε_k in the normal and superconducting states as function of E_k. (b) The density of states near the E_F in a superconductor, showing the energy gap 2Δ, and in a normal metal at $T = 0$.

The first major result of BCS theory is that it derived the important theoretical prediction of the existence of an energy gap and described how the DoS changes on entering the superconducting state. In particular, it linked the energy E_k of an electron in a state k, measured from E_F, to the superconducting excitation energy ε_k according to the following relation:

$$\varepsilon_k = \sqrt{\left(E_k{}^2 + \Delta_k{}^2\right)} \,. \tag{32}$$

From this it can be observed that the gap energy Δ_k is the order parameter of the superconducting phase: the energy is still greater than zero with no kinetic energy, unlike in the normal state (Figure 8a). At $T = 0$ all electrons occupy states below the energy gap and a minimum energy of 2Δ has to be supplied to produce an excitation across the gap, as shown in Figure 8b.

Using the BCS formalism, the gap Δ_k can be determined by self-consistently solving the following equation [42,44]:

$$\Delta_k = -\sum_l \frac{\Delta_l V_{kl}}{\sqrt{\left({E_k}^2 + {\Delta_l}^2\right)}}. \tag{33}$$

In the weak-coupling limit of BCS theory, Δ_k is momentum independent (s-wave symmetry) meaning that $\Delta_k = \Delta$. Moreover, from statistical averaging [44] of the BCS equations, it can also be shown that the temperature dependence of $\Delta(T)$ near T_c for a weakly coupled superconductor is given by:

$$\frac{\Delta(T)}{\Delta(0)} \approx 1.74\sqrt{1 - \frac{T}{T_c}}. \tag{34}$$

Many experiments have been designed to test this temperature dependence of the energy gap (Figure 8) and it has been found that the so-called universal BCS relation $\Delta_0/k_B T_c \approx 1.764$ is valid for most superconducting materials [45]. Other materials, such as Al, deviate from the predictions of BCS, and therefore may not be considered conventional superconductors.

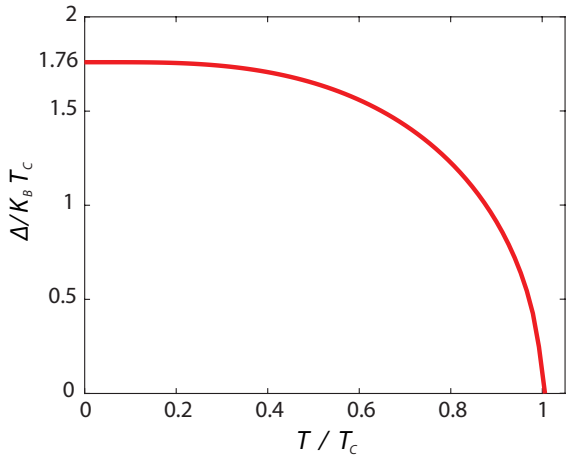

Figure 9 - Temperature dependence of the energy gap $\Delta(T)$ according to the BCS theory.

The coherence length, first introduced in the GL theory, can now be understood in BCS theory as the distance between the two electrons of a Cooper pair [43] and, at $T = 0$, is related to the energy gap according to:

$$\xi_0 = \frac{\hbar v_F}{\pi \Delta_0}, \tag{35}$$

where v_F is the Fermi velocity and ξ_0 is the intrinsic coherence length, which is temperature-independent and valid in the clean limit only, i.e. when the electron mean free path λ_{IMFP} is larger than ξ_0. Conversely, Gor'kov showed that in the dirty limit ($\lambda_{IMFP} < \xi_0$), the superconductor coherence length becomes [46]:

$$\xi_s = 0.85\sqrt{\xi_0 \, \lambda_{IMFP}}\,. \tag{36}$$

In conclusion, BCS allows describing microscopically what occurs in the lattice and Fermi system and has been verified by tunnelling experiments (see section 2.4). The theory has anyhow drawbacks as it best approximates only conventional weakly coupled superconductors.

2.3 Electron tunnelling process

Electron tunnelling is a fundamental phenomenon in quantum mechanics describing an electron particle with finite kinetic energy E overcoming a potential barrier $\phi > E$. While for classic physics theory this process would not be possible, at the quantum scale the electron has a finite probability to tunnel through the potential barrier due to its wavelike nature.

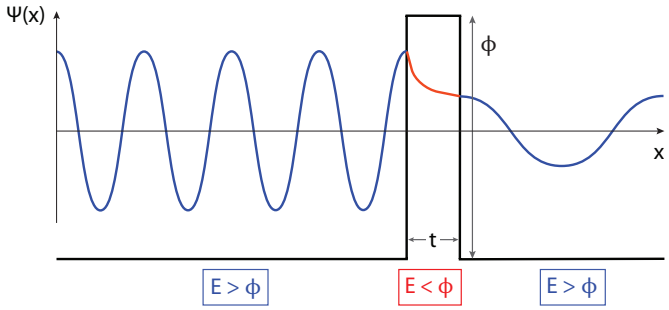

Figure 10 – Quantum tunnelling through a barrier with finite thickness t.

In detail, the evanescent states of an electron wave incident with energy E on a step potential with height ϕ have a finite probability of emerging on the other side of the barrier, as shown in Figure 10. Such transmission probability $\mathbb{T}$ is related to the barrier thickness t and to the difference between the electron's energy and that of the potential barrier as follows [47]:

$$\mathbb{T}(E) \propto exp\left[-\frac{2t}{\hbar}\sqrt{2m_e(\phi - E)}\right]. \tag{37}$$

Thus, for higher barrier thickness and barrier height, the transmission probability decreases exponentially.

Applying a bias voltage V to a normal metal/insulator/normal metal (NIN) trilayer structure, also called tunnel junction, is a representative implementation of the tunnelling process. Due to the difference in resistance between the metal electrodes and the insulating barrier, the Fermi energy E_F of one electrode is raised by eV compared to the other. Thus, electrons near E_F of the high energy-electrode tunnel elastically across the barrier into lower energy electrode, as shown in Figure 11.

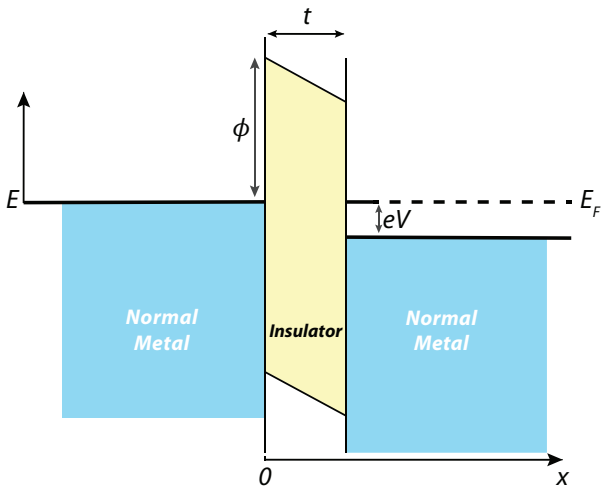

Figure 11 - Band diagram for a normal metal-insulator-normal metal junction with applied bias eV. Shaded blue areas represent filled states, open areas are empty states, and the yellow area represents the forbidden gap in the insulator.

The tunnelling process can be considered as a perturbation, as suggested by Bardeen [48], and thus the Hamiltonian $\mathcal{H}$ of a tunnel junction can be decomposed in three independent Hamiltonians

$$\mathcal{H} = \mathcal{H}_L + \mathcal{H}_R + \mathcal{H}_T, \tag{38}$$

being $\mathcal{H}_L$ and $\mathcal{H}_R$ the Hamiltonians of the independent left and right electrodes, and $\mathcal{H}_T$ being the tunnelling perturbation. Second quantization of the tunnelling Hamiltonian provides the probability for an electron particle to transfer from a state to the left $|L\rangle$ electrode to a state to the right $|R\rangle$ electrode by a tunnel process and corresponds to the matrix element $\mathbb{M} = \langle R|\mathcal{H}_T|L\rangle$ [49,50]. According to Fermi's Golden Rule [51], the tunnelling rate per unit of time of electrons $\Gamma_{L\to R}$ with a certain energy E transmitted from the right to left electrode is:

$$\Gamma_{L\to R} = \eta_L(E_L)\eta_R(E_R)|\mathbb{M}|^2 f(E_L)[1 - f(E_R)]\,, \tag{39}$$

where

$\eta_L(E_L)$ is the DoS at a certain energy E_L of the right electrode,

$\eta_R(E_R)$ is the DoS at a certain energy E_R of the right electrode,

$f(E)$ is the Fermi–Dirac function $f(E) = \left[1 + \exp\left({E - E_F}/{k_B T}\right)\right]^{-1}$.

Equation (39) includes the probability that the states in the left electrode are occupied, $f(E)$, and that the states in the right electrode are empty, $1 - f(E)$, in order to impose that electrons on one side of the barrier must have empty states to tunnel into on the other side of the barrier.

Under the application of a voltage V between the two electrodes, the tunnelling current flowing across a tunnel junction from left to right $I_{L\to R}$, according to the energy reference shown in Figure 11, is:

$$I_{L\to R} = \int \eta_L(E)\eta_R(E - eV)|\mathbb{M}|^2 f(E)[1 - f(E - eV)]\,dE\,. \tag{40}$$

Similarly, the tunnelling current from the right electrode to the left electrode $I_{R\to L}$ can be written as:

$$I_{R\to L} = \int \eta_R(E - eV)\eta_L(E)|\mathbb{M}|^2 f(E - eV)[1 - f(E)]\,dE\,. \tag{41}$$

The net tunnelling current I between the electrodes is the difference between left- and right-going currents is:

$$I = I_{L\to R} - I_{R\to L} = \int \eta_L(E)\eta_R(E - eV)|\mathbb{M}|^2[f(E) - f(E - eV)]\,dE\,. \tag{42}$$

Equation (42) can be simplified by employing several more or less sophisticated models. In particular, for low bias voltages ($eV \ll E_F$) the transmission matrix and the densities of states can be considered to be constants along the range of energy in the integration [48]. In addition, in the limit of zero temperature, the factor $[f(E) - f(E + eV)]$ can be replaced by a Dirac delta function

$$[f(E) - f(E + eV)] \approx -eV\frac{\partial f(E)}{\partial E} = -eV\delta(E_F)\,, \tag{43}$$

thus, Equation (42) for the net current reduces to:

$$I(V) \propto |M|^2 \eta_L(E_F)\eta_R(E_F)V\,. \tag{44}$$

This relation implies that the tunnelling current is dominated only by electrons near E_F and that, in the limit of low bias voltage [47], the conductance dI/dV is proportional to the product of the densities of states at E_F in two metal electrodes:

$$\frac{dI}{dV} \propto |M|^2 \eta_L(E_F)\eta_R(E_F)\,. \tag{45}$$

A bias-dependent tunnel current density $J(V)$ analytical solution for a NIN tunnel junction can be obtained using the Wentzel-Kramers-Brillouin (WKB) approximation [52]. An average barrier height $\bar{\phi}$ approximates the rectangular barrier making the calculation of the transmission probability easier. The solution reads:

$$J(\mathrm{V}) = \frac{J_o}{t^2}\left[\left(\bar{\phi} - \frac{eV}{2}\right) exp\left(-At\sqrt{\bar{\phi} - \frac{eV}{2}}\right) - \left(\bar{\phi} + \frac{eV}{2}\right) exp\left(-At\sqrt{\bar{\phi} + \frac{eV}{2}}\right)\right], \tag{46}$$

where the two constants J_o and A are, respectively, $\frac{e}{4\pi^2\hbar}$ and $\sqrt{\frac{8m_e}{\hbar^2}}$.

For $eV < \bar{\phi}$, i.e. in the tunnelling regime, the tunnelling current density can be expanded in a power series as [47]:

$$J(V) \approx \alpha V + \beta V^3 + \cdots, \tag{47}$$

and hence, the shape of a conductance curve $G(V) = dI/dV$ for NIN tunnel junction in low bias voltage regime is parabolic. This model, proposed by Simmons [53], is generally applicable to symmetric junctions where the conductance curve is symmetric around $V = 0$, whereas usually the barrier are mostly asymmetric due to the different growth conditions at the metal/insulator and insulator/metal interfaces. Brinkman, Dynes and Rowell (BDR) [54] modified the previous model by introducing an additional parameter, the barrier asymmetry $\Delta\phi = \phi_R - \phi_L$, accounting for the asymmetry in the barrier, and thus modifying the tunnel current density as follows:

$$J(\mathrm{V}) = \mathrm{G}_0\left[V - \left(\frac{A_0\Delta\phi}{16\bar{\phi}}\right)(eV)^2 + \left(\frac{9A_0^2}{128\bar{\phi}}\right)(eV)^3\right], \tag{48}$$

where $\mathrm{G}_0 = 3.16\times10^{10}\sqrt{\bar{\phi}}exp\left(-1.025\sqrt{\bar{\phi}}\right)/t$ and $A_0 = 4\sqrt{2m}t/3\hbar$.

Though these two models ignore important effects on the tunnelling current of pinholes and defects in the barrier, which are often present in tunnel junctions, effective barrier height and thickness can be estimated with reasonable accuracy by a fitting of the experimental data.

2.4 Superconducting tunnel junctions

The first experimental observations of electron tunnelling in junctions were carried between two semiconductors by Esaki in 1957 [55] and between two metals by Giaever in 1960 [56]. Later on, tunnelling measurements were carried out between a normal metal and a superconductor. The current-voltage $I(V)$ characteristics of Al_2O_3-based tunnel junction with Al and Pb electrodes showed a change from a linear to a non-linear behaviour when the Pb layer was brought into its superconducting state [56,57]. The tunnelling current was remarkably reduced at low voltage bias. Moreover, the conductance curves displayed a clear resemblance with the BCS theory for the quasiparticle DoS in a superconductor (Figure 12).

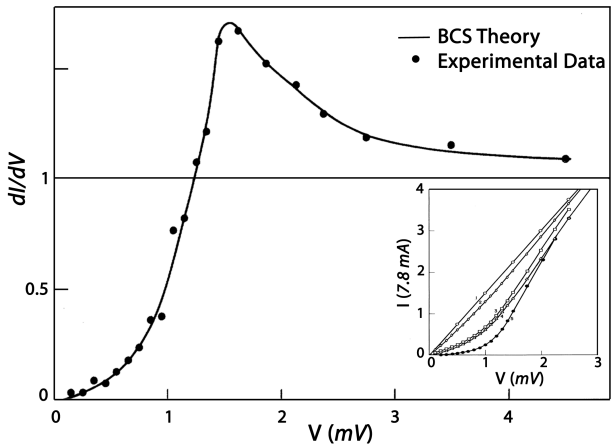

Figure 12 – First tunnelling experiment in a Al/Al_2O_3/Pb tunnel junction measured by Giaever [57]. Zero applied field (H_a=0) dI/dV curve at 1.6 K clearly shows the presence of the BCS energy gap at low voltage bias. Inset, I(V) curves for H_a=0 to 0.27 T, showing the SC transition in the Pb layer.

This experiment was the first direct observation of the energy gap in the superconductor and provided strong confirmation of the BCS theory. This pioneering work also confirmed the importance of the electrode/barrier couple, i.e. not to the individual bulk properties, and that the tunnelling properties of any tunnel junction are dominated by the local DOS at the electrode/barrier interface [58], where the electrode may be a normal metal or a superconductor, as anticipated in the previous section of this chapter.

2.4.1 Superconductor-insulator-normal metal junctions

According to the BCS theory, see section 2.2.3, the DoS of quasiparticles in the superconducting state η_s at $T = 0$ is

$$\frac{\eta_s}{\eta_n} = \begin{cases} \dfrac{E}{\sqrt{E^2 - \Delta^2}} & for\ |E| \geq \Delta \\ 0 & for\ |E| < \Delta \end{cases}, \tag{49}$$

therefore, no tunnelling current can occur across a thin insulating barrier from a normal metal electrode to a superconductor electrode if the applied bias voltage is less than the energy gap. This is because there are no available states in the superconductor, as shown in Figure 13a, for the electrons to tunnel into and therefore the tunnelling probability is zero. In this superconductor/insulator/normal metal SIN junction, a current can only tunnel across the barrier when the applied bias reaches the value of ±Δ. Thus, the absence of current at small values of applied bias is an experimental proof of the existence of a gap in the DoS of a superconductor (Figure 13b). At higher temperatures, but still lower than T_c, a tunnelling current can be measured at small voltages due to electrons thermal excitations. The gap completely vanishes at temperature above T_c and the $I - V$ curve resembles the one of a NIN junction.

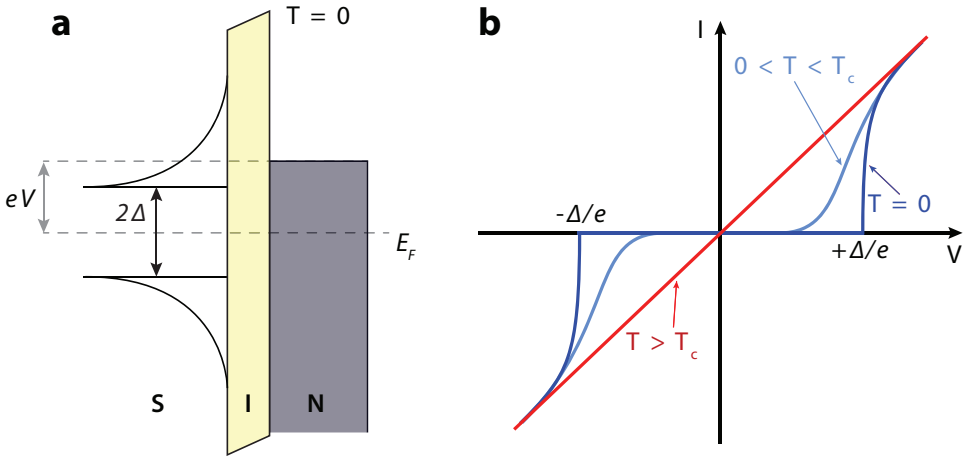

Figure 13 – (a) Energy band diagram at $T = 0$ of a superconductor/insulator/normal metal tunnel junction with applied voltage V. (b) Tunnelling I(V) characteristics in a superconductor/insulator/normal metal tunnel junction at different temperatures.

The tunnelling rate in such a junction will be, as shown in Equation (39) for a NIN junction, the convolution of the DoSs of the normal metal and of the superconductor. In good approximation, η_n is constant around E_F on an interval relevant for superconductivity, thus the experimental dI/dV behaviour, shown in Figure 14, will resemble the DoS of the superconductor according to:

$$\frac{dI}{dV} \propto \int \eta_s(E) \left[-\frac{\partial f(E + eV)}{\partial E} \right] dE \cong \eta_s(E_F)\,. \tag{50}$$

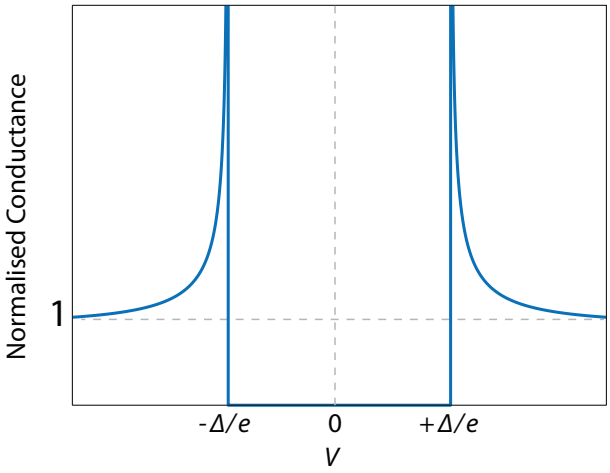

Figure 14 – Normalised differential tunnelling conductance dI/dV curve for a generic superconductor/insulator/normal metal tunnel junction resembling the DoS of the superconductor with an energy gap Δ.

In Giaever first SIN measurement and in many other experiments, the coherence peaks at $\pm\Delta/e$ do not appear perfectly sharp as shown in Figure 14 but instead are broadened and are of finite width. The origin of this deviation from the perfect case can be manifold, such as a finite lifetime of the Cooper pairs due to scattering at surfaces or spin-orbit effects in heavy superconductors. Often, a phenomenological smearing parameter Γ can be used to smooth the gap-related structures in the η_s. This parameter accounts for the lifetime broadening of the quasiparticles [59] and modifies η_s as follows:

$$\eta_s(E,\Gamma) = \mathbb{R}e\left[\int \frac{E - i\Gamma}{\sqrt{(E - i\Gamma)^2 - {\Delta_k}^2}} dk\right], \tag{51}$$

here the Dynes parameter Γ is defined as $\Gamma = {\hbar}/{\tau_e}$, where where τ_e is the lifetime of the quasiparticle. Figure 15 displays the modified differential tunnelling conductance dI/dV for different values of Γ. It can be clearly seen that Γ not only broadens the quasiparticle excitation peaks but also reduces their amplitude.

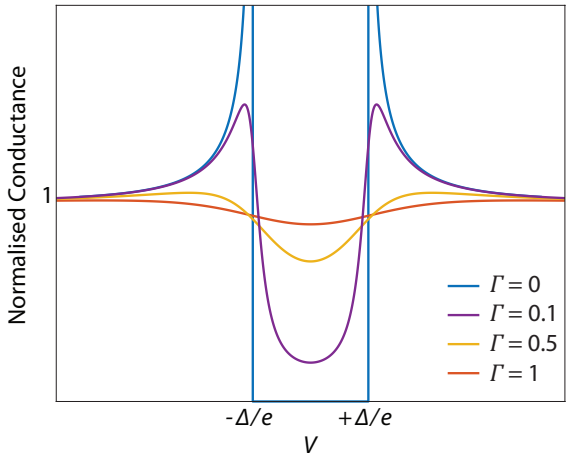

Figure 15 - Calculated differential tunnelling conductance dI/dV normalised to the superconducting gap as a function of the lifetime parameter Γ using Equation (51) for a superconductor/insulator/normal metal junction. For Γ=0 the ideal sharp BCS DOS without any states in the superconducting gap is obtained. Non-zero Γ values smear the DOS around the gap edges and produces finite amount of states in the superconducting gap.

2.4.2 Superconductor-insulator-superconductor metal junctions

In the previous section, the current-voltage characteristic of a tunnel junction with a superconducting electrode was investigated in terms of the band model for the quasi-particles in the two electrodes. In the following, the same approach is applied to tunnel junctions with two superconducting electrodes (SIS) junction.

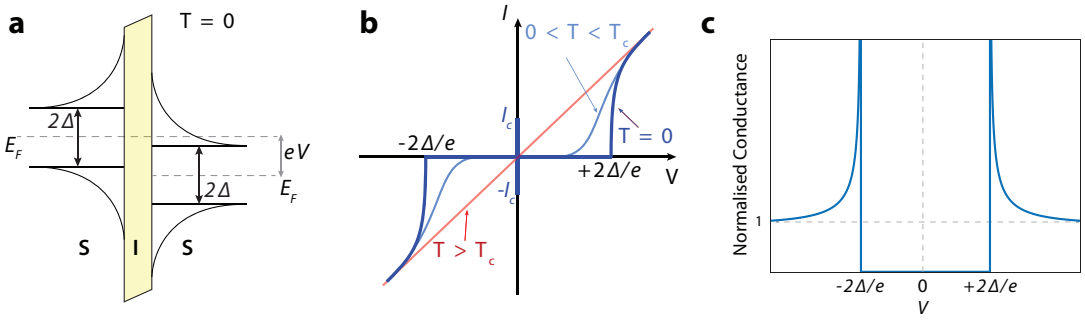

Figure 16 - (a) Energy band diagram at $T = 0$ of a SIS tunnel junction with applied voltage V. (b) Tunnelling I(V) characteristics in a SIS junction at different temperatures. (c) Calculated differential tunnelling conductance dI/dV normalised to the superconducting gap for a superconductor/insulator/superconductor metal junction (with no Cooper pair tunnelling).

Figure 16a shows the corresponding band model at $T = 0$ when a positive voltage is applied. Also in this case, tunnelling can take place at any energy, but only if the electrons in one electrode have allowed and free states at their energy to tunnel to in the other electrode. Therefore, in a SIS junction electrons can tunnel from one side to the other only for applied voltages higher than $V > 2\Delta/e$ and, due to the high density of states at the band edge, the current starts suddenly, as shown in the $I - V$ depicted in Figure 16b, with the abrupt increase in current at energy gap voltage $2\Delta/e$. For voltages applied below this threshold, the current is strictly zero. At finite

temperatures, there is some current that flows in this subgap region due to the thermal quasiparticles.

The current flowing in a SIS junction may be calculated using yet again Equation (42) and by integrating the DoS in the two electrodes and by taking into account the occupied and unoccupied states in each electrodes according to the Fermi distribution:

$$I \propto \int \eta_{s1}(E-eV)\eta_{s1}(E)[f_1(E-eV)-f_2(E)]dE \\ = \int \frac{|E-eV|}{\sqrt{(E-eV)^2-\Delta_1^2}}\frac{|E|}{\sqrt{E^2-\Delta_2^2}}[f_1(E-eV)-f_2(E)]dE \ . \tag{52}$$

In the case of two different superconducting electrodes (SIS'), there exist two distinct features in the $I-V$ curve when the bias voltage is equal to the sum and difference of the two gaps. For an applied voltage $eV=\Delta_1-\Delta_2$, as the singularities in DoS in the two superconductors align, there is a peak in the subgap, and for $eV=\Delta_1+\Delta_2$ the tunnel current increases sharply. When the bias voltage is much greater than the sum of the two gaps ($eV \gg \Delta_1+\Delta_2$) the superconducting DoS approaches its value in the normal state, and the differential resistance becomes ohmic.

The $I-V$ characteristic described thus far in a SIS junction is related to the quasiparticles tunnelling across the junction. In 1962, Josephson theoretically predicted that in a superconducting junction with a thin enough insulating barrier, a dissipationless tunnel current can flow across the device. The current is entirely carried by Cooper pairs and is described by the Josephson [60] equations:

$$I = I_c sin(\varphi) \tag{53}$$

$$\frac{\partial \varphi}{\partial t} = \frac{2eV}{\hbar} \ , \tag{54}$$

where I_c is the critical current and φ the phase difference $\varphi=\theta_{s1}-\theta_{s2}$ between the macroscopic BCS wave functions describing the superconducting electrodes, as introduced in section 2.2.3. Equation (54) suggests that if a finite direct current (DC) voltage V were applied, the phase difference would not remain constant and, as a consequence, an alternating current (AC) with frequency $\omega_s=2eV/\hbar$ would flow. The appearance of the Josephson critical current is not only restricted to superconducting tunnel junction, but it occurs in a variety of cases whenever two superconductors are separated by a weak-link, which can be an insulating region, a normal metal or a short, narrow constriction. I_c is therefore an important phenomenological parameter of the device and can be affected by temperature as well as by an applied magnetic field. Its maximum value is related to $\Delta(T)$ and to R_n, the normal state resistance of the tunnel junction [61], by:

$$I_c(T) = \frac{\pi}{2}\frac{2\Delta(T)}{eR_n} tanh\left(\frac{\Delta(T)}{2k_BT}\right), \tag{55}$$

which for low temperatures ($T \ll T_c$), as the gap becomes independent on temperature, reduces to:

$$I_c = \frac{\pi\Delta}{2eR_n}. \tag{56}$$

An external magnetic field H_a, penetrating the tunnel junction parallel to the barrier plane and perpendicular to the direction of I_c, generates a spatial modulation of the phase difference and consequently influences the maximum I_c. The phase difference along the tunnel junction axis (x-axis) as a function of the magnetic field is found to be:

$$\varphi' = \frac{2et'}{\hbar} H_a x + \varphi\,, \tag{57}$$

where $t' = t + 2\lambda_L$, t the thickness of the barrier plus the London penetration depth on both sides of the barrier. Thus, the current density reads:

$$J = J_c sin\left(\frac{2et'}{\hbar} H_a x + \varphi\right). \tag{58}$$

The magnetic field dependence of the total maximum critical current flowing across the tunnel junction is obtained by an integration with respect to x:

$$I_c(\phi) = I_c(0)\left|\frac{sin\left(\pi\frac{\Phi}{\Phi_0}\right)}{\left(\pi\frac{\Phi}{\Phi_0}\right)}\right|, \tag{59}$$

where $\Phi = t'LH_a$ the magnetic flux in the tunnel junction of lateral size L , and $\Phi_0 = h/2e \approx$ 2.07x10^{-15} Wb the elementary quantum of magnetic flux. In Figure 17, the critical current $I_c(\phi)$ is represented as a function of the magnetic flux and shows close resemblance to the Fraunhofer pattern for a single-slit diffraction of waves. The roots of $I_c(\phi)$ are located at each integral multiple of ϕ_0. With a sufficiently strong magnetic field the Josephson current and hence the Josephson effect as a whole can be suppressed.

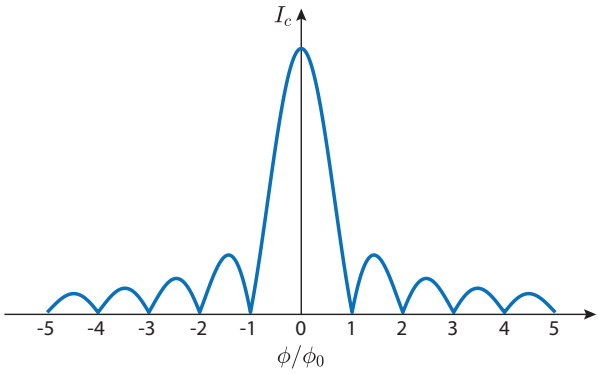

Figure 17 – Fraunhofer pattern for the critical current dependence on the magnetic flux.

2.5 Spin-polarisation

Derived by Paul Dirac in 1928 [62], the intrinsic angular momentum, spin, carried by elementary particles is another essential aspect arising from the relativistic quantum mechanics.

As anticipated in section 1 of this chapter, in normal metals (paramagnetic materials) the DoS of spin-up and spin-down are equal because of Pauli's exclusion principle (Figure 18a). Instead, in a ferromagnetic material the DoS at the Fermi level is different for the up-spin and down-spin sub-bands, $\eta_{\downarrow}(E_F) \neq \eta_{\uparrow}(E_F)$, due to the intrinsic exchange splitting $2\Delta_{ex}$ (Figure 18b) generated by the spontaneous magnetisation of the magnetic material.

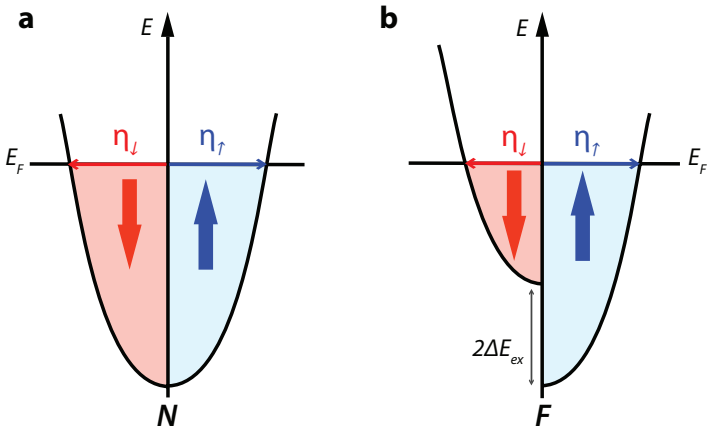

Figure 18 - A free electron density of states diagram characteristic of a nonmagnetic metal N and of a ferromagnet F.

The electrical current J in a ferromagnet, according to the "two current model" deduced by Mott in 1936 [63], is the sum of spin-up and spin-down partial currents, $J_{\uparrow}$ and $J_{\downarrow}$. Therefore, an electrical current flowing in a ferromagnetic material has a net spin-polarisation

$$P = \frac{J_{\uparrow} - J_{\downarrow}}{J_{\uparrow} + J_{\downarrow}} \neq 0 \,. \tag{60}$$

Generally, the degree of spin-polarisation is limited to about 50% in conventional ferromagnetic elements and alloy materials. It can reach higher values in a special set of materials called half-metallic ferromagnets, which by definition have only one spin sub-band that crosses the Fermi level. These materials can thus lead to nearly 100% spin-polarisation [64].

As it will be discussed later on, Tedrow and Meservey [65] defined P also as the degree of DoS asymmetry between the two spins subbands:

$$P = \frac{\eta_{\uparrow}(E_F) - \eta_{\downarrow}(E_F)}{\eta_{\uparrow}(E_F) + \eta_{\downarrow}(E_F)} \ . \tag{61}$$

It can be easily understood from Figure 18a that $P = 0$ for a normal metal, essentially due to the equal occupancy of its spin-up and spin-down states, while the net magnetisation in a ferromagnet ensures that $0 < P < 1$ as depicted in Figure 18b. This had a profound implication in the integration of ferromagnetic materials in tunnel junctions and has lead to a new research field of spin-polarised tunnelling.

2.6 Magnetic tunnel junctions

The integration of ferromagnetic materials, whether as magnetic conducting electrodes or as magnetic insulating barrier in tunnel junctions, opens up an entire new way of seeing the tunnelling process. The conduction of the electrons will now be dependent on the magnetic configuration of the magnetic layers and thus the current may be polarised. For example, the tunnelling current in MTJs is dependent on the relative orientation of the magnetisations of the F layers and gives rise to the TMR phenomenon.

In 1975 Jullière first proposed a simple analytical model for tunnelling between ferromagnets [6] and defined TMR as the difference in conductance (resistance) between parallel G_P (R_P) and antiparallel G_{AP} (R_{AP}) magnetisation states of the electrode, normalised by the antiparallel conductance:

$$\text{TMR} = \frac{G_P - G_{AP}}{G_{AP}} = \frac{R_{AP} - R_P}{R_P} \ . \tag{62}$$

In this model, Jullière assumed spin conservation during the tunnelling process and tunnelling only occurring between bands of the same spin orientation. In other words, tunnelling happens to an empty up (down) spin band in one electrode from a filled-up (down) spin in the other. A schematic representation is shown in Figure 19 for both parallel and antiparallel configurations.

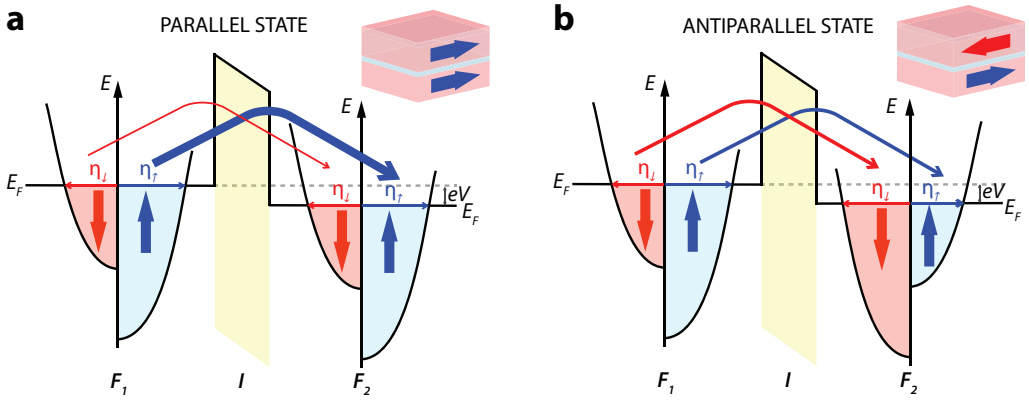

Figure 19 – Schematic representation of the Jullière's model for spin-polarised tunnelling in the (a) parallel and (b) antiparallel state.

With these assumptions, the total current flowing across the junction for parallel and antiparallel configurations can be assumed to be the sum of two spin channels currents:

$$I_P = I_P^{\downarrow} + I_P^{\uparrow} \tag{63}$$

$$I_{AP} = I_{AP}^{\downarrow} + I_{AP}^{\uparrow} \ . \tag{64}$$

Recalling Equation (45), which links the tunnel conductivity to the product of the DoS, the conductivity of the parallel state G_P is:

$$\left(\frac{dI}{dV}\right)_P = G_P \propto \eta_L^{\uparrow}(E_F)\eta_R^{\uparrow}(E_F) + \eta_L^{\downarrow}(E_F)\eta_R^{\downarrow}(E_F)\,, \tag{65}$$

while for the antiparallel state, G_{AP} is:

$$\left(\frac{dI}{dV}\right)_{AP} = G_{AP} \propto \eta_L^{\uparrow}(E_F)\eta_R^{\downarrow}(E_F) + \eta_L^{\downarrow}(E_F)\eta_R^{\uparrow}(E_F)\,. \tag{66}$$

Using Equation (66) to define the tunnelling spin-polarisation in the left P_L and right P_R ferromagnetic electrode, the conductances can be rewritten as follows:

$$G_P \propto (1+P_L)(1+P_R) + (1-P_L)(1-P_R) \propto (1+P_L P_R)\,, \tag{67}$$

$$G_{AP} \propto (1+P_L)(1-P_R) + (1-P_L)(1+P_R) \propto (1-P_L P_R)\,. \tag{68}$$

Then, according to Equation (62), the TMR ratio of a magnetic tunnel junction is

$$\mathrm{TMR} = \frac{2P_L P_R}{1 - P_L P_R}. \tag{69}$$

Jullière's model therefore implied that using F electrodes with the highest possible P at room temperature would maximise TMR. The first experimental confirmation of Jullière's model came almost 20 years later. Al_2O_x-based MTJs with two polycrystalline transition metal electrodes (Co, CoFe, NiFe) showed the first room temperature TMR (~10%) [7]. Since this discovery, there have been an enormous number of experimental and theoretical investigations on TMR, mostly to achieve defect-free interfaces between the barrier and the electrodes, to reduce pinholes in the barrier and to develop proper patterning method to reduce the junction dimensions down to the sub-micron scale. In addition, to achieve independent switching (i.e. two distinct P and AP magnetic states) the F electrodes must be carefully chosen according to their magnetic properties. Usually this is done by using two F electrodes with appropriately different coercive fields, or by pinning one of the electrodes with an AF pinning layer via exchange coupling [66]. Nowadays, thanks to the improvements in all these fields, reported TMR values are as high as 470% at room temperature and 800% at 5K [8]. These are obtained thanks to fully epitaxially MgO-based MTJs grown on CoFeB electrodes and also due to the fact that the band symmetry of Fe/MgO, theoretically predicted by Butler [67], contributes to the production of very highly spin-polarised tunnelling currents.

Chapter 3. Spin-filter effect

The next chapter provides an overview of the spin-filter effect. Firstly, the theoretical fundamentals are presented. The central part of the chapter focuses on the various methods used to demonstrate this effect and gives an overview on the wide range of FI materials used for spin-filtering, from the first experiments on Eu-chalcogenides to the latest on spinel ferrites oxide. Regarding the latter, a description of the antiphase boundaries formation during their growth and their role in limiting high efficiency at room temperature is presented. In conclusion, it is introduced the potential of $LiTi_2O_4$ as electrode in all-spinel $CoFe_2O_4$-based tunnel junction for the generation of highly spin-polarised currents at room temperature.

3.1 Spin-filter theory

Although the advancements in TMR have been outstanding and its leading role in data storage technology is more and more consolidated, it was clear since its discovery that P in MTJs would be limited by the maximum degree of spin-polarisation of 50% in conventional F transition metals and alloys. A solution is to adopt half-metallic ferromagnetic materials but they are by design quite difficult to achieve. In fact, to date high TMR ratios have been achieved in half-metallic ferromagnetic electrodes, such as CrO_2, $La_{0.7}Sr_{0.3}MnO_3$ and Fe_3O_4, but they vanish quickly with increasing temperature [68,69].

An entirely different and very promising way to polarise a charge tunnel current is to take advantage of the spin-selective tunnelling through a FI barrier. In this device the barrier is responsible for the polarisation of the charge current from the normal electrodes. On the contrary, in conventional MTJs the thin nonmagnetic insulating barrier acts only as a decoupler of the magnetic moments of the ferromagnetic electrodes and the TMR response arises from the related imbalance of the DoS for spin-up and spin-down electrons.

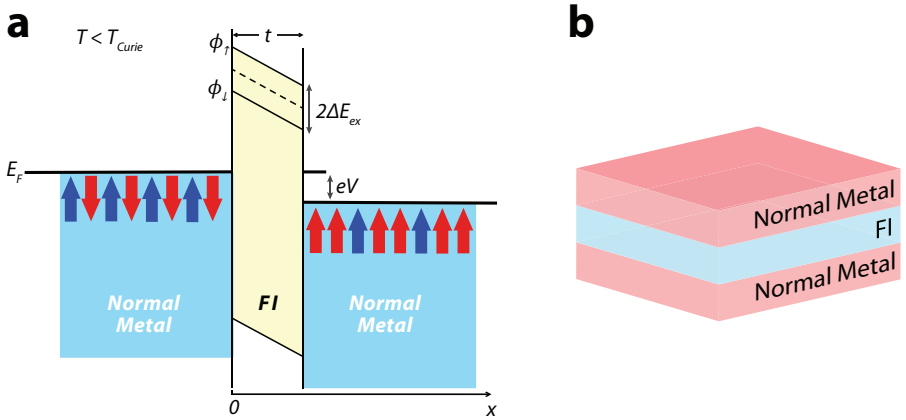

Figure 20 – (a) Schematic illustration and (b) band diagram of a spin-filter tunnel junction below T_{Curie} showing the spin splitting of the conduction band of the FI barrier.

At temperatures below the ferromagnetic transition temperature of a FI, the conduction band is spin split due to the exchange energy $2\Delta_{ex}$, as shown in Figure 20a. Thus, two different barrier heights exist for spin-down and spin-up electrons:

$$\phi_{\uparrow,\downarrow} = \phi_0 \pm 2\Delta_{\mathrm{ex}} , \tag{70}$$

where ϕ_0 is the average paramagnetic barrier height at temperature above T_{Curie}.
Recalling from chapter 2 that the tunnelling probability depends exponentially on barrier height, the two spin currents for a given barrier of thickness t are:

$$I_{\uparrow,\downarrow} \propto exp\left(-t\sqrt{\phi_{\uparrow,\downarrow}}\right) . \tag{71}$$

Due to this exponential barrier height-dependence of the tunnelling current a very high spin-polarised current can be achieved in a metal/FI/metal tunnel junction where the electrodes are nonmagnetic, shown in Figure 20b. This phenomenon of generating polarised currents is called spin-filter effect. In contrast to MTJs, the polarisation occurring in a spin-filter device is not determined by the DoSs at the Fermi energy of the ferromagnetic electrodes but only on the magnetic properties and thickness of the FI barrier. Moreover, even a modest exchange splitting of the spin-up and spin-down barrier heights can yield a high polarisation:

$$P = \frac{I_\uparrow - I_\downarrow}{I_\uparrow + I_\downarrow} \sim 100\% \ . \tag{72}$$

3.2 Spin-filter tunnel junctions

The first indirect evidence of the spin-filter effect emerged from the transport measurements on EuS and EuSe films by Esaki [70]. For direct measurements of the current polarisation resulting from the spin-filter effect, one of the non-magnetic electrodes of the junction needs to be replaced by one that provides spin analysing capabilities. The first direct measurement of the degree of spin-polarisation from spin-filtering was performed at low temperature by exploiting the pioneering spin-polarised electron tunnelling experiments of Tedrow and Meservey (TM), based on the use of superconducting Al as spin-analyser electrode [4,5], as shown in Figure 21a. In the following years, quasi-magnetic tunnel junctions were used to determine the effectiveness of a spin-filter material by measuring the TMR arising from the different magnetisation orientations between the FI barrier and a FM electrode that replaced the top non-magnetic electrode of a spin-filter device (Figure 21b). This method allowed to overcome the low temperature restriction of the TM method, and to determine whether spin-polarisation could occur at higher temperatures in a whole different range of FI materials with higher T_{Curie}.

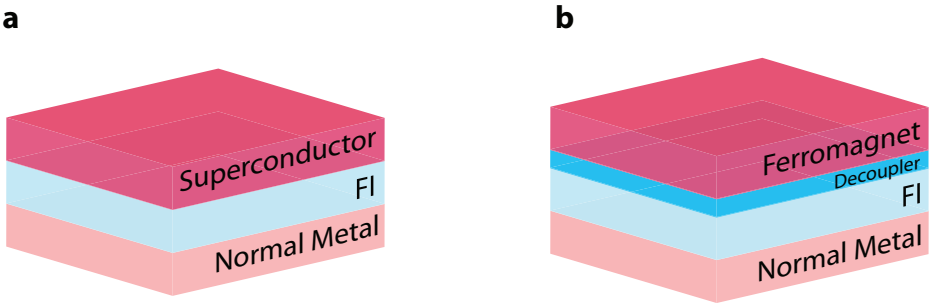

Figure 21 – To directly measure the spin-polarisation arising from the spin-filter effect the non-magnetic top electrode of a spin-filter tunnel junction is replaced (a) by a superconducting electrode or (b) by a ferromagnetic electrode magnetically decoupled from the FI barrier.

3.2.1 Tedrow-Meservey method

Following the ground breaking work of Giaever on SIN tunnel junctions, described earlier in chapter 2, TM demonstrated that the tunnelling current from a ferromagnetic metal electrode through an insulating AlO_x barrier is spin-polarised [4,5]. This was possible by exploiting the Zeeman-split DoSs of an Al superconductor, which acted as spin detector for the tunnel current from the ferromagnetic electrode.

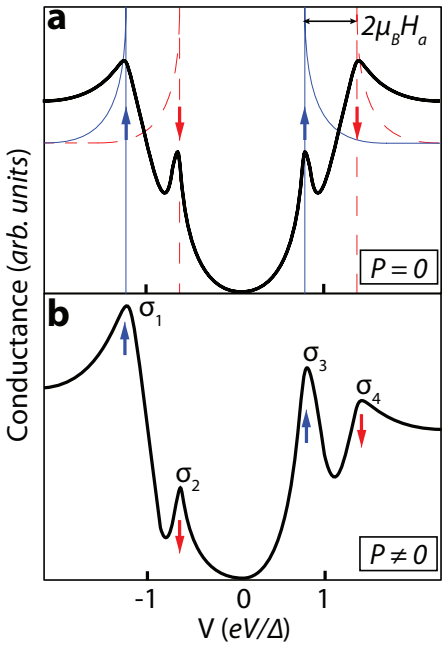

Figure 22 – Conductance dI/dV curves versus bias voltage for F/I/S tunnel junctions as measured by the TM technique. (a) The blue and red dotted lines indicate the deconvoluted spin-up and spin-down DoS respectively. The black curve corresponds to the total conductance and is symmetric, indicating that $P = 0$. (b) dI/dV in an applied field when a FM metal is used as the current source. Here, the spin-up DoS is visibly greater than the spin-down DoS resulting in an asymmetric curve and $P \neq 0$. Adapted from [5].

When a magnetic field is applied parallel to the plane of the films, the quasiparticle energies of the superconductor are shifted by $\pm 2\mu_B H_a$. The quasiparticle states with magnetic moments parallel to the magnetic field are lowered in energy by $-\mu_B H_a$, and those that are antiparallel are raised by

$+\mu_B H_a$ (Figure 22a). Thus, if this Zeeman splitting is achieved, the DoS in a superconductor is spin-dependent, allowing it to act as spin detector. The conductance of the Ni/Al_2O_3/Al tunnel junctions analysed by TM were visibly asymmetric as consequence of the different spin-up and spin-down DoSs at the Fermi surface of the Ni electrode modifying the height of the coherence peaks in the dI/dV curve (shown in Figure 22b). The value of the effective carrier P in the ferromagnet at E_F may therefore be reasonably estimated using the following relationship between the heights of the inner peaks (as shown in Figure 22b) σ_2 and σ_3 [5]:

$$P(E_F) = \frac{\eta_\uparrow(E_F) - \eta_\downarrow(E_F)}{\eta_\uparrow(E_F) + \eta_\downarrow(E_F)} \approx \frac{\sigma_2 - \sigma_3}{\sigma_2 + \sigma_3} \,. \tag{73}$$

The TM method for detecting the polarisation of the current with a superconductor has a few requirements. Firstly, the thickness of the superconducting film should be sufficiently thin to avoid any orbital screening currents suppressing the polarisation/electron spin interaction with the magnetic field, i.e. the Zeeman splitting of the quasiparticle states in the superconductor. Moreover, the H_c of the superconductor should be large enough so that the high fields needed to observe the splitting do not affect the superconducting state at temperature below T_c. Another requirement is that element with low spin-orbit scattering (i.e. low atomic number) should be used to avoid spin scattering events in the superconductor. These are the reasons why Al has been a perfect candidate for this purpose: a light element with a H_c of ~5 T for thickness of 4-5 nm.

Although Equation (73) provides only an estimation of P, as an accurate determination would require taking into account also spin-orbit scattering in the superconductor, other TM measurements with different F electrodes (Fe, Co and Gd) produced similar results, thus proving the effectiveness of the method [5].

3.2.2 Quasi-magnetic tunnel junctions

Though the TM technique described in the previous section is a useful technique for spintronics systems, it is restricted to temperatures below the T_C of the superconductor, i.e. well below room temperature. Thus, to overcome such a limitation, one could take advantage of the exchange-split DoSs of a ferromagnetic electrode, rather than the Zeeman-split DoSs in a superconductor, to perform spin analysing measurements in a spin-filter tunnel junction. The tunnelling current in this quasi-magnetic tunnel junction (QMTJ) will be dependent on the relative magnetisation of the FI insulating barrier and of the F electrode, giving rise to the TMR effect, see Figure 23. In a QMTJ the parallel state leads to a high tunnel conductance (low resistance) as the number of electrons with non-filtered spin orientation have a large number of available spin-states in the receiving F electrode. Conversely, in the antiparallel state, the tunnelling of such electrons is limited due to the lower availability of spin states in the receiving F electrode (high resistance). By recalling

Equation (69) from Jullière's model for TMR, the degree of spin-polarisation arising from a spin-filter P_{SF} can be estimated according to

$$\text{TMR} = \frac{R_{AP} - R_P}{R_P} = \frac{2P_F P_{SF}}{1 - P_F P_{SF}} \ , \tag{74}$$

where P_F is the known polarisation of the ferromagnetic electrode used in a QMTJ.

As for conventional MTJs, TMR can be observed to quantify P_{SF} only if the switching is independent and with well-separated coercivities. Indeed, adding a non-magnetic insulating layer to act as a decoupler prevents magnetic coupling between the spin-filter barrier and the F electrode. Oppositely, QMTJ has a different bias dependence than a conventional MTJ, in which the TMR increases with bias up to a certain value and then decreases for higher bias applied, due to the spin-split conduction band of the FI barrier [71].

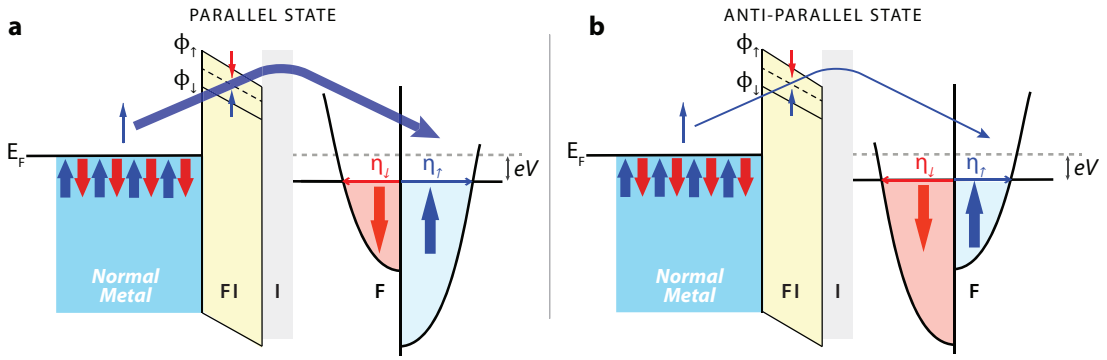

Figure 23 – Band diagram of a quasi-magnetic tunnel junction in the (a) parallel state and (b) antiparallel state.

3.2.3 Temperature dependent transport measurement

An indirect but reliable way of estimating the spin-polarisation arising from a spin-filter device is based on the clear decrease of the junction resistance R_j usually observed when cooled below T_{Curie}, due to the lowering of the barrier height. In particular, R_j of a spin-filter tunnel junction, at temperatures above the T_{Curie} of the FI, shows the typical behaviour of a semiconducting barrier, that is an exponential increase with decreasing temperature. However, when the temperatures falls below T_{Curie}, R_j decreases due to the exchange splitting of the conduction band that leads to the temperature-dependent reduction of the barrier height for one spin direction [72]. A typical R_j curve for a spin-filter tunnel junction is depicted in Figure 24.

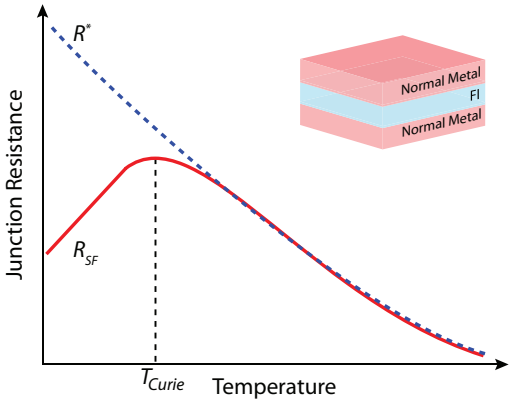

Figure 24 – The red curve show the typical behaviour of the junction resistance versus temperature for a spin-filter tunnel junction (schematically shown in the inset). The blue-dotted curve is the fitted temperature dependence in the high temperature range.

Recalling that $G \propto exp\left(\sqrt{\phi}\right)$ in the framework of the WKB approximation (see chapter 2), the spin-dependent barrier lowering leads different contributions of spin-up $G_{\uparrow}$ and spin-down $G_{\downarrow}$ to the total conductance G [65,72]. The P_{SF} of a spin-filter device can be estimated, after simplifications, by:

$$P_{SF} = \left|\frac{G_{\uparrow} - G_{\downarrow}}{G_{\uparrow} + G_{\downarrow}}\right| \approx tanh\left[cosh^{-1}\left(\frac{G_{SF}}{G^*}\right)\right], \tag{75}$$

where G_{SF} is the measured experimental value below T_{Curie}, and G^* is the conductance in the absence of exchange splitting. The latter can be extrapolated from the temperature dependence of R_j in the high temperature ($T > T_{\text{Curie}}$) regime, as shown in Figure 24.

3.3 Spin-filter materials

3.3.1 Europium chalcogenides

Following Esaki's indirect evidence of spin-filtering in transport measurements on EuS and EuSe [70], the spin-polarisation arising from spin-filtering in Eu chalcogenide tunnel barriers was directly measured via TM technique. The general structure of these junctions were Al/EuX/M, where M= Al, Au, Ag or Y, and X= Se, S or O. The barriers were usually 1-4 nm thick and the superconducting Al electrode usually 4.2 nm thick.

The first demonstration was carried in EuS-based junctions by Moodera *et al*. in 1988 [73]. The T_{Curie} of EuS is 17 K, while the band gap and the exchange splitting are 1.65 eV and 0.36 eV, respectively. The conductance curves measured at 0.4 K, below the critical temperature of the superconducting Al electrode (~2.7 K), showed a SC gap-like behaviour with the four peaks arising from the Zeeman splitting of the quasiparticle DoS (Figure 25). The effect was observed even at zero applied field and, because the electrodes are not F, and thus are not spins sources, the large measured polarisation (P=80%) is clearly arising from the spin-filtering of the FI barrier.

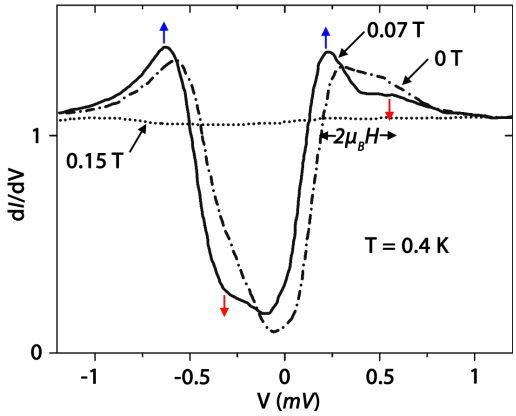

Figure 25 – Dynamic conductance of an Au/EuS/Al tunnel junction at 0.4 K measured at different applied magnetic fields. The amount of Zeeman splitting and the spin orientation of the Zeeman split DoS (coloured arrows) are indicated for the 0.07 T curve. The polarisation estimated P was 80%±5%. Adapted from [73] .

The high polarisation achieved prompted LeClair *et al*. to integrate EuS in QMTJs. The experiments demonstrated a TMR ratio of nearly ~100% at 2K [74]. The F electrode used to analyse the spin-polarisation was Gd, while the non-magnetic electrode was Al. Figure 26 shows the two distinct switching observed: the one at low fields, due to the magnetisation reversal of the EuS; and the one at higher fields, which corresponds to the change in magnetisation orientation of Gd. Note also that above the T_{Curie} of EuS (16 K), TMR was absent. The P_{SF} obtained of nearly 90% was in line with the results obtained by TM technique. Later on, Nagahama *et al*. [75] added a decoupling layer (AlO_x) between the FI and the F electrode in order to avoid any exchange coupling between the two magnetic materials. Their Al/EuS/AlO_x/Co tunnel junctions were effectively decoupled and provided more robust and reproducible TMR measurements.

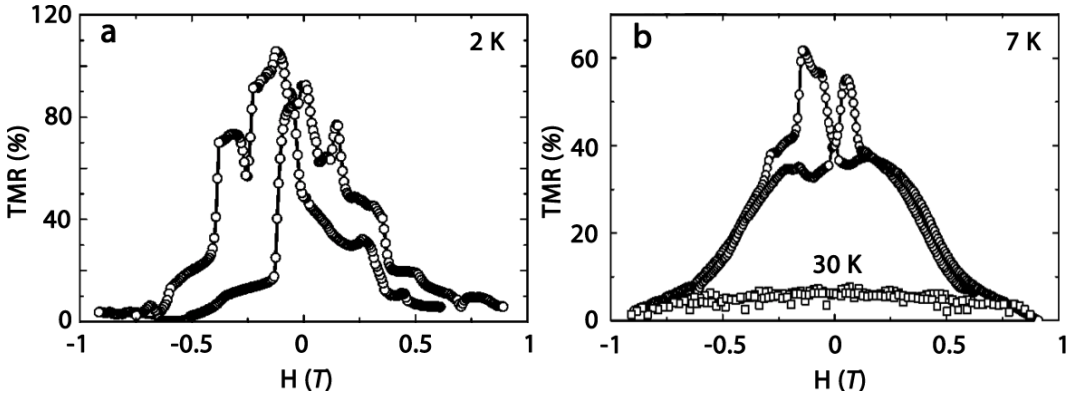

Figure 26 – (a) TMR as a function of magnetic field at 2 K and (b) at 7 K and at 30 K for an Al/EuS/Gd QMTJ. For temperatures below the T_{Curie} of the FI, two distinct switching can be seen. Adapted from [74].

Another Eu-based material used as spin-filter material is EuSe. It has the peculiar property of having a transition from an antiferromagnetic state, at zero field, into a ferromagnetic state, at

high field [76]. Thus, when integrated in a TM-like tunnel junction, at zero field no Zeeman splitting is observed and the conductance curve is symmetric about zero bias. For higher fields, the splitting is clearly visible and increasing with field due to the fact that EuSe enters in the ferromagnetic state and its exchange splitting increases. Consequently, also the polarisation increases. This behaviour was observed by Moodera *et al*. in Ag/EuSe/Al tunnel junctions [77], see Figure 27. The estimated polarisation value was as high as (97±3)%, which is in agreement with the presence of only the spin-up peaks in the dI/dV curves as there is nearly zero conductance in the spin-down DoS.

In all the Eu-chalcogenides-based spin-filter tunnel junctions described thus far, the clear decrease of the junction resistance, due to the lowering of the barrier height at temperatures below T_{Curie} of the FI, was observed (Figure 27b).

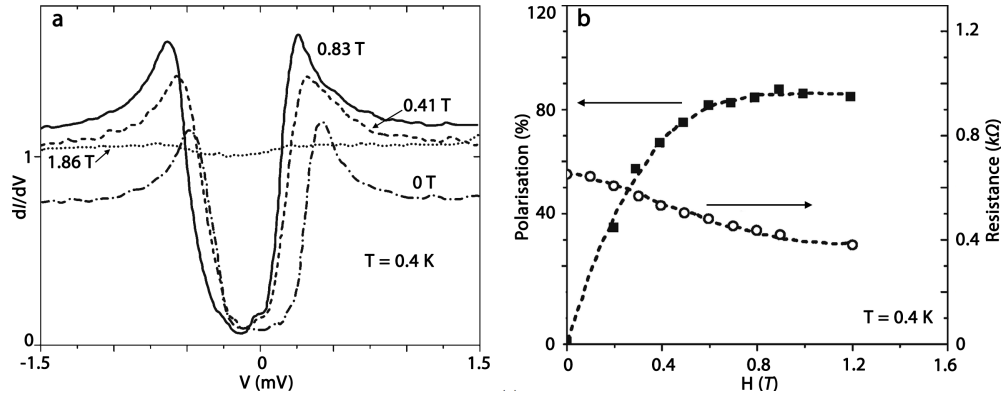

Figure 27 – (a) Dynamic conductance of a Ag/EuSe/Al tunnel junction at 0.4 K measured at different applied magnetic fields showing Zeeman splitting at fields higher than zero. (b) Polarisation and junction resistance as a function of applied field for the same junction. Adapted from [78].

Although both EuS and EuSe proved to be very efficient spin-filter materials, their magnetic ordering temperature of 16.6 K and 4.6 K, respectively, limited the filtering of the spins at temperatures in the liquid helium range. In 2004, Santos and Moodera [78] fabricated EuO-based spin-filter tunnel junction in an effort to obtain spin-filtering at higher temperatures, due to the higher magnetic ordering temperature (69 K), which can also be increased by rare earth metal doping, and greater $2\Delta E_{ex}$ (0.54eV) of this Eu-oxide. Nevertheless, their Al/EuO/Y/Al junctions showed a polarisation of only 29% at 0.45 K via TM-technique. This was due to the challenging deposition of high-quality, stoichiometric thin EuO which is affected by the more readily formation of Eu_2O_3, a more stable, non-magnetic and non-spin-filtering phase. This work pointed out for the first time at the importance of the FI/electrode interfaces in terms of quality and stoichiometry as detrimental effects on the spin-polarisation efficiency arise from low quality, non-stoichiometric interfaces.

3.3.2 Nitrides

Other materials which are potential candidates for spin-filtering due to their magnetic and semiconducting behaviour, are the rare-earth nitrides [79]. Up to date, GdN has been investigated for this purpose. It has a very large magnetic moment (7 μ_B), the highest T_{Curie}~70 K [80–82] K and very large spin-filtering efficiency (~90%) has been observed in NbN/GdN/NbN spin-filter tunnel junctions at 5 K [83] K . GdN-based devices offer the possibility of tuning the spin-polarisation of the current due do the large magnetoelectric coupling of this rare-earth nitride. The oxidation readiness with air of the earth nitrides and the consequent need to passivate these materials with capping layers [79] is currently hampering the use of these materials as FI in spin-filters.

3.3.3 Perovskite oxides

The issue that arose from the low spin-filter efficiency in EuO, due to the low quality of the film, shifted the interest towards complex oxide spin-filters (perovskites or ferrites), as they can be epitaxially grown on either elemental metals or oxide electrodes. Moreover, their T_{Curie} temperatures are higher than those of the Eu-based FIs.

Among the perovskites, $BiMnO_3$ (T_{Curie} = 105 K), and its La-doped phase, have been successfully demonstrated to produce spin-filtering in QMTJs experiments. The isostructural fully polarised half-metallic ferromagnetic $La_{2/3}Sr_{1/3}MnO_3$ [84] is used as a spin analyser to probe the filter efficiency. TMR measurements on $La_{2/3}Sr_{1/3}MnO_3/SrTiO_3/BiMnO_3/Au$ epitaxial tunnel junctions showed a TMR ratio of 50% and a P_{SF} of 22% at 3 K [85] K . Though the FI $BiMnO_3$ was grown epitaxially on $SrTiO_3$, which acted as decoupler and ferromagnetic electrode, P_{SF} decreased rapidly with increasing temperature, completely disappearing above 40 K, still below the bulk T_{Curie} of $BiMnO_3$. This was probably due to the lower T_{Curie} and lower exchange splitting than the bulk of the FI when grown as thin enough film to act as tunnel barrier. Consequently, this limited efficient spin-filtering to temperatures much less than T_{Curie} and reduced the spin-filter efficiency.

Another perovskite material used as FI in spin-filters has been $Pr_{4/5}Ca_{1/5}Mn_{1-y}Co_yO_3$, due its T_{Curie} of 75 K, by Harada *et al.* [86]. Epitaxial tunnel junction of the form $LaNiO_3/Pr_{4/5}Ca_{1/5}Mn_{1-y}Co_yO_3/SrTiO_3/La_{2/3}Sr_{1/3}MnO_3$ showed a TMR response as high as 120% at 4 K. Using the extended Jullière's model and assuming a P_F for the $La_{2/3}Sr_{1/3}MnO_3$, decoupled with $SrTiO_3$, of 90%, the estimated P_{SF} was 42%. Also in this case, the drop in junction resistance below the ferromagnetic transition temperature of $Pr_{4/5}Ca_{1/5}Mn_{1-y}Co_yO_3$ was observed.

Recently, spin-filtering has been observed also in $Sm_{3/4}Sr_{1/4}MnO_3$-based tunnel junctions. This perovskite FI oxide has a T_{Curie} of ~100 K and showed spin-polarisation of as high as 75% at 5 K [87,88] .

3.3.4 Spinel ferrites oxides

Spin-filtering has been observed in all of the spin-filter materials described thus far in the previous sections, though all at temperatures well below room temperature due to the low T_{Curie} of the FIs. In recent years, in the quest of achieving spin-polarisation by spin-filtering at room temperature, spinel ferrites have been considered as the best candidates as their magnetic and electronic properties are most appropriate for high temperature applications. The spinel ferrites are mixed oxides with the general formula XFe2O4, where X is a divalent transition metal cation such as Fe^{2+}, Mn^{2+}, Ni^{2+}, or Co^{2+}. All are insulating and ferromagnetic, with the exception of Fe_3O_4, with T_{Curie} above 500 K. While the conductive Fe_3O_4 has been most widely studied as a half-metallic electrode in traditional MTJs [55], the others have been considered as exciting candidates for room temperature spin-filter tunnel barriers. A detailed description of the spinel structure and their properties is presented in chapter 4.

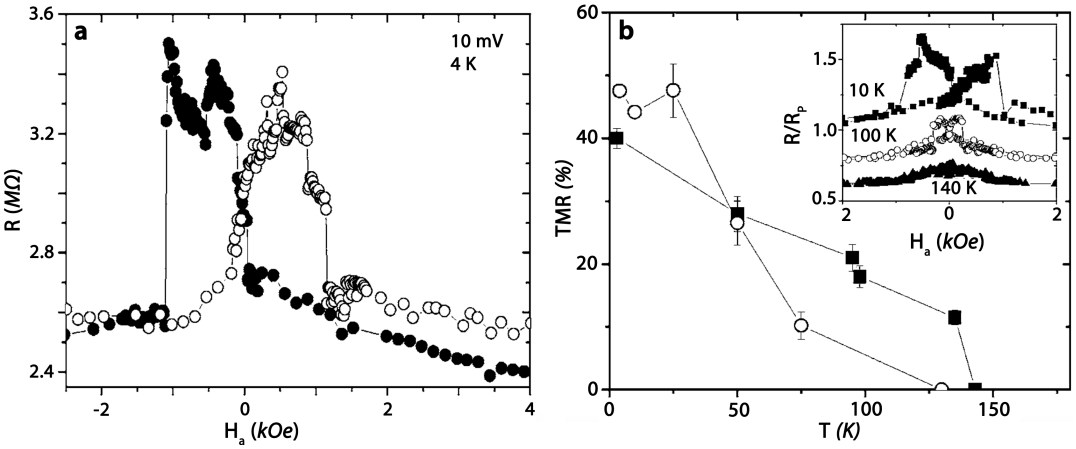

Figure 28 – (a) Typical resistance versus magnetic field dependence of $La_{2/3}Sr_{1/3}MnO_3/NiFe_2O_4/Au$ junction. (b) Temperature dependence of the TMR for a $La_{2/3}Sr_{1/3}MnO_3/SrTiO_3/NiFe_2O_4/Au$ (circles) and a $La_{2/3}Sr_{1/3}MnO_3/NiFe_2O_4/Au$ spin-filter (squares). The inset shows the resistance normalized to the resistance in the parallel state versus field, at several temperatures for the $La_{2/3}Sr_{1/3}MnO_3/NiFe_2O_4/Au$ junction. The curves are offset for clarity. Adapted from [89].

Spin-filtering in a ferrite tunnel barrier was demonstrated for the first time with $NiFe_2O_4$ in $La_{2/3}Sr_{1/3}MnO_3/NiFe_2O_4/Au$ QMTJs [89]. In Figure 28 are shown the results of the TMR measurements at 4 K, which proved that the spinel $NiFe_2O_4$ acted as a filter for the two spin currents. Considering a P_F for the $La_{2/3}Sr_{1/3}MnO_3$ electrode of 90%, the estimated P_{SF} of the FI barrier from Jullière's model was 19%. The latter increased to 22% by decoupling the two ferromagnetic layers with a thin $SrTiO_3$ layer. The positive sign of P_{SF} is not in agreement with the electronic band structure calculations for $NiFe_2O_4$, which instead propose a negative sign. The causes of this discrepancy can be the different effective masses for spin-up and spin-down electrons [89] and the alternative tunnelling pathways, other than direct tunnelling across the electronic band gap, provided by defects in the barrier. Moreover, the TMR signal of these $NiFe_2O_4$-based tunnel junctions rapidly decreases with increasing temperature, as shown in Figure 28b. In fact, above 140 K, well below the expected T_{Curie}= 850 K of

the FI, TMR is no longer observed. This is in net contrast with the predicted capability of ferrite-based spin-filters to produce spin-polarisation up to room temperature. A possible decrease of the FI coercive field at higher temperatures, or a drop in the T_{Curie} of the ferromagnetic electrode caused by non-stoichiometry at interface with the barrier could be the reasons for the vanishing behaviour of TMR for higher temperatures. Additionally, any minor non-stoichiometry in either of the oxide films leading to defect states in the barrier and at the interfaces cause spin scattering events or direct tunnelling without spin-filtering, which become more prominent at higher temperatures and bias voltages. Defect states may also play a role in the observed bias decreasing dependence of TMR, which is not in agreement with the theoretical expected behaviour for a spin-filter [71].

Following these promising but inefficient results on $NiFe_2O_4$, Ramos *et al.* [16] focused on another material from the spinel ferrite family: $CoFe_2O_4$. Tunnelling spectroscopy study of $CoFe_2O_4/MgAl_2O_4/Fe_3O_4$ double barrier tunnel junctions had already revealed good results for the spin-filter efficiency of $CoFe_2O_4$. However, in this work neither the P_{SF} and TMR values were obtained directly but only from from a complex model developed to fit experimental current-voltage curves rather than from direct TM or TMR measurements. A year later, Ramos *et al*. reported for the first time a direct measurement to unequivocally demonstrate the spin-filter capabilities of $CoFe_2O_4$. The fully epitaxial growth of $Pt/CoFe_2O_4/\gamma\text{-}Al_2O_3/Co$ tunnel junctions, by oxygen-plasma assisted molecular beam epitaxy onto sapphire substrates, demonstrated successful spin transport measurements at high temperatures.

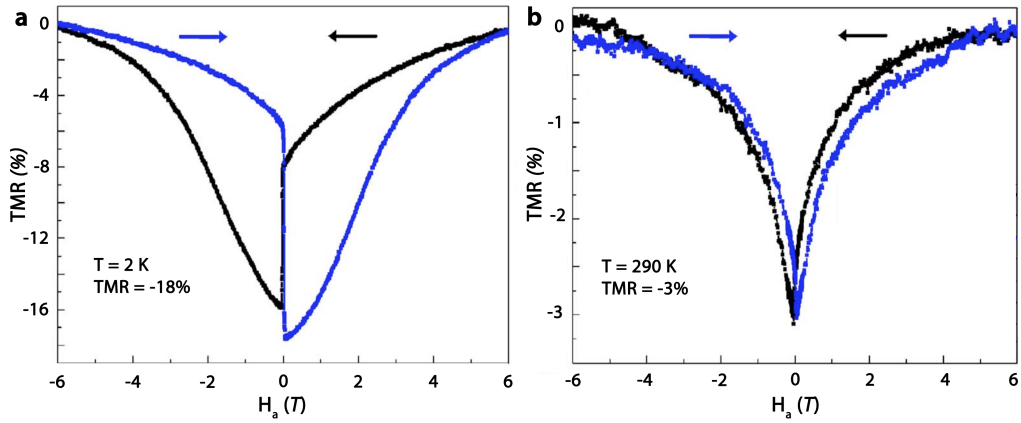

Figure 29 - TMR as a function of applied magnetic field for a Pt(20 nm)/CoFe2O4(3 nm/γ-Al_2O_3 (1.5 nm)/Co(10 nm) tunnel junction at 2 K (a) and at room temperature (b). Adapted from [16].

The TMR signal was -3% at room temperature and increased to -18% at 2 K, as shown in Figure 29. Jullière's model calculation with a 40% spin-polarisation of the Co electrodes, which is decoupled from the $CoFe_2O_4$ by the thin γ-Al_2O_3 layer, estimated a P_{SF} at room temperature and at 2 K to be -4% and -25%, respectively. In this case, the negative sign of P_{SF} is in agreement with band structure calculations. Also, the bias-dependence of the TMR showed the expected behaviour for a spin-filter with an increase to a certain value followed by a decrease for increasing bias voltage.

It may be noted that, although some degree of spin-filtering was achieved, the spin-polarisation remained quite low in comparison with what could be expected from a spinel ferrite spin-filter. This is, once again, due the possible defects at the barrier, arising from oxygen vacancies or antiphase boundaries, influencing the magnetic order of the ferrite. The same group demonstrated in $CoFe_2O_4$-based tunnel junctions via TM method the predominant effect of oxygen vacancies on the spin-filtering capabilities of $CoFe_2O_4$; by increasing the oxygen pressure during the growth of the ferrite barrier, P_{SF} increased from 6% to 26%. This systematic increase in P_{SF} revealed that in the presence of oxygen vacancies, defect states in the FI band gap lower the effective tunnel barrier height, create spin-scattering centres, and are less exchange split, resulting in a reduction in the spin-filter efficiency.

TM technique was later on used to study the spin-filtering capabilities of $MnFe_2O_4$ magnetic tunnel barriers [15]. $MnFe_2O_4$ is another promising candidate as a room temperature spin-filter. Its predicted $2\Delta_{ex}$ of 3.85 eV [90] is higher than the one for $NiFe_2O_4$ (1.21 eV) and $CoFe_2O_4$ (1.28 eV), thus $MnFe_2O_4$ could lead to better spin-filtering efficiencies. The measured Zeeman split dI/dV curves of the Pt/$MnFe_2O_4$/γ-Al_2O_3/Al junctions were clearly asymmetric, proving that the tunnelling current was spin-polarised. A spin-polarisation of up to 9% was extracted from the relative conductance peaks' heights. The positive sign of P_{SF} is in contradiction with the expected negative polarisation for $MnFe_2O_4$ from band structures calculations and the amplitude was once again lower than expected, most likely due to defect states in the barrier, creating parallel spin-independent conduction channels [91–93]. An analysis of the properties of these junctions, with different oxygen pressures during the growth of the ferrite barrier, suggested that the spin-polarisation could be further limited by the presence of defects, other than oxygen vacancies in the ferrite barriers, such as cationic disorder and antiphase boundaries.

In 2012, Matzen *et al*. in 2012 [17] demonstrated that the spin-polarisation in ferrite spin-filters can be increased by limiting the contribution of defects in $CoFe_2O_4$-based nanojunctions, Using the nanoindentation technique [94], the Pt/$CoFe_2O_4$/Al_2O_3/Co junctions were nanofabricated with a lower lateral size of around 5 nm. The following TMR measurements provided a higher TMR ratio with the respect to the results on $CoFe_2O_4$-based micro-junctions by Ramos *et al.* [16]. The room temperature value of TMR was -6%, corresponding to a P_{SF} of -8%, two times higher than the previously reported -4%. To date this is the highest room temperature P_{SF} reported. This work proved that spin-filtering at the nanoscale is more efficient due to fact that the magneto-transport measurements in nanojunctions allow the probing of a single magnetic domain in the spin-filter barrier. Parallel and antiparallel magnetic states are thus very well defined in comparison with micro-junctions, explaining the highest spin-polarisation values. More importantly, the size reduction decreases the number of structural and chemical defects probed in the tunnel barrier, which have hampered the magnitudes of spin-polarisation at room temperature in all the ferrite spin-filters thus far reviewed.

In Table 1 are summarised the main properties of the different FI materials used to demonstrate spin-filtering along with the results obtained via different methods.

Material	T_{Curie} (K)	m (μ_B)	Crystal Structure	E_g (eV)	$2\Delta E_{ex}$ (eV)	P_{SF} (%)	Method	$T_{measurement}$ (K)	Ref.
EuS	16.6	7	FCC	1.65	0.36	80	TM	0.4	[73]
EuSe	4.6	7	FCC	1.80	-	97	TM	0.4	[77]
EuO	69.3	7	FCC	1.12	0.54	29	TM	0.4	[78]
$BiMnO_3$	105	3.6	Perovskite	1.10	0.5 -1.6	22	QMTJ	3	[85]
PCMCO	75	2	Perovskite	-	-	42	QMTJ	4	[86]
SSMO	100	-	Perovskite	0.50	0.60	75	R_j	4	[87]
$NiFe_2O_4$	850	2	Spinel	0.98	1.20	22	QMTJ	4	[89]
$MnFe_2O_4$	573	5	Spinel	-	3.85	9	TM	0.4	[15]
$CoFe_2O_4$	858	3	Spinel	0.80	1.28	8	QMTJ	300 K	[17]

Table 1 – Review of the materials and methods used to achieve spin-filtering.

3.4 Antiphase boundaries

The potential application of ferrite spinel oxides in spintronics devices relies on the assumption that the transport and magnetic properties in thin films are similar to those in the bulk material. As presented earlier, spinel ferrite-based spin-filter device have not yet demonstrated high efficiency at room temperature due the formation of defects at the interfaces of the ultrathin barrier, which are detrimental for electronic and magnetic properties. Among these defects, APBs are one of the most common defects known to affect the epitaxial growth of ferrite thin films. Transmission microscopy experiments have revealed their existence in spinel Fe_3O_4 thin films and various studies have shown that APBs have relevant effect on the magnetic [21,95], transport and magneto-transport properties [96–99].

APBs are stacking faults of the atomic planes in the spinel lattice corresponding to half lattice translation of the cationic sublattice. These result from the coalescence of islands with different cationic systems during the epitaxial growth. Studies on Fe_3O_4 have shown that the density of APBs depends directly on the deposition time during film growth: prolonged deposition times result in larger antiphase domains [100]. The presence of APBs creates altered super-exchange interactions via non-bulk bonds and non-bulk bonding angles and distances due to the changed local cationic arrangement and due to the broken periodicity in the cations sublattice [95,101]. As the bond lengths and bond angle between the cation across oxygen sites determine the super-exchange interactions (see chapter 4), a large fraction of the stacking faults generates an additional strong AF coupling at the defect boundary, which opposes to the ferromagnetic coupling. Because of the presence of these AF-APBs, both the magnetic and the transport properties of the films are different from those of the bulk material [102]. Since the formation of APBs is intrinsically related to the growth process of thin films, the anomalous magnetic properties with respect to bulk properties should be intrinsic to these films and independent of preparation technique.

The reduced magnetisation in thin films due to APBs formation is the main drawback in ferrite-based spin-filters as it decreases the conduction band exchange splitting and limit the spin-filter efficiency. In addition, as the works on $CoFe_2O_4$ have shown, APBs also act as preferential conduction channels without any spin-filtering effect, reducing the spin-polarisation of the current tunnelling through the spinel barrier [91]. Transport measurements through a $CoFe_2O_4$ nanometric thin film by conductive AFM have confirmed that the existence of a non-tunnelling non-spin-conserving transport channel across the barrier can explain the low efficiency of $CoFe_2O_4$-based spin-filter [92,93].

3.5 $LiTi_2O_4$ as electrode in spin-filter devices

The ensemble of results obtained from $NiFe_2O_4$, $MnFe_2O_4$, $CoFe_2O_4$ based tunnel junction for room temperature spin-filtering confirmed the critical importance of mastering the structural and chemical quality of the spinel spin-filters in order to obtain results at higher temperature, and in particular above room temperature. The promising results obtained by Matzen *et al*. in spin-filter nano-junctions and explained by the decrease in the APBs density [17], are encouraging for spin-filtering applications at room temperature. In this context, the control of the growth of ferrite ultrathin films without APBs appears particularly crucial in order to get higher spin-polarisation. As APBs are natural growth defects, resulting from the fact that the lattice constant of the ferrites is, due their complex cation arrangement, almost double (a≈0.83-0.85 nm) [12] that of the metallic layers (Au, Pt, $LaNiO_3$, $La_{2/3}Sr_{1/3}MnO_3$) and substrates conventionally used in spin-filter devices, the search of more suitable substrates and electrodes offers promising perspective in the quest of obtaining higher spin-polarisation, by promoting the growth of ultrathin ferrite films with reduced APBs. In particular, achieving high spin-filter efficiencies at room temperature may therefore be dependent on overcoming structural and chemical defects in ultra-thin (<5 nm) epitaxial spinel ferrites films to be used in complex oxide heterostructures.

The objective of this thesis is to explore the use of a spinel substrate ($MgAl_2O_4$) and a spinel electrode ($LiTi_2O_4$) in fully isostructural all-spinel spin-filter tunnel junctions as a way to reduce APBs. $LiTi_2O_4$ is one of the few conducting spinels that also has superconducting properties (critical temperature $T_C \sim 13$ K) and, more importantly, it has a lattice parameter (a=0.8405 nm) closely-lattice matched to those of the spinel $CoFe_2O_4$ ferrite and of the spinel $MgAl_2O_4$ (a=0.8080 nm) substrate. The lattice mismatch to the latter is -3.8% while to $CoFe_2O_4$ (a=0.8392 nm) [12] is only +0.2%. This makes $LiTi_2O_4$ a very good candidate as oxide electrode in an isostructural spinel tunnel junction.

Chapter 4. Spinel oxides

The following chapter reviews the spinel crystal structure and the magnetic and electronic properties of $CoFe_2O_4$, the spinel ferrite used in this research project as FI barrier. Moreover, as the main aim is to prove the suitability of $LiTi_2O_4$ as electrode in a spin-filter, an overview of its magnetic and electronics properties is given in the last part of this chapter.

4.1 The spinel crystal structure

A unit cell of the face-centered-cubic (fcc) spinel structure has general formula unit AB_2O_4, where A is divalent metal cation (such as Li^{2+},Fe^{2+}) and B is trivalent metal cation (such as Fe^{3+},Co^{3+},Mn^{3+}, Ti^{3+}). The space group of the system is $Fd\bar{3}m$. A cubic-close-packed array of 32 oxygen atoms and a distribution of 64 tetrahedral and 32 octahedral available interstitial sites compose the unit cell. The A^{2+} and B^{3+} cations reside at the centre of 1/2 of the tetrahedral 1/8 of the octahedral, respectively (Figure 30). This unit cell contains eight formula units of AB_2O_4. The perfect normal spinel structure and the inverse spinel structure are two variants of spinels and are usually described by $B_yA_{1-y}[B_{2-y}A_y]O_4$, where y is the inversion parameter and brackets indicate those cations occupying the octahedral positions. When the B^{3+} cations occupy all the tetrahedral sites, and an equal proportion of the remaining A^{2+} and B^{3+} cations occupies the octahedral sites, the spinel is perfectly inverted ($y = 1$). Between these two ideal structures, a cationic disordered mixed spinel structure quantified by y can be observed.

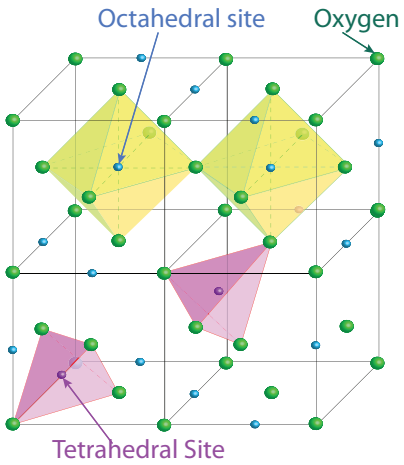

Figure 30 – The spinel crystal structure. Each tetrahedral site is occupied by one metal with four nearest-neighbour oxygen atoms. Each octahedral site is occupied by one metal with six nearest-neighbour oxygen atoms.

4.2 $CoFe_2O_4$ – Crystal structure and physical properties

There exists a wide range of properties across a broad range of temperatures for spinel oxides with 3d transition metals on the octahedral sites, such as ferromagnetism,

antiferromagnetism, charge ordering and other types of electronic and magnetic ordering. In particular, room temperature magnetism occurs with high iron-content in spinel oxides, which are termed ferrites. These mixed spinel oxides are of interest for spintronics applications and have a general formula XFe_2O_4, where *X* is a divalent transition metal cation, such as Fe^{2+}, Mn^{2+} or Co^{2+} and show ferromagnetic-like behaviour and high T_{Curie}. Fe_3O_4, $CoFe_2O_4$ and $NiFe_2O_4$ ideally crystallise in the inverse spinel structure while $MnFe_2O_4$ exhibits the normal spinel structure [103]. The lattice parameters of the different ferrites are close to each other and typical values of the cubic cell parameter are shown in Table 2 together with the T_{Curie}.

	T_{Curie} (K)	a (nm)
Fe_3O_4	*858*	*0.8397*
$CoFe_2O_4$	*793*	*0.8392*
$NiFe_2O_4$	*850*	*0.8339*
$MnFe_2O_4$	*573*	*0.8511*

Table 2 - T_{Curie} and lattice parameters for the spinel ferrites. Values adapted from [12].

The capability of $CoFe_2O_4$ as a candidate for room temperature spintronics applications has already been discussed in chapter 3 where the first spin-filtering effect at room temperature was described. It is a good candidate thanks to its ferromagnetic behaviour, high T_{Curie} (793 K) and good insulating properties. As $CoFe_2O_4$ ideally has an inverse spinel structure, the Fe^{3+} cations occupy 1/8 of the available tetrahedral sites, while 1/2 of the available octahedral sites are filled in equal proportion by the remaining Fe^{3+} and Co^{2+}. Its lattice parameter is a = 0.8392 nm.

The magnetic properties of $CoFe_2O_4$ are formed from several exchange couplings between the different cations. In particular, such interactions are related to the magnetic species on the site as well to the bond angle between the cation and bonding oxygen. Superexchange is a strong (usually) antiferromagnetic coupling between two nearest neighbours cations through a non-magnetic anion (oxygen). Because of the Pauli Exclusion principle both spins on *d* and *p* hybridised orbitals have to be oriented antiparallel. This results in antiparallel coupling with the neighbouring metal cations, as electrons on *p*-orbital of oxygen are also antiparallel oriented. Among the couplings between the spinel ferrites cations, superexchange interactions are the most predominant and involve the *3d* orbitals of Fe^{3+} and Co^{2+} by means of an overlap with the 2*p* orbitals of an intermediate oxygen anion. When the overlap angle is greater than 90° the interaction is strongly antiferromagnetic, whereas when the angle is 90° the interaction is weaker and ferromagnetic (Figure 31). There exits another ferromagnetic interaction contributing to the magnetic properties of $CoFe_2O_4$ and it involves the direct transfer of the $3d^7$ electron in Co^{2+} towards the empty $3d^5$ in Fe^{3+}. This interaction is named double-exchange and it is rather weak compared to the super-exchange interaction [103].

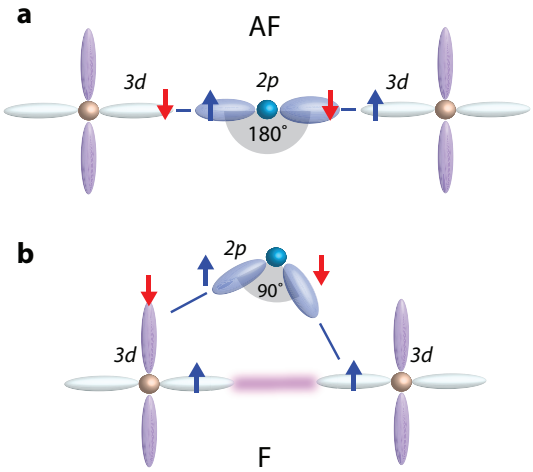

Figure 31 – Schematic representation of the magnetic superexchange interaction in (a) antiferromagnetic and (b) ferromagnetic configuration.

The magnetic moment arising from the Fe^{3+} cations in the octahedral and tetrahedral sites effectively cancels out in the antiferromagnetic coupling. Thus, the net magnetic moment m of an inverse spinel $CoFe_2O_4$ is determined by the moment of the Co^{2+} ions, which is $3\ \mu_B$.

First principles calculations [103] have demonstrated that in the case of an inverse spinel, $CoFe_2O_4$ has a theoretical band gap E_g of 0.8 eV and an exchange splitting of the conduction band of 1.28 eV, confirming its important role to achieve very efficient spin-filtering at room temperature. Additionally, spin-down electrons have a lower tunnel barrier height due to the lowest energy level of the conduction band corresponding to spin-down states, pointing at the fact that a negatively polarised spin-filtering should be observed.

4.3 $LiTi_2O_4$ – Crystal structure and physical properties

Among the spinel oxides, there is only one known metallic spinel oxide to date, $LiTi_2O_4$. It also shows a superconducting transition temperature of 13 K. Superconductivity in such a ternary system was first reported by Johnston *et al*. in 1973 [104] and since then a lot of studies on $LiTi_2O_4$ have been reported. Johnston *et al*. [105] found also that in a solid solution of $Li_{1+x}Ti_{2-x}O_4$ the other end member ($x = 1/3$) is a band insulator, thus it exhibits completely different electronics properties than the metallic superconducting $LiTi_2O_4$ ($x = 0$).

Various powder and single crystal X-ray diffraction and neutron diffraction analyses have shown that $LiTi_2O_4$ belongs to the family of the normal spinel structure [105–107]. The titanium ions have a stronger preference for the octahedral sites relative to the lithium ions, due to their higher charge. In fact, in the $Li_{1+x}Ti_{2-x}O_4$ ternary system, the tetrahedral sites are occupied entirely by lithium ions, while the octahedral sites are occupied by $(2 - x)$ titanium ions and x lithium ions per formula unit. Thus, in $LiTi_2O_4$, Li ions and Ti ions occupy the tetrahedral sites and the octahedral sites, respectively.

For $LiTi_2O_4$ the unit cell constant is a = 0.8420 nm, closely-lattice matched to those of the spinel $CoFe_2O_4$ ferrite and of the spinel $MgAl_2O_4$ (a=0.8080 nm) substrate.

Local density approximation and calculations [108,109] suggest that in the $LiTi_2O_4$ electron band structure the separation between the Ti *3d* orbitals and the O *2p* band is about 2.4 eV. The t_{2g} sub-band of Ti is highly degenerated, remaining in a narrow *d*-band metal with significant electron–electron interaction [110,111]. The Ti sublattice, in mixed valences of Ti *3p* and Ti *4p*, is instead frustrated and favours short-range spin ordering [112]. In addition, in the stoichiometric compound $LiTi_2O_4$ the Fermi level is located at the bottom of the t_{2g} quarter-filled sub-band. $Li_4Ti_5O_{12}$ instead has an empty t_{2g} conduction band and thus shows the properties of a band insulator, rather than a conductive metal, as there are no electrons left in the conduction band. This difference between $LiTi_2O_4$ and $Li_4Ti_5O_{12}$, suggests that a metal-to-insulator transition must occur at intermediate x composition. Figure 32 depicts the phase diagram of $Li_{1+x}Ti_{2-x}O_4$ evaluated from the experimental data available since the preliminary studies on the ternary system [105,113,114]. The critical composition x~0.15 marks the disappearance of the superconducting properties and is thought to be due to grain boundary effects [115–117].

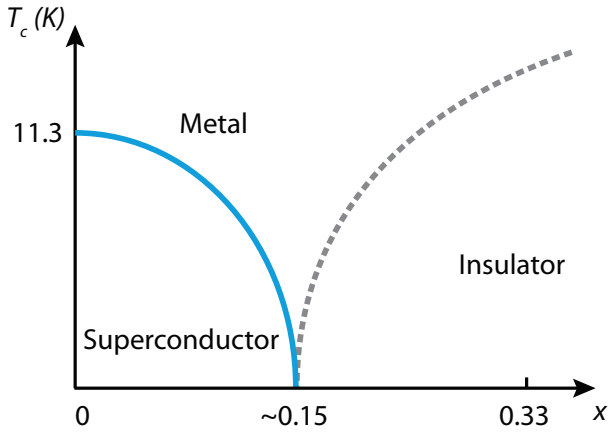

Figure 32 – Phase diagram for the $Li_{1+x}Ti_{2-x}O_4$ system.

BCS superconductivity with s-wave pairing symmetry with medium electron-phonon coupling (λ_{el-ph}= 0.65) has been proposed to fit $LiTi_2O_4$. Nevertheless, an enhanced DoS has been unveiled by magnetic susceptibility [105] and specific heat measurements [118], indicating that *d-d* electronics correlations cannot be ignored in this system. Although superconducting properties of bulk $LiTi_2O_4$ have been investigated extensively, the lack of sample reproducibility and the availability of single crystal and high quality thin films [119,120] have hampered the development of research experiments in order to better understand this spinel oxide. Recently, high quality epitaxial $LiTi_2O_4$ thin films have been successfully grown by pulsed laser deposition [121–123]. This allowed to perform transport measurements on high quality epitaxial [001]-oriented $LiTi_2O_4$ films [124]. The data indicated a twofold in-plane angular dependent positive magnetoresistance and a quadratic dependence of the energy gap on the applied magnetic field ($\Delta \sim -H_a{}^2$), which

are possibly related to a spin and orbital fluctuation effect. Moreover, investigations of the superconductivity on $LiTi_2O_4$ thin film surfaces have been explored by means of an in-situ scanning tunnelling microscope (STM) analysis and revealed a modified superconductivity on the surface, originating from the formation of a pseudogap in the DoS [125]. The main physical parameters of $LiTi_2O_4$ are summarised in Table 3.

T_c	Δ	ξ_S	ξ_{GL}	λ_{GL}	H_{c1}	H_{c2}
(K)	**(meV)**	**(nm)**	**(nm)**	**(nm)**	**(mT)**	**(T)**
11.5-13	*1.93*	*14.9*	*4.47*	*160*	*26*	*16*

Table 3 – Main physical parameters of $LiTi_2O_4$. Adapted from [118,124].

Chapter 5. Experimental methods

In the following chapter, the technique of pulsed laser deposition is described in terms of fabrication of epitaxial complex oxide thin films. Structural properties, phase and surface morphology of the deposited film were investigated by X-ray diffraction, atomic force microscopy. Surface chemical composition was analysed by angle-resolved photoelectron spectroscopy. In addition, the magnetic properties of the samples were measured by vibrating sample magnetometry, and the transport measurements were performed in cryogen-free measurement system. A brief description of these characterisation techniques is presented in the last part of this chapter.

5.1 Pulsed laser deposition

Pulsed laser deposition (PLD) is a physical vapour deposition (PVD) technique extensively used for the thin film growth of a wide variety of oxide materials [126,127]. It is based on the interaction between intense laser nanosecond-pulses and solid matter, which allows the stoichiometric composition transfer from a target to the sample. For laser pulse energy per unit area (fluence) of the order of ~ 1 J/cm^2, the illuminated area of the target is superheated, allowing a change in phase from solid to weakly ionized plasma and the formation of a highly directional plume of material escaping the surface of the target [128]. The result is the deposition of a partial monolayer of the material on the substrate upon which it condenses and the thin film grows [129,130]. This process can occur in ultra high vacuum (UHV) or in the presence of a background gas (e.g. O_2, N_2O, mixture of Ar/O_2, etc.). The background gas is an important parameter for the oxidation process. Fluence can be controlled by varying the size of the laser-illuminated area on the target and the energy of the laser pulse [131,132]. The substrate is heated to elevated temperatures to improve surface diffusion and facilitate the growth of a crystalline film of the target material. Conversely, growth temperatures should also be controlled in order to prevent equilibrium re-evaporation of the material from the as-deposited thin film.

The plasma expands three dimensionally towards the substrate, with the greatest pressure gradient normal to the surface. This means that the elements of the plume with higher velocities are those near the normal of the surface of the target. As a consequence, thin films grown on substrates placed at the centre of the plume show an increased surface roughness than those placed at the edge of the plume [131]. Another drawback of on-axis deposition is the formation of droplets of molten target material on the surface of the film [133]. Crystallisation of the deposited film depends also on the pulse repetition rate, as the time between two pulses should be higher or equal than the time required for the crystallisation of the ablated material to occur [131]. Films can be grown of the desired thickness by controlling the number of pulses, once the growth rate of the material is determined. Further details about the physical principles of PLD can be found elsewhere [128,134].

A schematic of the basic geometry of the PLD deposition chamber used for the deposition of complex oxide thin films is shown in Figure 33. A pulsed KrF excimer laser (Coherent Inc., λ = 248 nm) is focused on one of the six targets placed inside an UHV chamber via a window and by means of an optical path consisting of four mirrors with 90% reflectivity and a convex focusing lens. Substrates are placed on a (Neocera Inc.) conductive heater and silver paste is used to ensure thermal contact between the two. A temperature controller (Eurotherm 2408 PID) sets the desired ramping rate and stabilises the desired temperature during growth.

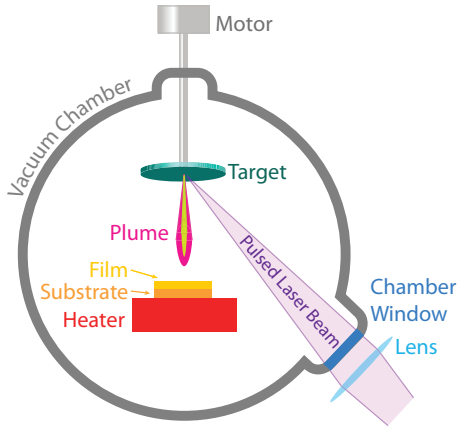

Figure 33 – Schematic of a basic Pulsed Laser Deposition System.

Before deposition the system was pumped down and baked overnight. The base pressure was better than $7x10^{-7}$ Torr. The surface of the target material was always pre-ablated before thin film deposition, in order to obtain a steady-state and avoid target surface enrichment of the less volatile component if there is one element that is more volatile than others [129]. During deposition the target carousel was continuously rotated at constant speed in order to obtain ablation from a more homogeneous target area rather than a single spot. The 10x10x1 mm and 10x5x1 mm $MgAl_2O_4$ (111)-oriented substrates (CrysTec GmbH) were cleaned by bathing and ultrasonication in acetone followed by isopropanol (IPA). Prior to loading into the PLD chamber, substrates were sprayed with a nitrogen airbrush with acetone and, finally, IPA.

5.2 Thin film and device characterisation

5.2.1 X-Ray diffraction

X-ray diffraction (XRD) analysis was performed on the PLD grown thin films to determine phase, crystallographic orientation and epitaxial quality. X-rays have a wavelength λ between 0.1 and 10 nm which is comparable to the distance a between planes in crystals and thus can be used to produce diffraction patterns, according to Bragg's Law [135] on constructive interference:

$$l\lambda = 2asin(\theta)\,, \tag{76}$$

where l is an integer number and θ is the angle between the incident beam and the crystallographic plane. Bragg's Law states that the path length difference between X-rays hitting parallel atomic planes must be a multiple of their wavelength to add constructively; otherwise the transmitted beams cancel one another out (Figure 34).

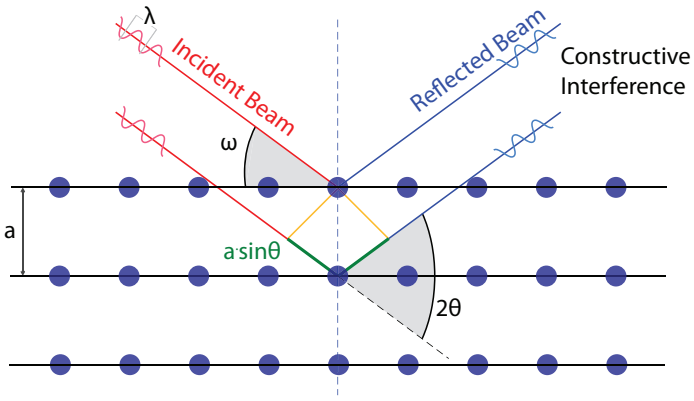

Figure 34 – Illustration of the constructive interference according to Bragg's Law.

The XRD patterns of the films were collected with a PANalytical high-resolution X-ray diffractometer with Cu-Kα_1 radiation (λ = 0.154 nm), a hybrid monochromator, a four-axis rotation system (2θ, ω, χ, φ) and z height motor controller. A schematic of the setup is shown in Figure 35: the incident beam is generated in an X-rays tube (described in section 4.2.4), restricted in size by a divergence slit and focused on the sample; the transmitted beam at different angles is detected after being monochromated.

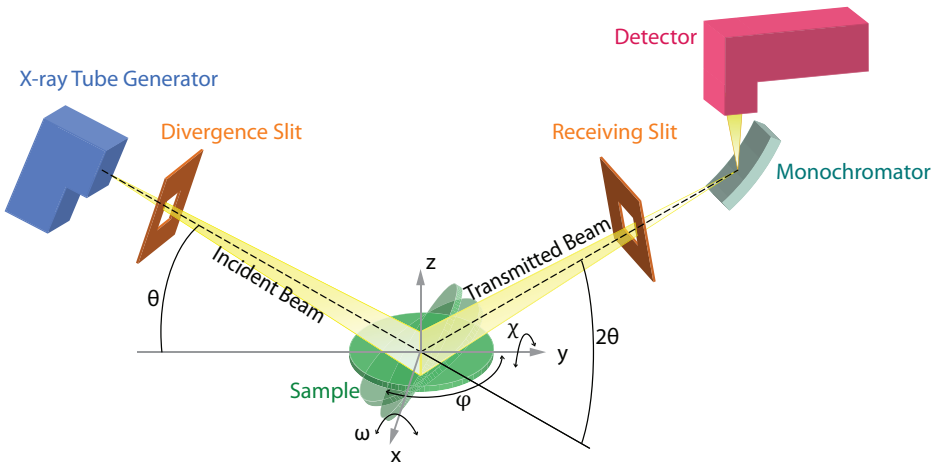

Figure 35 – Schematic illustration of an X-ray diffractometer.

Out-of-plane and in-plane lattice parameters were respectively calculated from $2\theta/\omega$ scans and reciprocal space mapping (RSM). The latter gave also information on the in-plane lattice parameter matching between substrate and film.

5.2.2 X-Ray reflectivity

X-ray reflectometry (XRR) was used to determine thin films thicknesses. XRR is based on the principle of total reflection and the interference of X-rays reflected from two interfaces. The refractive index of air n_{air} equals unity, whereas the refractive indices of thin films are lower than but very close to unity, in the case of X-ray radiation. In particular, the refractive index n_{film} is given by:

$$n_{film} = 1 - \delta - i\beta \,, \tag{77}$$

with δ being the scattering dispersion coefficient and β the absorption of the film material.

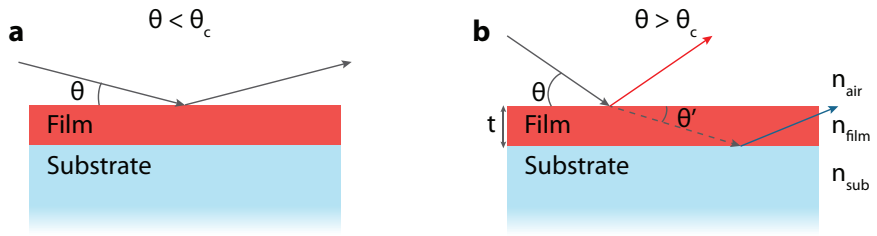

Figure 36 – X-ray total reflection and refraction at the surface of a thin film deposited on a substrate: (a) for incident angles lower than the reflection critical angle, all the incident X-rays are reflected. (b) Incident X-rays are transmitted into the film for angles higher than the reflection critical angle.

The Snell–Descartes law, relating the angles of incidence θ_1 and refraction θ_2 between two different media (n_1 and n_2), is

$$n_1 cos\theta_1 = n_2 cos\theta_2 \,, \tag{78}$$

and, in case of an incident X-ray beam with angle θ from air into a thin film (as shown in Figure 36), can be rewritten as:

$$cos\theta = n_{film} cos\theta' \,, \tag{79}$$

with θ' the diffracted angle. In the limit of an absorption free material ($\beta = 0$) and in the limit of total reflection ($\theta' = 0$), the previous equation reduces to:

$$1 - \delta = cos\theta_c \approx 1 - \frac{{\theta_c}^2}{2} \,, \tag{80}$$

where θ_c is the critical angle of incidence below which the total internal reflection occurs.
Snell's law, Equation (77), can be thus rewritten as:

$$1 - \frac{\theta^2}{2} = \left(1 - \frac{{\theta_c}^2}{2}\right)\left(1 - \frac{\theta'^2}{2}\right), \tag{81}$$

implying that the relationship between the incident angle θ and the diffracted angle θ', via the critical angle θ_c, for low incident angles, is:

$$\theta'^2 = \sqrt{\theta^2 - {\theta_c}^2}\,. \tag{82}$$

Finally, the modified Bragg's Law (see Equation (76)), requiring that the path difference between the reflected waves should be an integer of the incident wavelength, reads:

$$2t\sqrt{sin^2\theta_l - sin^2\theta_c} = l\lambda\,. \tag{83}$$

In XRR scans, the incident X-rays are reflected from all the interfaces between materials with different refractive index (i.e. different electron densities) [136–138] and give rise to interference fringes, called Kiessig fringes [139], at angles determined by Equation (83). The difference between two consecutive maxima

$$sin^2\theta_{l+1} - sin^2\theta_l = \frac{(2l+1)\lambda^2}{t^2}\,, \tag{84}$$

gives the following relation:

$$(2l+1)\lambda^2 = 4t^2(sin^2\theta_{l+1} - sin^2\theta_l)\,. \tag{85}$$

According the to Equation (85), the (square) thickness t^2 of the film can be evaluated by calculating the gradient of the linear fit between $(sin^2\theta_{l+1} - sin^2\theta_l)$ and $(2l+1)\lambda^2$, as shown in Figure 37.

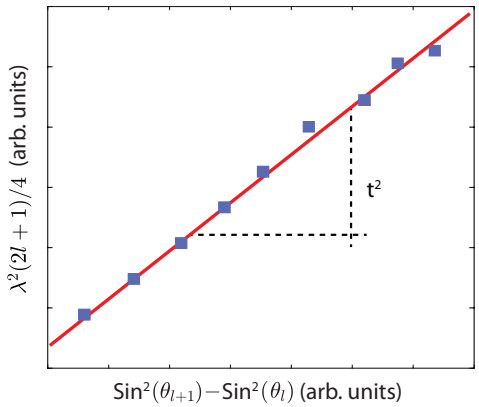

Figure 37 –The slope of the linear dependence between the positions of the intensity maxima versus the Kiessig fringe order l is used to estimate the thickness t of the thin film.

X-ray reflectometry (XRR) was performed on a Bruker D8 diffractometer with $\theta/2\theta$ scans. The sample was rotated in the range from the critical angle to 5˚-6˚ while the detector was rotated at double angular velocity. The obtained fringes-pattern was then analysed and fitted with the previous model and also with a simulation software (Leptos, Bruker Ltd) to determine film thickness and roughness. The latter was then compared with the value estimated from topographical images obtained by atomic force microscopy, as described in the following section.

5.2.3 Atomic force microscopy

The surface topography of the as-deposited thin films was examined by a (Bruker Ltd) Multimode atomic force microscopy (AFM) with a Nanoscope V controller and used in tapping mode.

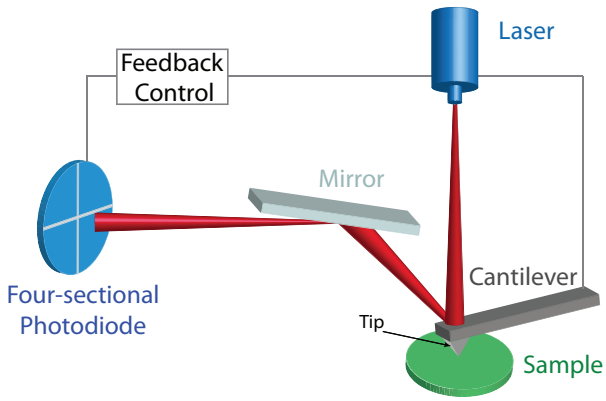

Figure 38 – Schematic illustration of the basic components of an AFM.

The topographical image of the sample surface is obtained by scanning the specimen with a silicon tip (with a radius smaller than 10 nm) attached to a cantilever. As shown in Figure 38, a laser beam is reflected towards a detector system (four-sectional photodiode) from off the back of the aluminium-coated cantilever, allowing to monitor its deflection, i.e. the tip height, while being raster-scanned across the sample surface [130,140]. The tip is oscillated at a frequency close to its

resonance frequency ($f_0 = 300\ kHz$) by a piezoelectric element. When brought close to the sample surface, the oscillation amplitude of the tip is modified due to the interaction between the atoms at the end of the tip and those at the surface of the sample. A feedback circuit keeps the amplitudes of these oscillations always constant (tapping mode) by changing accordingly the height of the sample. The AFM topography image is thus constructed from the changes in height collected across the scanned area.

All collected data was analysed with WSxM software [141] to evaluate the root mean square (RMS) roughness of the samples [142].

5.2.4 Angle resolved-X-ray photoelectron spectroscopy

Surface chemical cation composition analysis of the films was performed by X-ray photoelectron spectroscopy (XPS), a technique that can measure elemental composition, empirical formula, chemical state and electronic state of the elements within the surface of a material. In XPS the sample is irradiated with a monochromatic beam of photons with energy hv. Due to the photoemission effect discovered by Albert Einstein in 1921 [143] the core electrons with binding energy (BE) less than the energy of the photon are ejected. A hemispherical analyser measures the energy distribution of the emitted electrons depending on their kinetic energies by changing their direction with an electric field. Photoelectron spectroscopy is usually done in a UHV environment, since the electrons would be scattered by gas molecules if they were present. The kinetic energy measured by means of XPS is directly related to the binding energy of the photoemitted electron from its core according to Einstein's Law on photoemission:

$$BE = hv - (E_k - W_0)\,, \tag{86}$$

where E_k is the kinetic energy of the photoemitted electron (referenced to E_F); BE is the energy needed to promote a core electron to the E_F; W_0 is the difference between the vacuum energy level E_{vac} and E_F and is called workfunction (Figure 39a). BE differs for every element, atomic orbital and chemical environment of the atom. Thus, the energy and intensities of the photoelectron peaks that appear in the analyser output (Figure 39b), corresponding to the many photoemitted electrons, enable identification and quantification of the surface elements of the sample. In detail, the sharp lines in the XPS spectrum arise from electrons that escape the film without suffering inelastic collisions with the atoms. When collisions happens, a background on the high BE side of the peaks appears.

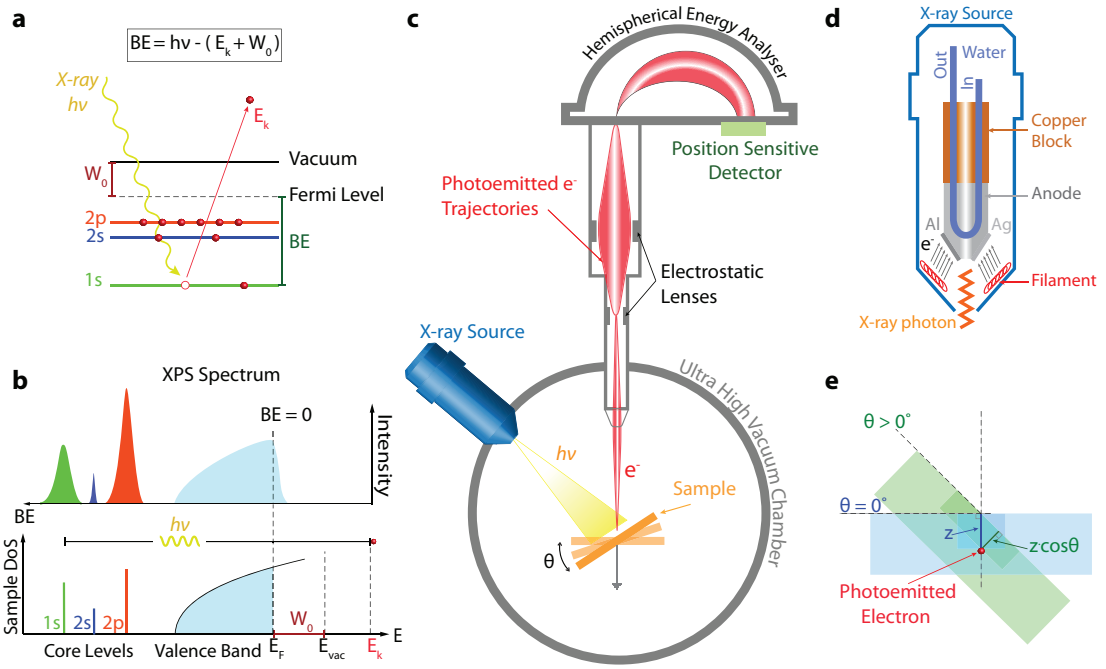

Figure 39 – (a) The photoelectron emission effect and (b) the way it relates to the XPS spectrum. (c) Illustration of the basic components of an AR-XPS and (d) of a tube X-ray source. (e) Greater surface sensitivity is achieved by collecting electrons at more grazing emission angles.

Illustrated in Figure 39c are the basic components required to carry out spectroscopic analysis. A source of monochromatic photons, a UHV chamber where the sample is located, an electron energy analyser, a detector and a data analysis system. The X-ray source is usually a standard X-ray tube in which a filament is heated and by thermionic emission the electrons are accelerated by a potential difference of 15-20 keV toward a water-cooled anode head (Figure 39d). The X-rays are then emitted from the anode due to the relaxation of occupied higher energy levels into the unoccupied/holes lower energy levels created by the accelerated electrons. Weaker X-rays and background continuous Bremsstrahlung radiation can be reduced to obtain sharper $K\alpha$ lines by reflecting the beam on bent quartz crystal that acts as a monochromator, at the expense of intensity [144].

In XPS, for an electron emitted at a depth z below the surface, the intensity for collections normal to the surface $\mathbb{I}$ is attenuated according the to Beer-Lambert law [145,146]:

$$\mathbb{I}(z) = \mathbb{I}_0 e^{-\frac{z}{\lambda_{IMFP}}}, \tag{87}$$

where λ_{IMFP} is the inelastic mean free path of an electron in a solid and $\mathbb{I}_0$ is the intensity from an infinitely thick sample. Such an exponentially decreasing relation indicates that about 95% of the signal will emanate from a depth of less than 3λ. The λ_{IMFP} depends on the kinetic energy of the electrons and the material being analysed. The 'Universal curve' for the electron mean free path in solids [147] (Figure 40) shows that photoelectrons with E_k in the 10-10^3 eV have λ_{IMFP} from 1 to

3.5 nm (highlighted area). Therefore the XPS sampling depth $3\lambda_{IMFP}$ is typically 3-10 nm. In most materials, for the Al-Kα radiation (1486.6 eV), λ_{IMFP} for electrons emitted is about 3 nm.

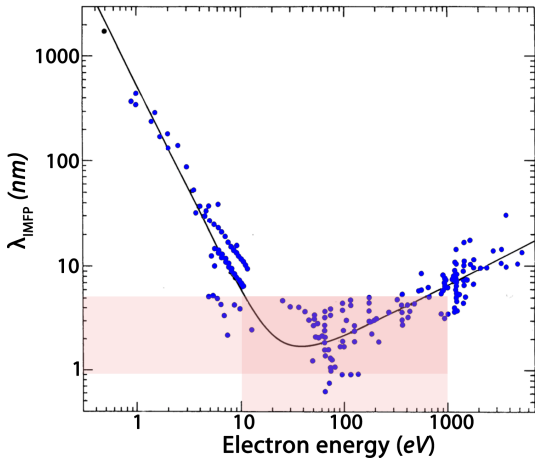

Figure 40 – Universal curve for the electron mean free path in solids as a function of electron kinetic energy. Each data point represents a different element or transition. Adapted from [147].

If electrons are collected at angles other than 0° with respect to the surface normal, the depth of emission is decreased by factor of $cos\theta$, as shown in Figure 39e. Thus, Equation (87) becomes:

$$\mathbb{I} = \mathbb{I}_0 e^{-\frac{d}{\lambda_{IMFP} \cdot cos\theta}}, \tag{88}$$

which implies that the analysis depth d can be varied if the XPS signal is collected over a range of angles from normal emission to near grazing emission. By tilting the substrate, angle-resolved XPS (ARXPS) is a technique that collects spectra for various angles at which the electrons are collected. This enables electron detection from different depths and provides non-destructive information about the thickness and composition of ultra-thin films [148].

For multi-element surface layers XPS can also provide semi-quantitative measurements that are as accurate as ±10%. The photoelectron intensity for an element j in a homogeneous material can be described by

$$\mathbb{I}_j = \mathcal{K} N_j \sigma_j \lambda_{IMFP_j}, \tag{89}$$

where N_j is the average atomic concentration of element j in the analysed surface, σ_j is the photoelectron cross-section of element j, $\mathcal{K}$ accounts for all other factors related to quantitative detection of a signal (e.g. transmission function of the analyser, instrument constant, etc.) and is often assumed constant. Thus, the atomic fraction of an element j in a multi component material can be estimated using the ratio between the integral intensity of the XPS peaks (i.e. peak areas):

$$N_j = \frac{\mathbb{I}_j / F_j}{\sum_i \mathbb{I}_i / F_i} \quad , \tag{90}$$

where F is the relative sensitivity factor $F_j = \sigma_j \lambda_{IMFP\,j}$. The Scofield Cross-section Factors (σ) have been calculated for each element from scattering theory, specifically for Al-Kα and Mg-Kα radiation [149], allowing the determination of N_j from the previous equation.

In our setup the source was a SPECS XR 50 high intensity twin anode, made of Al and Ag coating on silver. The X-ray source is carefully designed so when one anode is in use there is minimal radiation produced by the other anode, minimising cross contamination. The results shown in this thesis were collected using the Al-Kα source (1486.6eV). The monochromator and the analyser used were a SPECS Focus 500 ellipsoidal quartz mirror and a SPECS Phoibos 100 analyser, respectively. The UHV chamber operational pressure was always better than 10^{-9} Torr. Data analysis was carried out using CasaXPS 2.3.15 software.

5.2.5 Electronic transport measurements

Electronic transport analysis of unpatterned thin films was carried out by using a custom-built dipstick probe in a liquid helium dewar. Current-voltage measurements were performed in a current-biased four-point configuration [150] between room temperature (~290 K) and liquid helium temperature (~4.2 K). The sample was attached to a custom-made sample holder with varnish glue and electrically connected to the pads by Al ultrasonic wedge wire bonds (~25 μm in diameter). The same pads were then used to contact the current and voltage leads. The temperature of the sample was controlled by slowly varying the depth of the probe inside the dewar and was measured by a LakeShore 332 temperature controller by means of a Cernox thermocouple, placed in close proximity with the sample and within the probe itself. All measurement equipment was controlled via a LabView program.

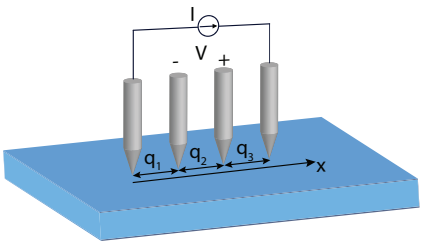

Figure 41 - Schematic of a four-probe resistivity measurement setup for electronic transport measurements of a thin film.

In this setup a constant current (typically lower than 0.1 mA), supplied by a current source, passes through the outer contacts while the potential difference is measured across the inner ones by a

voltmeter. This allows the indirect measurement of the resistance of the sample as a function of temperature $R(T)$. The arrangement of probes is shown in Figure 41 where q_i are the spacing between the probes. The use of this four-point configuration cancels out the effects of contact resistance between sample and leads allowing more accurate resistance measurements [151]. Moreover, if the thickness of the film is smaller than the spacing of the leads ($t \ll q$) and provided none of the probe is too close to an edge of the sample, the sheet resistance of the film is given by

$$\rho = \frac{V}{I}\left[\frac{2\pi}{\frac{1}{q_1}+\frac{1}{q_3}-\frac{1}{q_1+q_2}-\frac{1}{q_2+q_3}}\right], \tag{91}$$

which for equally distant probes, reduces to:

$$\rho = \frac{V}{I} 2\pi q \, . \tag{92}$$

If a temperature lower than 4.2 K was required or electronic transport measurements in an applied magnetic field had to be performed, a cryogen-free measurement system by Cryogenics Ltd with a base temperature of ~1.5 K and an applied magnetic field of up to 9 Tesla was used. A description of the cooling circuit and main components of this system is presented in section 4.2.7.

5.2.6 Magnetic measurements at room temperature

Vibrating sample magnetometer (VSM) was used to analyse the thin films room temperature magnetic properties. In-plane and out-of-plane measurements were usually done on 5x5 mm^2 samples with a Princeton Micromag™ 2900 VSM. A schematic of the setup is shown in Figure 42. The sample was fixed to a sample rod with vacuum grease and centred between the two poles of an electromagnet generating a maximum homogenous magnetic field of $1\ T$. An oscillator provided a sinusoidal vertical vibration to the rod with amplitude and frequency usually 1 mm and 60-80 Hz, respectively. In a VSM the magnetic hysteresis loop measurement is based on Faraday's Law according to which an electromagnetic force is generated in a coil when a change in flux occurs. Thus, two pick up coils are placed in close proximity of the moving sample in order to detect such electromotive force produced by the oscillating magnetic sample. The magnetic moment $\boldsymbol{m}$ of the sample, at a certain applied external field, is extracted from the scaling of the detected signal by a calibration signal collected on a reference sample.

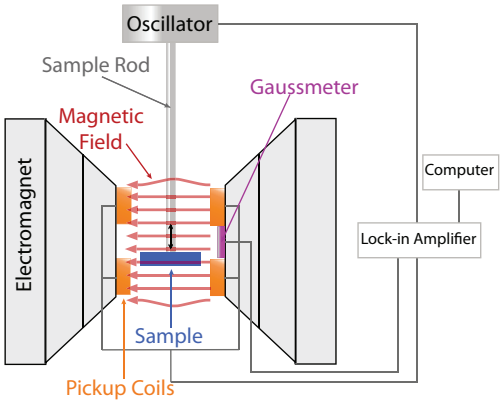

Figure 42 - Schematic of a vibrating sample magnetometer.

The magnetic moment amplitude was always normalized to the volume in order to give the bulk magnetisation, and allow the comparison between the magnetic properties of samples with different thicknesses. In addition, the paramagnetic contribution of the substrate was subtracted from the measured signal. The surface area of the samples was determined by measuring the lateral dimensions to an accuracy of ±0.1 mm using vernier calipers.

5.2.7 Magnetoelectric measurements at low temperature

Low-temperature (down to ~1.5 K) electronic transport measurements of tunnel junctions were performed in a cryogenic-free system (CFS) designed by Cryogenic Ltd. In the CFS the probe is attached at the end of a sample rod and placed inside a Variable Temperature Insert (VTI). A high-field (±9 T) superconducting magnet and the VTI are located in a vacuum-insulated cryostat and cooled down by a closed cycle of helium. A drawing of the system and a schematic of its working principle are shown in Figure 43a-b. He gas, at room temperature, flows from a dump vessel into the system and it is cooled down below its boiling point and condenses into the He pot. Liquid helium is then expanded into an annular tube around the sample space via a needle valve to further cool down to 1.5 K, before being pumped into the dump vessel by a scroll pump.

Though the VTI and the sample space are isolated, the thermal contact between the VTI circuit and the sample space due to the static He exchange gas, cools the sample down. A Lakeshore 340 temperature controller sets the temperature of the sample in the range 1.6-325 K by controlling a heat exchanger and a Cernox thermometer.

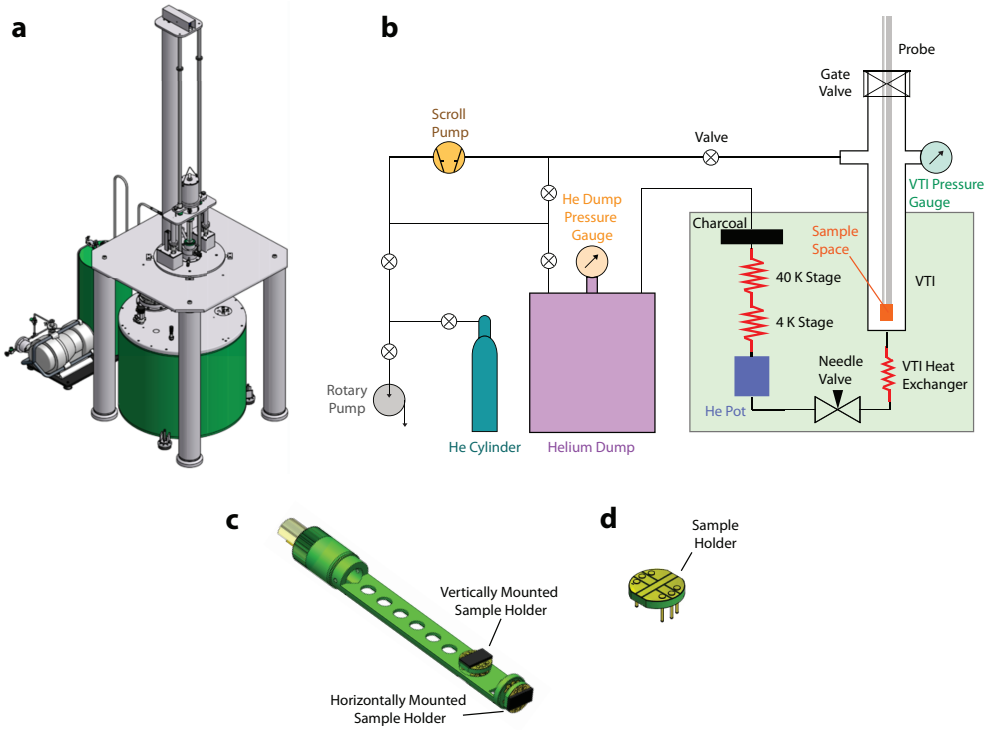

Figure 43 – (a) Drawing of the cryogen-free measurement system and (b) schematic illustration of its main components and cooling circuit. (c) The resistivity probe and (d) the six-contacts sample holder. All pictures adapted from the user manual provided by Cryogenic Ltd.

For transport measurements the sample was glued with varnish glue onto a demountable sample holder (Figure 43d) and then fitted onto one of the two sockets of the probe: one positioned parallel and one perpendicular to the magnetic field (Figure 43c). Al ultrasonic wedge wire bonds provided electrical contact between the holder six-pins and the electrodes of the tunnel junction. Four-points resistance measurements were then performed, at different temperatures and fields, with a Keithley 2400 source meter and a Keithely 2182A nanovoltmeter.

The CFS is also equipped with a VSM and the pick-up coils are located inside the VTI allowing low-temperature magnetic measurements.

Chapter 6. Device fabrication

The as-deposited trilayers were micro-fabricated into micro-pillars with two different techniques. The first one, carried out at the Materials Science Department, Cambridge, involved a single step of optical lithography followed by Ar ion milling to produce micron-scale tracks and millimetre-scale contact pads for wire bonding to chip carriers. The tracks were then patterned with a Ga^+ focused ion beam microscope to achieve vertical transport in pillars with device area of ~0.5x0.5 μm^2. The other fabrication process was carried out by the author of this thesis at INESC-MN, Lisbon. It involved a conventional 3-step optical lithography process with subsequent milling and lift-off steps. The lithography steps patterned, respectively, the bottom electrodes, the pillar and the top electrodes. A detailed description of both microfabrication processes is described in sections 5 and 6 of this chapter, while a brief introduction on lithography, focused ion beam and ion milling is given in sections 1-4. Also, as the deposition of metallic and insulating metal-oxides thin films was required during the fabrication of the tunnel devices, a short introduction to two methods (sputter deposition and ion beam deposition) used to deposit these thin films are presented.

6.1 Photolithography

The two micro-fabrication processes used to micro-fabricate tunnel junctions require at least one step of photolithography. The latter is a process used to transfer a geometric pattern from a mask to the photoresist (PR) on the substrate, as shown in Figure 44. PR is a light-sensitive chemical and it is usually spin coated on the sample, resulting in a uniform thin layer. Chemical changes in the PR occur when exposed to a source of ultra-violet (UV) (λ = 365 nm) light shined through the mask of the required pattern.

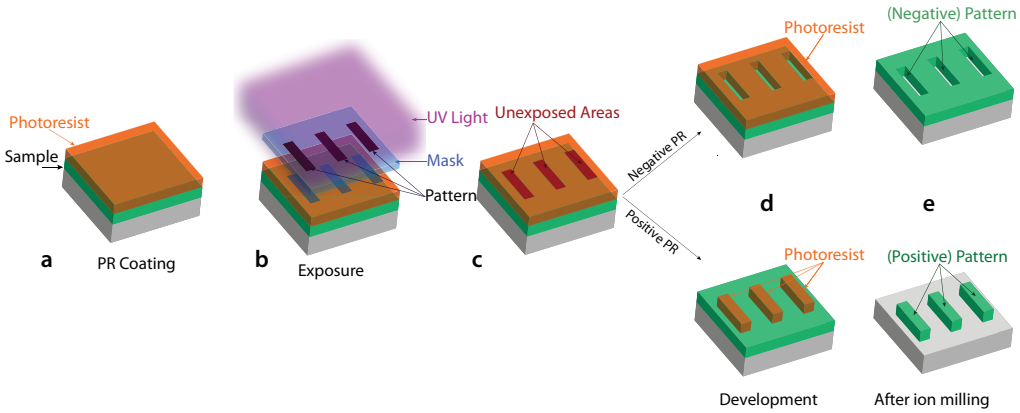

Figure 44 – Schematic of a photolithography process: (a) the PR is spin coated on the sample, (b,c) the required pattern is exposed with UV-light from a mask into the PR, (d) after developing, (e) after ion milling and PR removal for a negative and a positive PR, the pattern is transferred into the pre-grown layers.

When illuminated, a positive photoresist becomes soluble in the developing solution, called developer; in a negative photoresist, unexposed regions are soluble in the developer. Usually, after lithography, ion milling is performed in order to engrave the exposure pattern into the pre-grown films underneath the PR, or a material is deposited in the desired pattern upon the pre-grown films underneath the PR (lift-off). In this work positive PRs were used.

6.2 Direct current and radio frequency sputtering deposition

DC sputtering is a thin film PVD method that involves the bombarding of the target material to be deposited by ionised gas atoms from a plasma. The vaporised target atoms then condense on the substrate forming a thin film [152,153].

The basic setup for a DC sputtering system, shown schematically in Figure 45, consists of the target material placed in a UHV chamber facing the substrate. A negative DC current is applied to target material (cathode), while a positive charge is applied to the substrate (anode). The high purity inert process gas, usually Ar, injected in the chamber after pumping it down to a base pressure, is ionised into Ar^+ by the collisions with the excited electrons flowing from the cathode in to the plasma. The positively charged gas atoms are then attracted to the negative charge of the target material at very high velocities and due to high momentum collision, the sputtering of the target material occurs. The target material fragments cross the vacuum deposition chamber and are deposited as a thin film on the surface of the substrate.

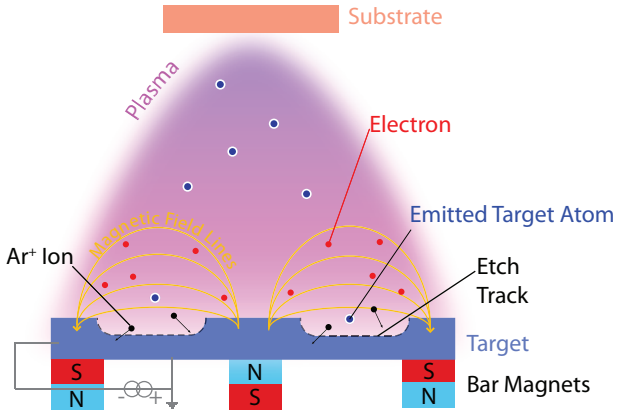

Figure 45 – Schematic illustration of a sputtering system with a DC magnetron source.

To enhance the efficiency of the Ar ionization process and to allow the generation of the plasma at lower pressures, a magnetic field is often used to trap the electrons, and thus also the Ar^+ ions, along an etch-track. As shown in Figure 45, a dc magnetron gun has a series of bar magnets beneath the target that generates the trapping field lines [154].

DC sputtering is limited to the deposition from metal targets that are electrical conductors. This is due to the fact that dielectric target materials, because of their insulating properties, will accumulate on their surface a positive charge, and therefore terminate the process. The charge

build up issue of dielectric materials can be overcome with the use of radio frequency (RF) sputtering where the sign of the anode-cathode bias is varied at high rate (13.56 MHz) to allow the surface of the target material to be discharged at each cycle.

6.3 Ion beam milling and deposition

In this work ion milling was used during microfabrication to etch the undesired portions of the samples and reproduce the mask pattern on the sample. Ion milling is a non-selective anisotropic physical etching technique based on the acceleration of Ar ions from a source onto the surface of the substrate. The impact of the ions transfers momentum to the substrate atoms and then physically dislodges them from the sample, providing the capability to produce patterns with high yields on micron level and minimal pattern variations. This occurs due to the photoresist having a very low milling rate and thus acting as a protection layer for the films underneath against the bombarding ions, as shown previously in section 5.1.

In a miller, schematically shown in Figure 46, the ions are generated from Ar gas by energetic electron bombardment in a discharge chamber, forming a plasma. Electrons are emitted from a tungsten filament (cathode) by thermionic emission and collected by a positively biased (discharge voltage) electrode (anode). Once formed, the Ar^+ ions are accelerated towards a negatively biased grid (grid voltage), towards the sample stage. After the grid, electrons can be introduced in the chamber by a neutralizer filament to compensate the positive charge of the ion beam. The ion beam continuous bombardment of the sample converts the kinetic energy of the ions to heat energy, thus the substrate needs to be cooled, by a water-cooling circuit embedded into the stage, to prevent any damage. The stage usually has azimuthal substrate rotation for milling uniformity optimisation and tilting to adjust the incident angle and the consequent milling rate.

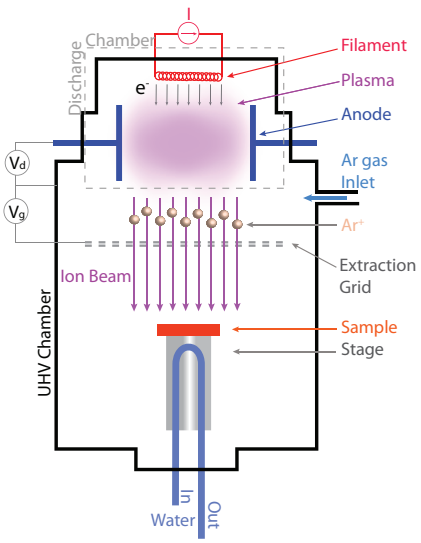

Figure 46 – Schematic illustration of an ion miller system.

The working principle of ion beams described thus far can also be used for deposition of thin films. In an Ion Beam Deposition (IBD) a highly energetic, broad ion beam is focused on a grounded metallic or dielectric target. The sputtered material then coats the substrate tilted toward the target with the sputtered material. The main advantage of an IBD with respect to sputter deposition is that in the latter the ions are generated in the same chamber as the targets and the substrates, whereas in an IBD system the ions are formed in a separate chamber. This ensures depositions at pressures that are one order of magnitude lower than the ones in the sputtering systems. As a consequence the ion density is smaller and therefore so is the deposition rate. Low deposition rates are valuable for the precise deposition of very thin layers.

It is very common to have an IBD system equipped with two ion guns: one directed towards a target carousel for deposition and one (assisted gun) directed toward the sample for milling purposes. The assist gun can also be used to act directly on the substrate to deliver energetic noble or reactive ions in the depositing material, improving the quality of the deposited films.

6.4 Focused ion beam

In principle, a focused ion beam (FIB) system is almost identical to a scanning electron microscope (SEM). However, while the latter uses a beam of electrons to image the sample in the UHV chamber, in a FIB a focused beam of ions is used instead. While a FIB is operated at low beam current for imaging purpose, at high beam currents a nanometric precise milling can be achieved by focusing of the ion beam on the sample surface. Thus, a careful control of the energy and intensity of the ion beam allows precise nano-machining removal of unwanted site-specific material without requiring masking with resists, wet or dry etching or resist removal, as in photolithography.

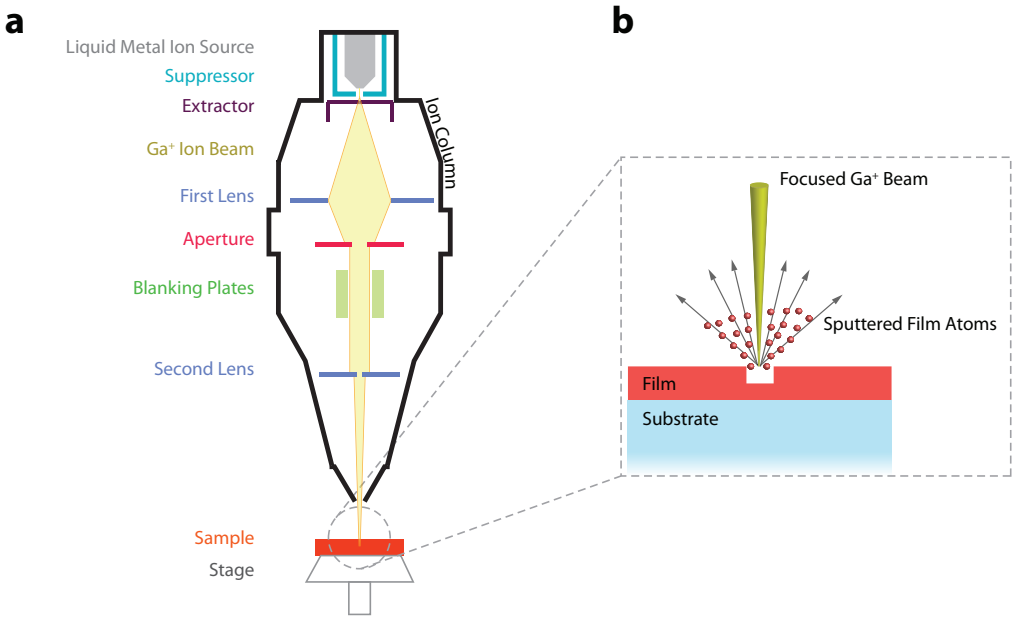

Figure 47 –(a) Schematic illustration of a FIB ion column and (b) of its working principle.

The ion source is usually a liquid Ga source, due to its low melting point (30 ˚C), low volatility and low vapour pressure. A tungsten needle heats the gallium to the liquid state and a high extracting electric field evaporates the ions from the sharp tip of a Taylor cone (~2 nm). As schematically depicted in Figure 47a, Ga^+ ions are subsequently accelerated to energies of 1-50 keV and then, by means of a series of apertures and electrostatic lenses, focused onto the sample.

As the diagram in Figure 47b shows, the Ga^+ ion beam sputters the sample surface due to the transfer of kinetic energy during collisions. Secondary electrons are also emitted from the surface when the beam rasters on the sample surface. The signal from these electrons is generally used to image the sample with high resolution and with a spot size on the order of a few nanometres.

6.5 Fabrication by focused ion beam

6.5.1 Gold deposition

The as-deposited trilayers grown on 10x5x1 mm $MgAl_2O_4$ substrates were covered with a 200 nm thick layer of polycrystalline Au deposited by standard DC magnetron sputtering. This conducting layer reduced the charging of the oxide layers during the FIB milling and served as top contact layer. The system used was a custom made sputtering chamber equipped also with an ion-miller. The chamber was pumped down overnight to obtain a vacuum better than $2x10^{-6}$ Torr. The Au layer was deposited in Ar gas at a pressure of 15 mTorr. The DC power was set to 50 W and the deposition was carried out for 120 s. Prior Au deposition, the sample surface was cleaned by milling the samples in the same chamber and without breaking the vacuum, in Ar gas with 2% O_2 for 30 s at a pressure of 0.2 mTorr. The discharge voltage was set to 42 V and the beam current used was 10 mA.

6.5.2 Photolithography patterning

Au-coated samples were cleaned with an acetone spray followed by an IPA spray and then loaded into a spinner. PR (AZ 4533) droplets were pipetted onto the sample. The spin coating required 25 s of spin at 4.5 krpm to achieve a thickness of ~4 µm at the centre of the sample. At the perimeter of the samples a thicker PR edge formed. Prebaking on a hotplate at 110 ˚C for 60 s followed.

Exposure of the sample was performed in a Karl Suss MJB3 UV300 mask aligner. Firstly, an exposure in contact mode for 90 s of a rectangular mask of dimensions slightly smaller than the size of the substrate in order to remove the edge-bead with the subsequent development in $NaOH:H_2O$ (1:3) solution. The developing time was controlled by several successive optical inspections and it usually was around 30 s. Further, a fine exposure in soft contact mode for 7 s of the CAM 44 mask (the drawing of the mask is shown in Figure 48). Careful optical inspections were performed during development in a 4:1 developer:solvant to make sure that small features were not over-developed

while the unexposed PR was removed. This process patterns a series of 4 µm-wide tracks which are connected to millimetre-scale contact pads for wire bonding to chip carriers.

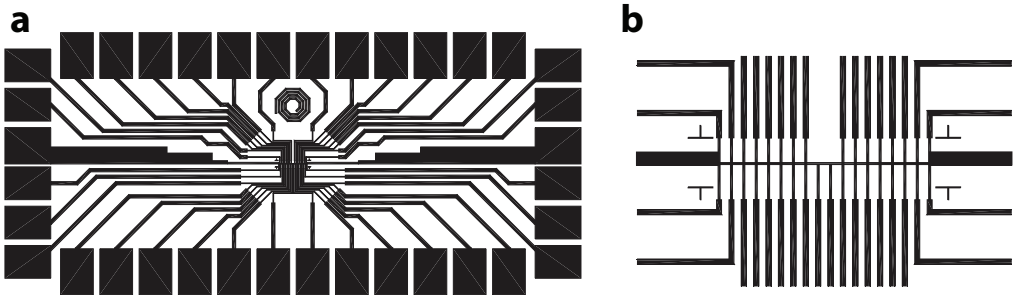

Figure 48 – Drawing of the CAM 44 mask design for 10x5 mm substrate, (a) the large millimetric areas are the contact pads for wire bonding the device. (b) An enlarged view of the centre of the mask showing the 4 µm width tracks.

6.5.3 Ion milling

Ar ion milling followed the lithography steps in order to pattern the tracks onto the deposited trilayers. The inert gas used in the ion miller for the microfabrication of the tunnel junctions by FIB was Ar with 2% oxygen. The small amount of oxygen reacts with the milled PR to form volatile CO and CO_2 to reduce the re-deposition of PR. The system used was equipped with a turbo-pump and a load-lock, thus ensuring reduced pumping times to reach the base pressure of $2x10^{-6}$ Torr. The operating pressure was 0.15 mTorr with a gas flow of 1.4 sccm. The discharge voltage and grid voltage were 42 V and 500 V, respectively. The beam current was set to 15 mA. Sample stage was water cooled and rotated continuously to ensure uniform milling. Milling rate of the different oxides layers were determined by performing calibration milling runs on thick (>400 nm) single oxide layers and measuring the step height of the features using a profilometer. After milling the PR strip was dissolved in acetone in an ultrasonic bath.

6.5.4 Focused ion beam fabrication

The 4 µm-wide central tracks patterned on the samples were then micro-machined by a FEI200 series FIB to fabricate several nano-pillar devices to achieve vertical transport. Such FIB is equipped with a sample stage that can be nominally rotated between 0˚ and 45˚ with respect to the beam (θ). The use of a custom 45˚ wedge holder allowed for an effective extended rotation of the sample from 0˚ to 90˚. Moreover, the sample stage also rotates 180˚ about a normal axis (φ).

A detailed description of the FIB processing for the nanopillar devices fabrication can be found elsewhere [155,156], while a brief description of the FIB process is presented here.

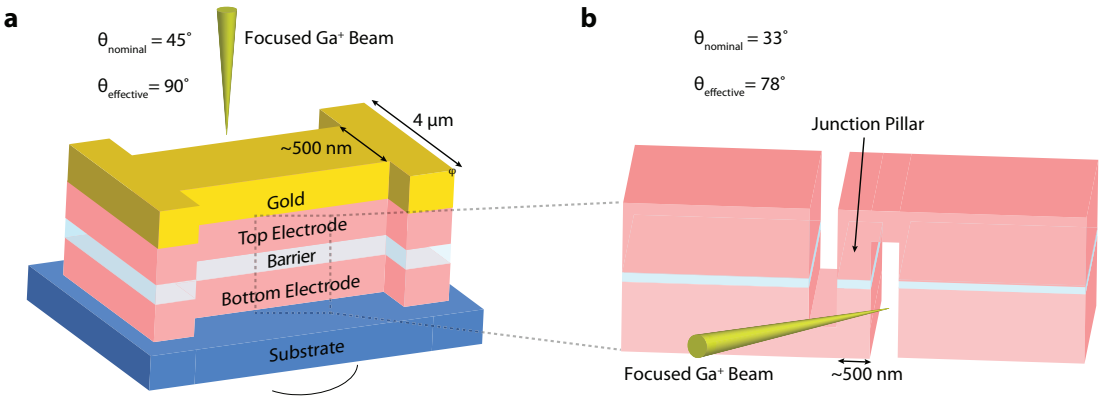

Figure 49 – Schematic of the FIB procedure for device fabrication: (a) narrowing of track from 4 µm to 500 nm with a normal to the sample ion beam, (b) fabrication of the junction pillar with two tilted cuts.

Firstly, the 4 µm-width of the track was narrowed down to 500 nm by milling a box area around both sides of the track with a normal ($\theta_{nominal} = 45^{\circ}$) beam current of 70 pA (Figure 49a). The milling was calibrated by eye thanks to change in image contrast once the substrate is reached. To avoid any shorting between the electrodes a further short milling was done. The actual junction pillar was fabricated by performing two isolating side ($\theta_{nominal} = 33^{\circ}$) cuts with a beam current of 11 pA, see Figure 49b, at a distance of 500 nm. The average lateral dimension of the final nano-pillar thus was 500x500 nm^2.

After the first step, the sidewalls of the track were polished with a beam current of 11 pA using the cleaning tool of the software to remove any possible shorts at the interface due to the Ga implantation that may occur when high beam currents are used.

6.6 Device microfabrication by 3-step lithography

The microfabrication of the tunnel junctions by means of a conventional 3-step lithography process requires first, the patterning of the bottom contact lead, then the definition of the micrometric junction pillar followed by the deposition of the top contact lead, as schematically shown in Figure 50. These steps are described in the next sections.

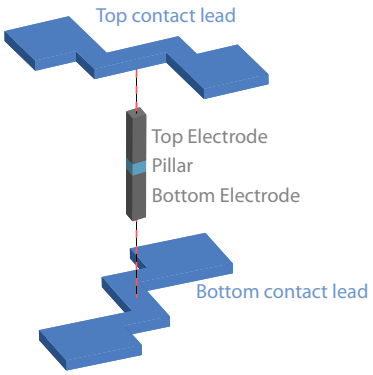

Figure 50 - Exploded schematic of the final tunnel junction structure fabricated by a 3-step conventional lithography process.

A vapour priming step was performed on all samples before lithography in order to increase the uniformity and the substrate adhesion of the PR. This was done by heating the substrates at 130° C in an oven and then exposing it to a hexamethyldisilazane (HMDS) vapour solution. The HMDS ensures the substrate surface is hydrophobic and promotes good PR-to-substrate adhesion.

6.6.1 Bottom contact lead

The coating and the development of the first lithography step which patterns the bottom contact lead were done with an automatic Silicon Valley Group (SVG) coating system. Optical lithography was done with a Heidelberg Direct Write Laser 2.0 (DWL) system equipped with a diode laser ($\lambda = 405$ nm) and grey filters to select the desired output energy. Both machines are made for processing 6-inch silicon wafers, thus the 10x10 mm substrate onto which the oxide trilayers were deposited were taped on a silicon wafer during processing. Moreover, to avoid the formation of edge-bead which affected the small 10x10 samples and the consequent non-uniformity of the PR, samples were placed in a custom-made 6inch rounded sample holder with a square hole in the middle with the right size and height to accommodate the sample and facilitate the coating of the PR to achieve better uniformity.

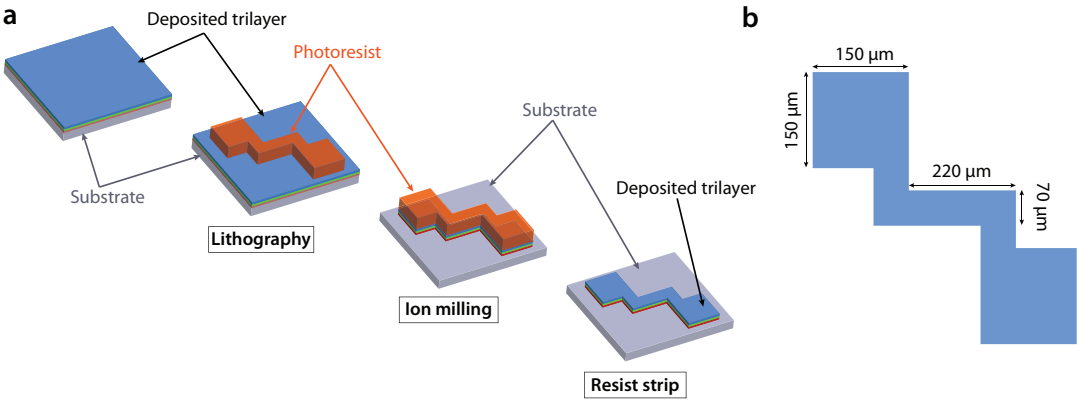

Figure 51 – (a) Schematic of the bottom electrode patterning process before and after lithography, ion milling and resist strip. (b) Autocad mask design to pattern the bottom electrode: the exposure is inverted, thus the PR remains inside the shape after development.

The coating step covered the samples with a 1.5 µm-thick positive PR (PFR7790G27cP) by spinning the sample at 2.5 krpm for 30 s in order to uniformly distribute the photoresist. Samples were then soft baked at 85 ˚C for 60 s in order to evaporate the solvent and relive stresses accumulated in the PR during the spinning stage. The subsequent exposure of the pattern was performed in the DWL with 100 mW power and 70%-90% energy. The mask used was designed in AutoCad and patterned up to 70 devices on each sample. The design of the mask of bottom electrode is shown in Figure 51b. Development (60 s) in the SVG required an initial hard bake at 110˚C for 60 s and was done by washing and drying the samples at high rpm. The pattern was checked by an optical

inspection with a microscope, to ensure that the photoresist was fully developed and had a sharp profile. Samples were then loaded into a Nordiko 3600 IBD system (equipped with a deposition and an assist gun) to perform the first ion-milling step to define the bottom electrodes of the junctions, as shown in Figure 51a. The IBD system used had a 6-target carousel, two neutralisers and was able to process 8 inch-diameter wafers. Calibration etching on high thickness single layers (~300 nm) was performed in order to estimate the milling rate for each layer via multiple profilometer measurements of trenches. The milling process was performed through the entire tunnel junction heterostructures down to the substrate. The Ar gas flow was set to 10 sccm and the working pressure was set to 1.4×10^{-4} Torr. The sample stage was rotated continuously at a speed of 30 rpm to ensure uniform milling. RF power was set to 180 W. The angle between the beam and the wafer used was 70°, in order to provide good etching control and vertical profiles.

After ion milling, the photoresist is removed chemically from the samples with acetone in an ultrasonic bath. Subsequently, the samples were cleaned with acetone and IPA and blown dry with compressed air.

Before the pattering process, to reduce specular reflections, the structure was covered with a 15 nm-thick Ta anti-reflection layer deposited in the same IBD system used for milling.

6.6.2 Junction pillar

The second lithography step is identical to that of the patterning of the bottom electrode, described above, except for the mask used, which now patterns the micro-pillars (Figure 52b). In addition, also the contact pads of the bottom electrode are patterned in order to provide protection from the subsequent oxide deposition (see Figure 52a).

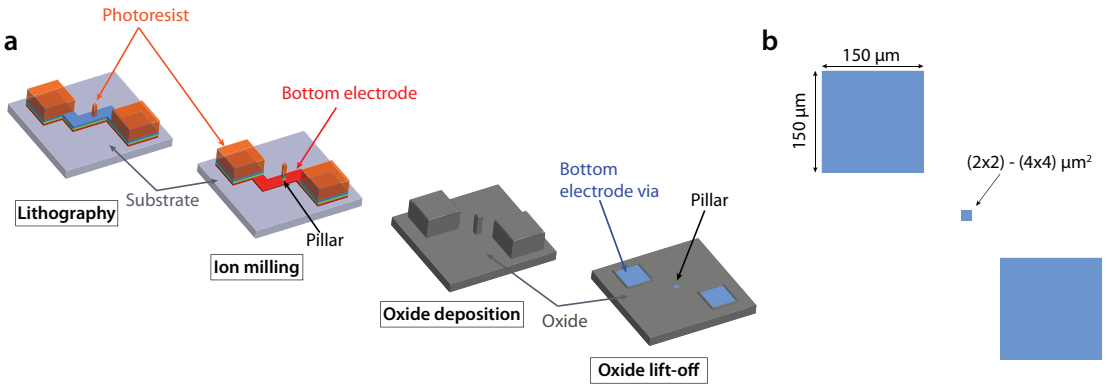

Figure 52 - (a) Schematic of the junction patterning process before and after lithography, ion milling and resist strip. (b) Autocad mask design to pattern the pillar: the exposure is inverted, thus the PR remains inside the shape after development. The design provides also cover for the contact pads for the bottom electrodes during the oxide deposition.

The ion milling which follows the second lithography step is the most critical part of the whole fabrication process. Pillar patterning requires the etching to be stopped right below the barrier/top electrode interface. To ensure a vertical propagation of the mask and preserve the shape and size of

the pillars etching was performed at an angle of 70˚ down to the $CoFe_2O_4$ barrier. As sidewalls re-deposition can be significant in this case, due to the large aspect ratio (feature depth/width), a second, shorter milling step with a lowered beam of incidence (40°) was performed until it penetrated the bottom $LiTi_2O_4$. This ensured a barrier with steep profile and well controlled nominal size, together with the reduction of metallic bridges around the barrier, at the cost of the profile walls in the bottom electrode [157]. Figure 53 shows schematically the shape of the pillar with a vertical profile down to the barrier and increased aspect ratio of the bottom electrode.

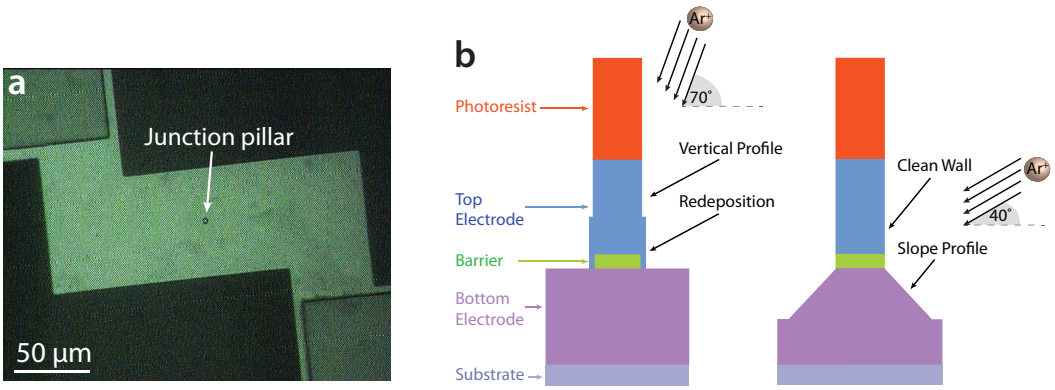

Figure 53 – (a) Optical microscope image of a tunnel junction device during microfabrication. (b) Re-deposition on the sidewalls during milling at high beam incidence angles and increased aspect ratio for the bottom electrode at lower beam incidence angles.

Passivation and later insulation of the pillars were achieved by deposition of a 100 nm-thick Al_2O_3 layer by RF sputtering in a homemade UHV system. The target was a 6 inch diameter amorphous Al_2O_3 wafer near a 4 inch diameter magnetron. The vacuum chamber was pumped down to $6x10^{-6}$ Torr before depositing the film at an Ar partial pressure and flow of $2x10^{-3}$ Torr and 45 sccm, respectively. The RF power was 200 W and the calibrated deposition rate by profilometer measurements of thicker films was 1.1 nm/min.

Lift-off of the buried photoresist from the bottom pads and the top of the pillar was done in acetone in heated (65 ˚C) ultrasonic bath. The samples were checked by multiple optical inspections with a microscope, to ensure a successful lift-off from all the 70 devices in the sample.

6.6.3 Top contact lead

The aim of the last lithography step was to deposit a thick metallic layer in trenched patterns for the top contact of the pillar and the vias to the bottom electrode (see Figure 54a). For this purpose the mask is non-inverted (Figure 54b). Due to the high thickness of the metallic layers, to ensure a non-time consuming lift-off, the PR is pre-developed for 20 s before exposure and after coating. Such a procedure hardens the surface PR and results in a sharper and slightly undercut PR profile after exposing it with higher energies (+10%).

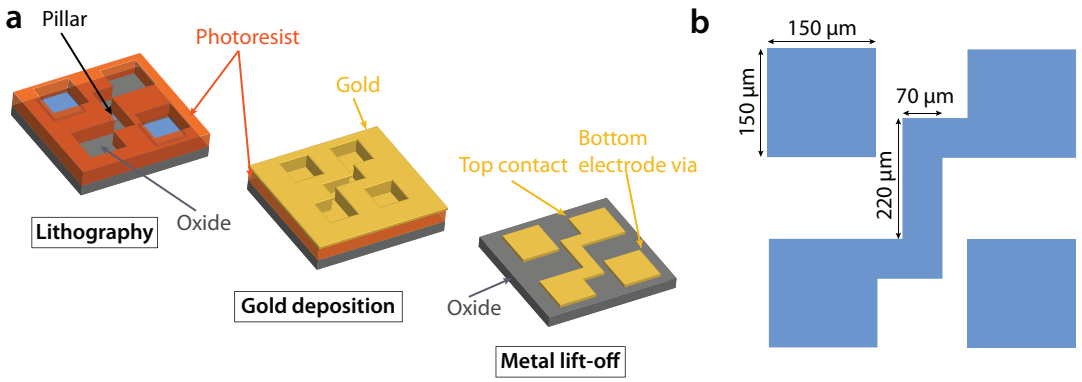

Figure 54 - (a) Schematic of the top electrode patterning process before and after lithography, Au deposition and lift off. (b) Autocad mask design to pattern the bottom electrode: the exposure is non-inverted, thus the PR remains outside the shape after development.

A 10 nm thick Cr layer was deposited on the samples to improve adhesion of the subsequent 100 nm-thick Au. Both layers were deposited in an Alcatel SCM450 multi-target DC magnetron sputtering system without breaking the vacuum. The system can host three 4-inch diameter magnetron targets and it is pumped down a base pressure of $1x10^{-7}$ Torr before deposition. A DC power of 20 W was applied during deposition. The Ar pressure and flow were set to 3 mTorr and to 20 sccm, respectively.

Lift-off follows the same procedures described earlier for the previous pattering steps and in this case requires only a few minutes.

Chapter 7. Thin film experimental results

In the following chapter the results of the magnetic and structural characterisation of the as-deposited $LiTi_2O_4$ and $CoFe_2O_4$ single thin films are presented. High quality surface layers are needed to integrate $LiTi_2O_4$ in a full-oxide spin-filtering device, thus a detailed AR-XPS analysis is reported. Lastly, the entire growth process used to optimise the magnetic and electronic properties of $CoFe_2O_4/LiTi_2O_4$ bilayer samples is presented. These bilayers were deposited with the intention of optimising their structural, chemical and magnetic properties for the insertion into fully epitaxial $LiTi_2O_4/CoFe_2O_4/LiTi_2O_4$ (SIS) and $LaNiO_3/CoFe_2O_4/LiTi_2O_4$ (SIN) tunnel junctions. Here the two top electrodes, $LiTi_2O_4$ and $LaNiO_3$, play the role of superconducting and paramagnetic electrode, respectively.

7.1 Growth of $LiTi_2O_4$ thin films

For the growth of $LiTi_2O_4$ thin films by PLD a $Li_4Ti_5O_{12}$ ceramic target was prepared from a mixture of Li_2CO_3 (Alfa-Aesar) and TiO_2 (Alfa-Aesar) powders by a standard solid-state reaction method [158]. The higher Li/Ti ratio (0.8) of the target was designed to compensate for the high loss of Li during ablation process. This is because volatile elements are scattered by the background gas molecules or by other species in the plasma, or are sputtered from the growing film by more energetic species arriving at the substrate [159]. The $LiTi_2O_4$ thin films were grown in high vacuum (P_{O_2} < 5x10^{-6} Torr), with a laser fluence of 0.7 J/cm^2 and a repetition rate of 5 Hz. The substrate temperature was kept at 800 ˚C during growth (unless stated otherwise) and cooled down to room temperature in vacuum after deposition.

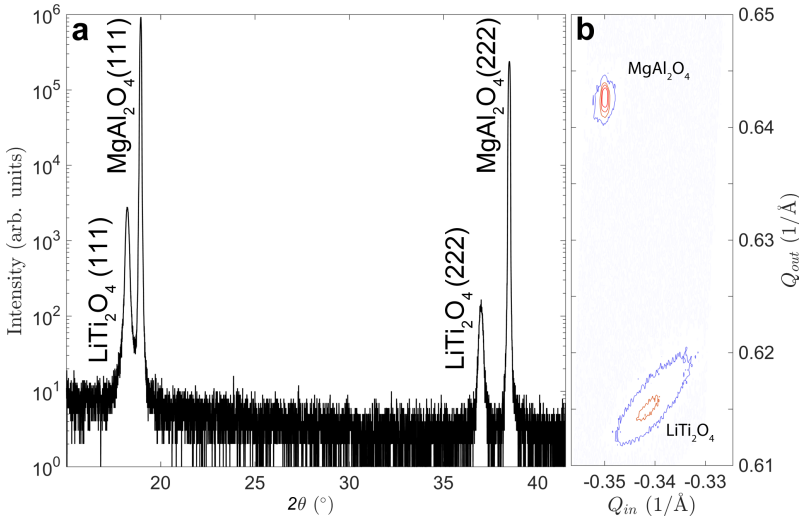

Figure 55 – (a) XRD pattern for the $LiTi_2O_4$ films around the symmetric (111) $MgAl_2O_4$ reflection. (b) XRD RSM of the (531) peak of $MgAl_2O_4$ along with the (531) peak of $LiTi_2O_4$.

To verify lattice mismatch and bulk phase purity of the $LiTi_2O_4$ films, out-of-plane XRD patterns (see Figure 55a) were measured. Single-phase $LiTi_2O_4$ film growth on $MgAl_2O_4$ was confirmed since the spectra showed clear (111) and (222) Bragg's reflection peaks of the film and substrate, with the absence of additional peaks. The average out-of-plane lattice parameter obtained from $LiTi_2O_4$ diffraction peaks position is almost identical to bulk value, *a=(0.8400±0.0002) nm*. The high resolution XRD-RSM, shown in Figure 55b, of the substrate (531) peak and the film (531) peak, reveals that $LiTi_2O_4$ is fully relaxed in-plane.

XRR measurements show Kiessig fringes pointing at smooth film surface and thus, a well-controlled growth. A reflectivity scan of a 27 nm-thick $LiTi_2O_4$ film is shown in Figure 56a together with the simulated fit and with the fit of the oscillations periodicity (Figure 56b). From these fits, the surface roughness of the film was estimated to be ~1 nm. AFM imaging of the sample surface morphology (Figure 56c) provided an estimation of the RMS roughness of 0.8 nm, confirming surface smoothness.

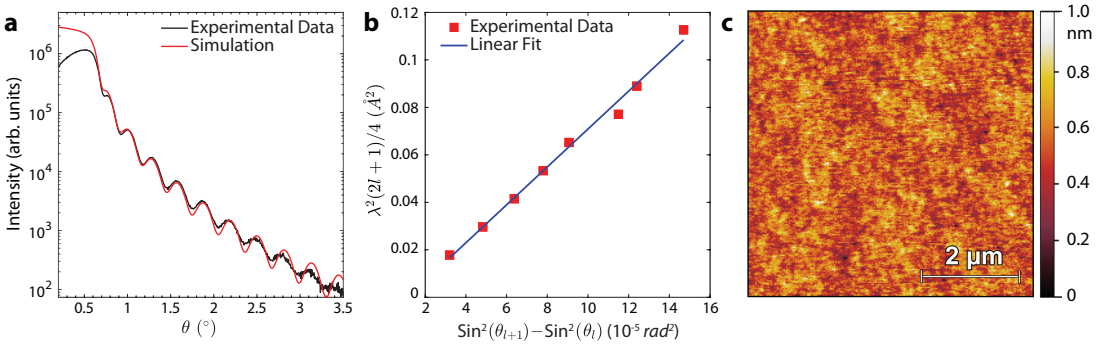

Figure 56- (a) XRR oscillation (black) for a 27 nm $LiTi_2O_4$ film grown on $SrTiO_3$ (110) substrate and the simulated fit (red). (b) Fit of the periodicity of the XRR reflectivity oscillations. (c) AFM image of the same as-grown $LiTi_2O_4$ film.

As reported by Johnston *et al.* [105], electrical properties of the $Li_{1+x}Ti_{1-x}O_4$ ternary system depend strongly on the stoichiometry. Charge transport characterisation on our samples confirmed high quality thin film growth of the superconducting phase ($x \sim 0$) Li-Ti-O spinel oxide. Figure 57 shows the metallic behaviour at room temperature – $\partial\rho/\partial T > 0$ for $T_c < T < 290$ K - and a sharp normal to superconductor state transition (width < 0.3 K) with a T_c of 13.8 K (inset). The Fermi liquid behaviour of the samples resistivity is confirmed by the variation of resistivity as T^2 at lower temperatures (blue line). The residual resistivity ρ_0 and residual resistivity ratio $RRR = \rho_{300K}/\rho_{15K}$ of the films were 330 µΩcm and 2.4, respectively, in accordance with the literature [121–124].

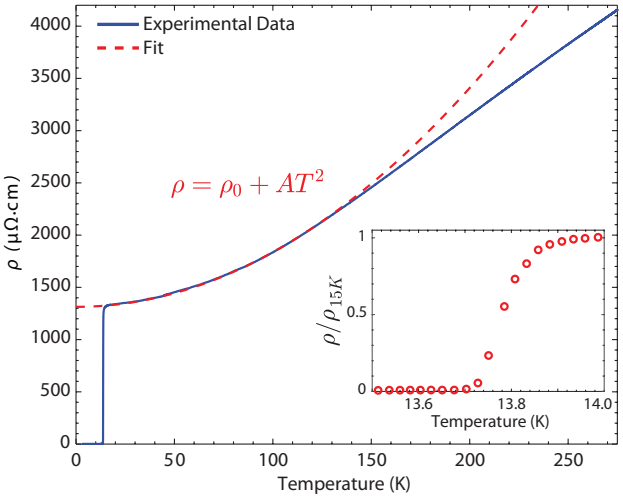

Figure 57 – Temperature dependence of resistivity for $LiTi_2O_4$ film (red-solid line). Blue-dotted line is the $\rho = \rho_0 + AT^2$ fit in the temperature range 40-120 K. The inset shows the transition from normal to superconducting state.

Growth of metallic-superconducting high quality $LiTi_2O_4$ films was possible under certain oxygen partial pressure values. Growth at elevated temperatures, at P_{O2} higher than 1x10^{-5} Torr, yielded insulating films with no superconducting transition. This is known to be due to change in the oxidation state of the Ti cations of $LiTi_2O_4$. In fact the latter has an equal number of trivalent and quadrivalent Ti cations and, for P_{O_2} higher than 1x10^{-5} Torr, Ti^{3+} ions readily oxides into Ti^{4+} ions, leading to the formation of the transparent insulator phase $Li_4Ti_5O_{12}$ [122]. This makes the growth of high quality single crystal thin films by PLD highly sensitive to the oxygen partial pressure P_{O_2} in the chamber [121,122,124,160].

7.1.2 AR-XPS – Lithium out-diffusion

Both XRD and transport measurements strongly indicate that bulk properties of the $LiTi_2O_4$ films are of very high quality. Film surface composition plays a critical role in tunnel devices, thus XPS measurements were carried out in order to determine the surface composition of the deposited $LiTi_2O_4$ thin films. Interestingly, the two different spinel phases, $LiTi_2O_4$ and $Li_4Ti_5O_{12}$, not only have an evident stoichiometric Li to Ti ratio difference, but also the valence state of Ti differs: the average charge of the titanium ions increases from 3.5+ (an equally mixed valence Ti^{3+} and Ti^{4+}) for superconducting $LiTi_2O_4$ to 4+ for insulating $Li_4Ti_5O_{12}$. XPS is hence a very powerful probing method to differentiate between the two oxides and to get a clear understanding of the chemical composition of the film surface layers. Moreover, the probed depth is almost similar for Li 1s and Ti 3s as their binding energies are close to each other: 55 eV and 62 eV, respectively. In addition, any spurious effect arising from the analyser transmission can be neglected so that the Li/Ti and Ti^{3+}/Ti^{4+} intensity ratios can be considered proportional to the ratio between the concentrations.

Spectra were calibrated to the binding energy of C 1s at 284.8 eV and were fitted with Voigt functions for Ti^{3+}, Ti^{4+} and Li peaks to reduce the standard residual between the fit and the

experimental data, using CasaXPS 2.3.15 software. The same fitting parameters were used for all spectra and a Shirley background was subtracted. For chemical quantification, we used the sensitivity factors 0.0568 and 0.473 for Li 1s and Ti 3s [149], respectively.

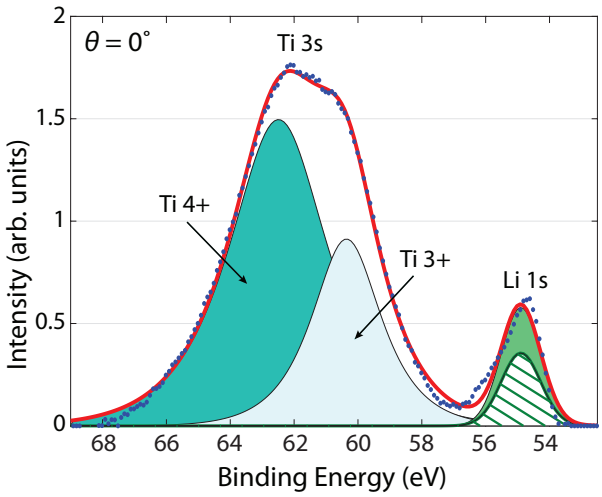

Figure 58 - Measured (dotted-blue) and total fitted (solid-red) Li 1s and Ti 3s XPS bulk-sensitive (θ=0°) spectrum for a 200 nm-thick $LiTi_2O_4$ film grown at 800 ˚C. The areas show the decomposed peak areas for Ti^{4+}(cyan), Ti^{3+}(light cyan) and Li 1s (green). The excess amount of Li present at the surface is clearly visible by comparing the measured Li 1s peak area (green) with the calculated peak area of Li 1s in order to have Li/Ti=0.5 (hatched green).

Figure 58 shows experimental XPS data as well as the fits of Li 1s and Ti 3s peaks of the $LiTi_2O_4$ film at a bulk sensitive emission angle ($\theta = 0°$). The Ti 3s peak is clearly split in a Ti^{3+} (~60 eV) and a Ti^{4+} (~63 eV) component, indicating the presence of $LiTi_2O_4$. However, the spectral weight of Ti^{3+} is much less than Ti^{4+} (Ti^{4+}/Ti^{3+}=2.3) suggesting that $Li_4Ti_5O_{12}$ is present at the surface. The formation of $Li_4Ti_5O_{12}$ is also confirmed by an increased Li/Ti ratio of 0.8 compared to 0.5 for $LiTi_2O_4$. To enhance clarity of the excess surface concentration of Li (green peak area), the total spectral weight of the Li peak in order the have the correct Li to Ti ratio (0.5), taking into account the total Ti concentration, is depicted in Figure 58 by the green-hatched area peak.

To quantify the $LiTi_2O_4$ cation composition of the surface layers, AR-XPS measurements were performed by varying the emission angle with respect to the surface normal and thus allowing control of the probing depth. Ti 3s, Li 3s spectra and their corresponding total fits - normalized to the Ti 3s area peaks - of $LiTi_2O_4$ film collected at various emission angles are shown in Figure 59. By increasing θ (i.e. more surface sensitivity) the intensity of the Li 1s peak increases with respect to Ti, clearly indicating a segregation of Li at the $LiTi_2O_4$ surface.

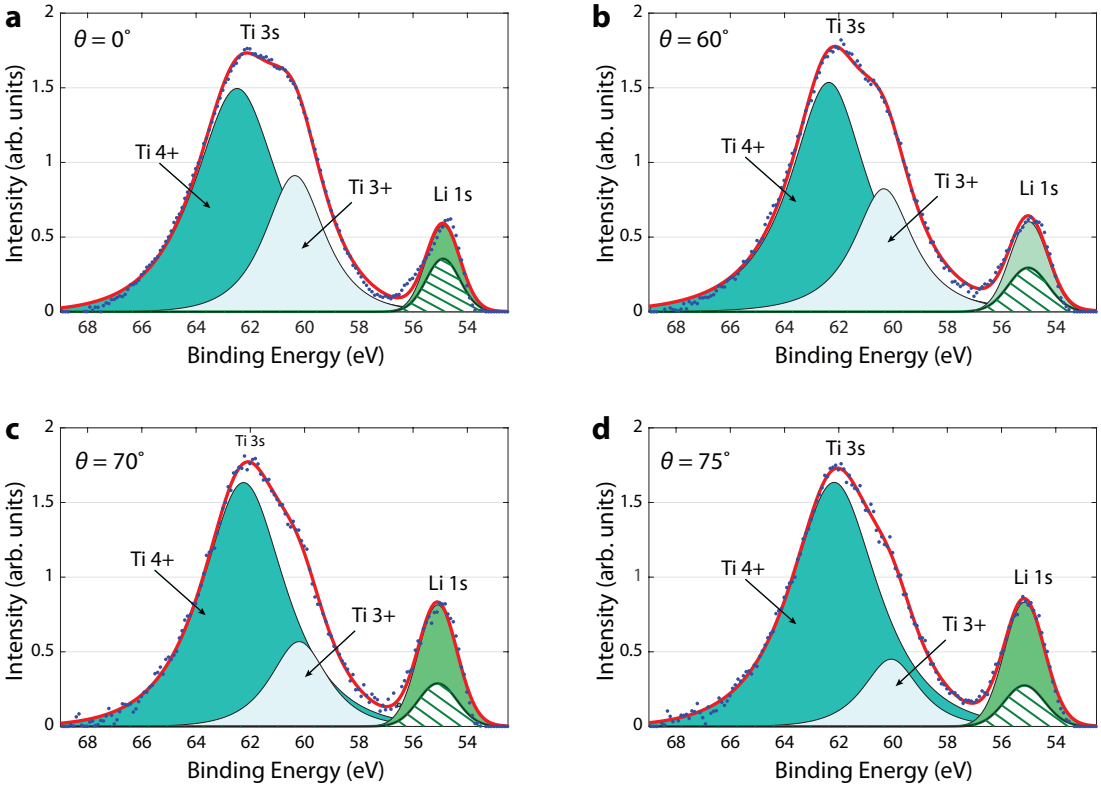

Figure 59 – Measured (dotted-blue) and total fitted (solid-red) Li 1s and Ti 3s XPS spectra collected at (a) θ = 0°, (b) θ=60°, (c) θ=70°, (d) θ=75° for a 200 nm-thick $LiTi_2O_4$ film grown at 800 ˚C. The areas show the decomposed peak areas for Ti^{4+}(cyan), Ti^{3+}(light cyan) and Li 1s (green). The excess amount of Li present at the surface is clearly visible by comparing the measured Li 1s peak area (green) with the calculated peak area of Li 1s in order to have Li/Ti = 0.5 (hatched green).

The increasing behaviour for higher angles can be seen with more clarity in Figure 60, which depicts the overlapped spectra collected at different angles. Moreover, the Li 1s peak shape broadens towards higher binding energy, indicating that Li^+ with a different chemical environment is present at the surface. An increase of the Ti^{4+} component with respect to the Ti^{3+} component with increasing θ is present as well.

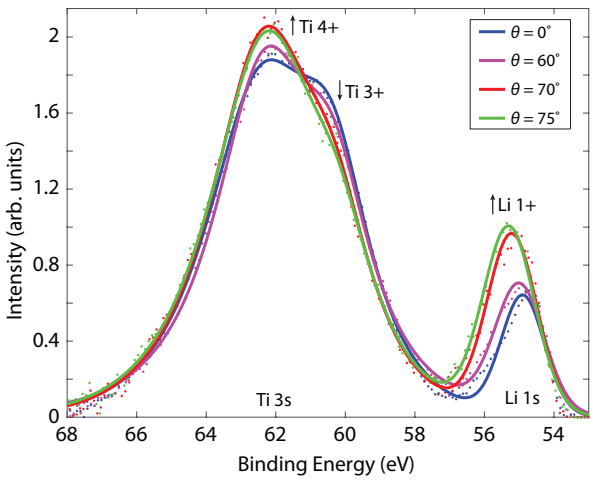

Figure 60 - Measured Li 1s and Ti 3s XPS spectra taken at different collection angles for a 200 nm-thick $LiTi_2O_4$ film grown at 800 ˚C. The arrows indicate the direction of increasing θ. The dots indicate the experimental data; the solid lines are the data envelopes fittings.

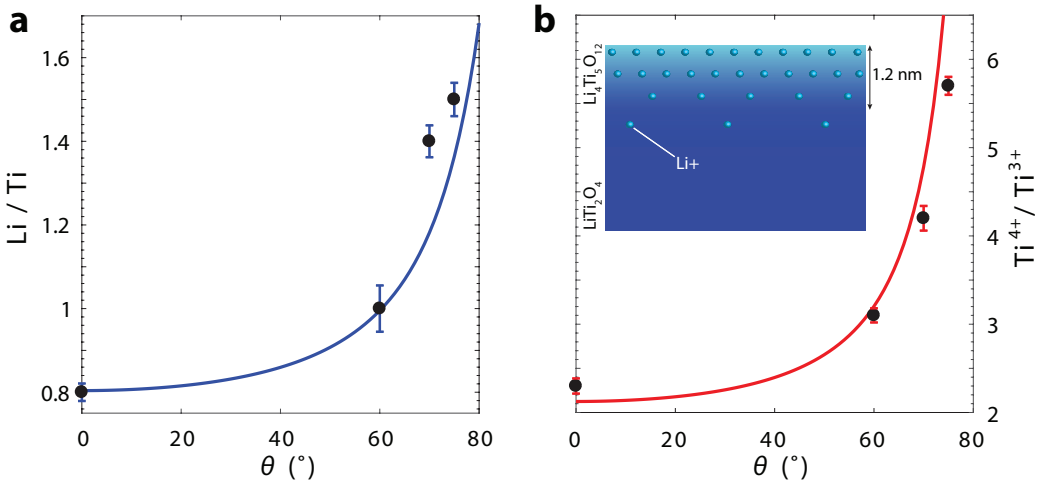

Figure 61 – Measured (a) Li/Ti and (b) Ti^{4+}/Ti^{3+} ratios (black dots) for $LiTi_2O_4$ films. A schematic model of the surface composition used to fit (solid lines) the experimental data is shown in the inset of Figure 61b.

The Li to Ti ratio was calculated for the different emission angles using the spectral weight of the Ti 3s peak and the spectral weight of the Li 1s peak. The clear increase of Li for larger θ is shown in Figure 61a. Since the Li/Ti intensity ratio is larger than 0.5 and not constant with increasing emission angle, it indicates that the top surface layers are disproportionately Li-rich. Ti^{4+} to Ti^{3+} ratios were calculated from the respective components of the fitted Ti 3s envelopes for the different emission angles (Figure 61b). A clear increase of the Ti^{4+}/Ti^{3+} ratio was found at higher emission angles, indicating the presence of $Li_4Ti_5O_{12}$ at the top surface layers.

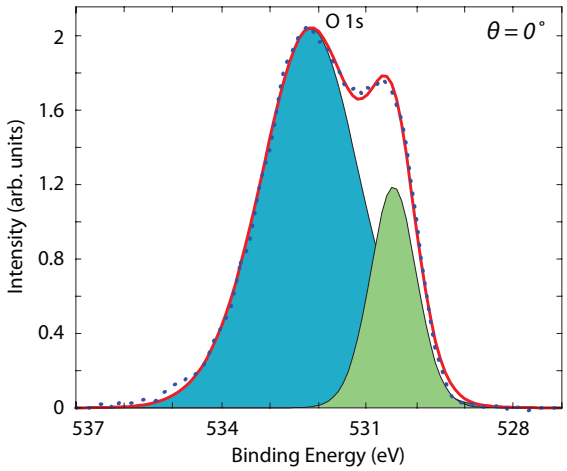

Figure 62 - Measured (dotted-blue) and total fitted (solid-red) O 1s bulk-sensitive (θ = 0°) spectrum. The areas show the decomposed peak areas for metal carbonate (blue) and metal oxides (green).

To resolve the composition of the surface layers, we modelled the observed Li/Ti and Ti^{4+}/Ti^{3+} ratios versus θ. In our model, we took into account that the intensity of the photoelectrons, created at depth z, has a damping factor $exp\,(-z/\lambda_{eff})$, where the electron mean free path (λ) is approximately 2 nm [161]. A surface chemical composition of a mixture of the two different Li-Ti-O spinel compositions, $LiTi_2O_4$ and $Li_4Ti_5O_{12}$, and of an additional Li phase that mimics the excess of Li at the surface, was hypothesized. Here, the additional Li-phase, modelled by simply using Li^+, may

come from $LiCO_3$, LiOH or Li_2O. Note that the presence of Li_2O at the surface could be ruled out, as this phase is accompanied with an O 1s peak at 528.6 eV, which was absent in our films (Figure 62). With this simple model, we found that a good match (solid lines, Figure 61) to the experimental data was found if the bulk of the film is $LiTi_2O_4$ and a thin Li-enriched layer, ~1.2 nm (1.5 u.c.), is present at the surface. More precisely, a mixture of Li^+ and $Li_4Ti_5O_{12}$ would be present at the top surface layer and a $LiTi_2O_4$-$Li_4Ti_5O_{12}$ mixture towards the bulk. The surface composition is schematically depicted in the inset of Figure 61b. The presence of a non-spinel Li^{1+} phase at the top surface layer would also clarify the peak broadening of the Li 1s at higher binding energy for increased emission angles. The Li enrichment at the surface can be understood by considering the increased mobility of Li ions at elevated temperatures as a result of their low activation energy [162]. This leads to an out-diffusion of Li towards the surface that changes the chemical cation compositions of the top $LiTi_2O_4$ layers. Similar Li out-diffusion has been observed in e.g. $LiNbO_3$ crystals [163,164].

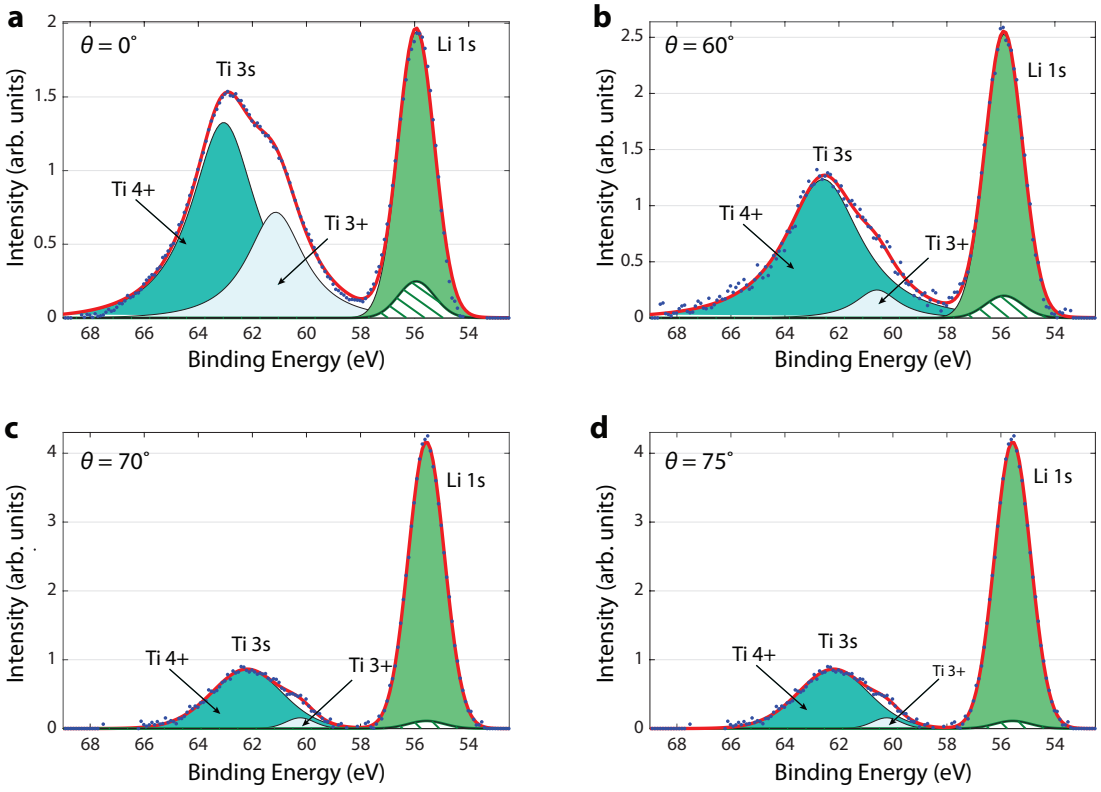

Figure 63 – Measured (dotted-blue) and total fitted (solid-red) Li 1s and Ti 3s XPS bulk-sensitive (θ = 0°) for a 200 nm-thick $LiTi_2O_4$ film grown at 600 ˚C. The areas show the decomposed peak areas for Ti^{4+}(cyan), Ti^{3+}(light cyan) and Li 1s (green). The excess amount of Li present at the surface is clearly visible by comparing the measured Li 1s peak area (green) with the calculated peak area of Li 1s in order to have Li/Ti = 0.5 (hatched green).

To increase the quality of the surface layers, we investigated whether the Li out-diffusion may be reduced by lowering the growth temperature, even though previous studies have shown that low-temperature growth is detrimental for the quality of $LiTi_2O_4$ films [123]. By studying the top surface layers of a film grown at 600 ˚C (showing a T_c of 10.7 K) we found that the Li-excess in the

surface layers was significantly increased compared to the samples grown at 800 ˚C. Figure 63 shows the Ti 3s, Li 3s spectra and their corresponding total fits - normalized to the Ti 3s area peaks - collected at various emission angles of a $LiTi_2O_4$ film grown at 600 ˚C. The predominant Li 1s peak with respect to the Ti 3s peak for different collection angles can be observed. This can be seen with more clarity in Figure 64, which shows the overlapped spectra collected at different angles. In these films the Li to Ti ratio at $\theta = 0°$ was 4.2±0.2 and increased dramatically to 26.5±2.7 for θ=75°.

By modelling the data (Figure 65) using the same procedure used for films grown at 800 ˚C, we found that for low-temperature growth, the thickness of the Li-excess layer doubles to ~2.5 nm. Moreover, Ti would be absent in the top ~0.5 nm of the film. The surface composition is schematically depicted in the inset of Figure 65b.

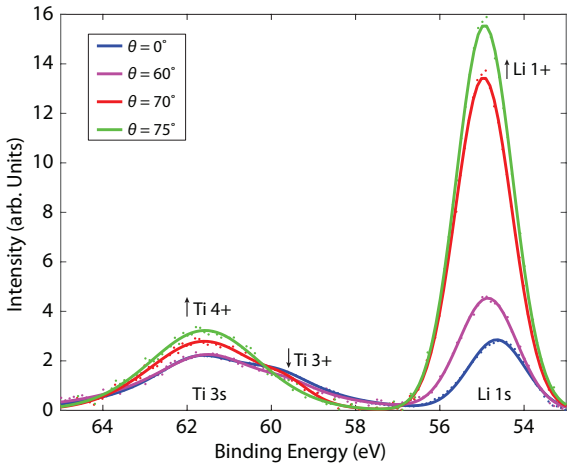

Figure 64 - Measured Li 1s and Ti 3s XPS spectra taken at different collection angles for a 200 nm-thick $LiTi_2O_4$ film grown at 600 ˚C. The arrows indicate the direction of increasing θ. The dots indicate the experimental data; the solid lines are the data envelopes fittings.

The increase in Li content at the surface for films grown at lower temperatures is counterintuitive as the out-diffusion may be expected to be reduced. However, previous studies have shown that Li can evaporate from the surface, where the evaporation rate increases with temperature [165,166]. Optimal surface layers are thus obtained when the competing processes of surface segregation and evaporation are balanced, i.e. the thickness of the Li-excess layer has to be kept minimal while keeping the out-diffusion low. Therefore, we have grown $LiTi_2O_4$ films in a temperature range of 400-800 ˚C. The found Li/Ti ratios are shown in inset of Figure 65a. These Li/Ti ratios show that up to 700 °C, the Li excess at the surface is extremely high, suggesting that the Li-evaporation is low. Increasing the growth temperature further, a clear drop in the Li/Ti ratio is present, indicating that Li evaporates from the surface. Taking also the bulk properties into account, our data suggest that a growth temperature of 800 ˚C is optimal for both high quality $LiTi_2O_4$ surfaces and bulk properties.

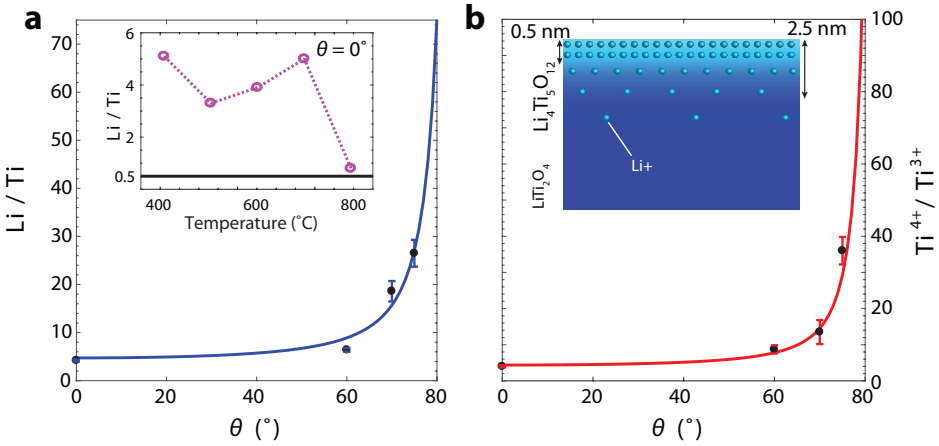

Figure 65 - Measured Li/Ti (a) and Ti^{4+}/Ti^{3+} ratios (b) for $LiTi_2O_4$ films grown at 600 ˚C(black dots) and the ratios resulting from the best-matched model (line). The inset of Figure 65a shows the Li/Ti ratio (magenta dots) for films grown at different temperatures measured at θ = 0° and the theoretical ratio value of 0.5 (black). The dotted line is a guide to the eye. A schematic model of the surface composition used to fit (solid lines) the experimental data is shown in the inset of Figure 65b.

With the presence of Li out-diffusion from bulk to the surface and subsequent Li evaporation, Li-deficiency of the bulk $LiTi_2O_4$ can be expected. However, since our films grown at 800 ˚C show a very high T_c, Li-deficiency in the bulk must be very low. Interestingly, a *small* Li deficiency could also explain our significantly higher T_c (13.8 K) compared to bulk $LiTi_2O_4$ (11.2 K), which is in agreement with the observations of Capponi *et al.* [167].

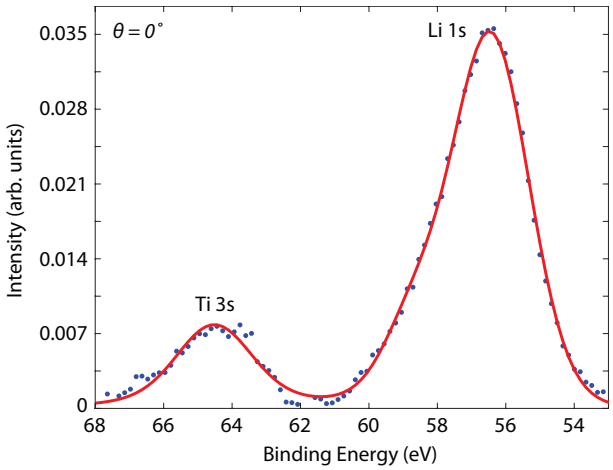

Figure 66 – Measured (dotted-blue) and total fitted (solid-red) Li 1s and Ti 3s XPS bulk-sensitive (θ = 0°) spectrum for a $LiTi_2O_4$ 200 nm-thick film capped with a 2 nm-thick $CoFe_2O_4$ layer.

In order to rule out any possible aging effect [168] arising from surface exposure to air contamination during the transfer from PLD to XPS, AR-XPS measurements were also performed on a $LiTi_2O_4$ film covered by an ultra-thin (2 nm) capping layer of $CoFe_2O_4$ deposited *in-situ* by PLD directly after the growth of $LiTi_2O_4$. The results, illustrated in Figure 66, show that the corresponding Li 1s to Ti 3s intensity ratio is very similar to that shown in Figure 64, suggesting that Li segregation is an intrinsic phenomenon occurring during growth.

In conclusion, high quality $LiTi_2O_4$ thin films were grown on $MgAl_2O_4$ substrates by PLD. The resistivity of the samples decreased with temperature, indicating a metallic behaviour. Moreover, the films undergo a superconducting transition at temperatures below T_c = 13.8 K. The growth of films at elevated temperatures in P_{O2} higher than 1x10^{-5} Torr yielded insulating films with non superconducting transition. In addition, it was shown that the growth of metal oxide $LiTi_2O_4$ thin films by PLD is affected by Li out-diffusion towards the surface. The thickness of the Li-rich layer was found to vary with growth temperature and it is minimized for samples grown at 800 ˚C, as a result of a balance between Li out-diffusion from bulk and Li evaporation from the surface.

7.2 Growth of $CoFe_2O_4$ thin films

$CoFe_2O_4$ films were grown by PLD of polycrystalline targets sintered from cobalt iron oxide nanopowders (Sigma-Aldrich). The laser was operated at an energy density of 2.5 J/cm^2 and at a repetition rate of 1 Hz. $MgAl_2O_4$(111) substrates were heated to a temperature of 800 ˚C and the P_{O_2} during growth was 30 mTorr.

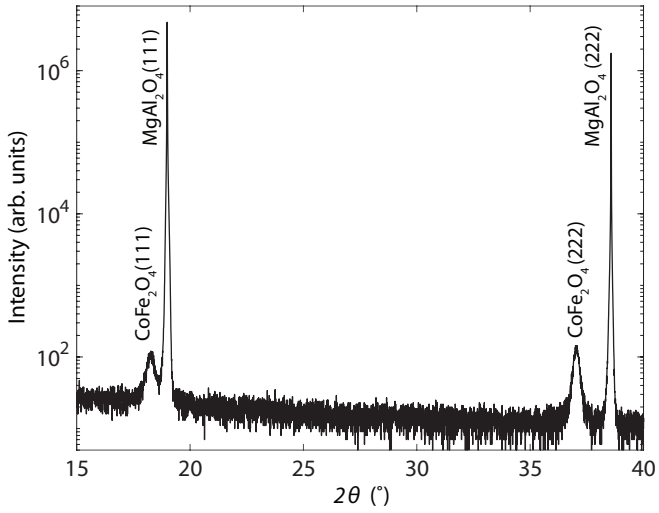

Figure 67 – XRD pattern of a 60 nm-thick $CoFe_2O_4$ film around the symmetric (111) $MgAl_2O_4$ reflection.

The XRD pattern of a 60 nm-thick $CoFe_2O_4$ thin film is depicted in Figure 67. Only the (111) family of reflections emerge from the deposited film, confirming the unidirectional growth of this ferromagnetic insulating Co-ferrite. Film thickness was determined from both fit of the periodicity of the reflectivity oscillations and simulated fit of the XRR low angle scan, Figure 68a,b. The latter provided also an estimation of the film surface roughness, which was better than ~0.5 nm. Such low roughness value was also confirmed by AFM surface analysis. Figure 68c shows the surface morphology of a $CoFe_2O_4$ thin film with smooth terraces confirming a 2-dimensional atomically flat growth of the film. The estimated RMS roughness value was 0.4 nm. This remarkably low value lends itself very well to the growth of more complex epitaxial $CoFe_2O_4$-based heterostructures, as is the intent of the research of this thesis.

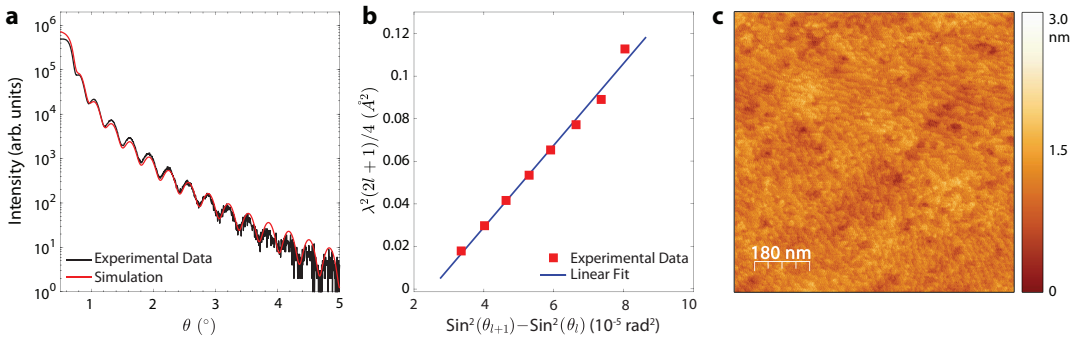

Figure 68 - (a) XRR oscillation (black) for a 34 nm-thick $CoFe_2O_4$ film grown on $MgAl_2O_4$ (111) substrate and the simulated fit (red). (b) Fit of the periodicity of the XRR reflectivity oscillations. (c) AFM image of the same $CoFe_2O_4$ film grown on $MgAl_2O_4$ substrate.

The well controlled growth of single phase $CoFe_2O_4$ with smooth surface and interface morphology was also confirmed by the XRD pattern of thin films grown on (100)-oriented MgO substrates which showed Laue oscillations, as shown in Figure 69. The latter can be related to the film thickness [169] and appear in XRD pattern of films with very low surface roughness.

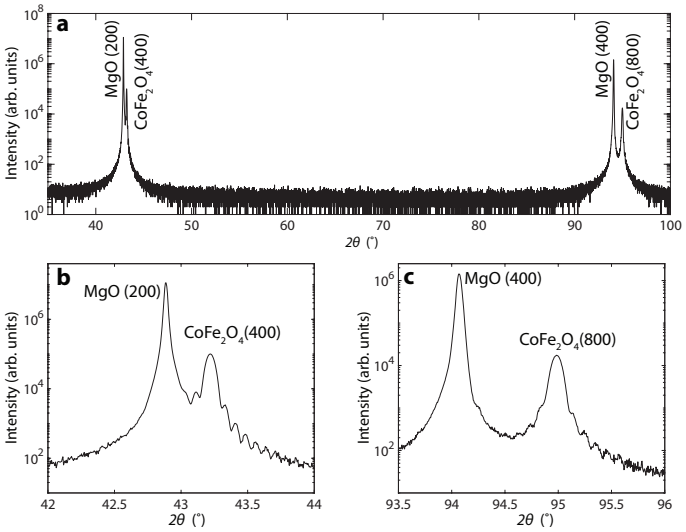

Figure 69 – (a) XRD diffraction pattern of a 75 nm-thick $CoFe_2O_4$ film grown on MgO (100) substrate. (b), (c) The peaks intensity of the film is modulated by finite thickness Laue fringes.

As they act as FI in spin-filter tunnel junctions, $CoFe_2O_4$ thin films were characterised for their in-plane electronic properties using the method described earlier in chapter 5. The resistivity versus temperature curve $\rho(T)$ for a $CoFe_2O_4$(50 nm) film grown on $MgAl_2O_4$ is shown in Figure 70. It clearly demonstrates the typical insulating behaviour with increasing resistance as the temperature is lowered. The room temperature resistivity for this sample was $\rho(290\ K) = 88\ \Omega cm$. Below ~110 K, the measured experimental resistance exceeded the measurement limit of the voltmeter.

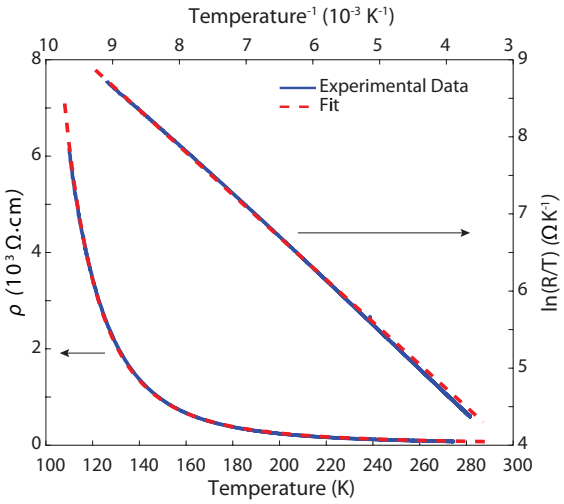

Figure 70 – Experimental (blue) temperature dependence of the in-plane resistivity of a 50 nm-thick $CoFe_2O_4$ film and the corresponding Emin-Holstein model fit (red).

The graph also shows the agreement of the data with the fit of the Emin-Holstein model [170] for small polaron hopping in the adiabatic limit

$$\rho(T) = \mathcal{K}_{EH} \cdot T \cdot e^{\frac{E_a}{k_B T}} \ , \tag{93}$$

where $\mathcal{K}_{EH}$ is a constant related to the polaron concentration and hopping length; E_a is the activation energy. Least square linear fitting of $ln(R/T)$ versus $(1/T)$ gives an E_a of 68 meV. For ultra-thin $CoFe_2O_4$ the resistivity-temperature curves are not shown, as at room temperature the resistivity was already too high to provide a measurement within the experimental setup limits.

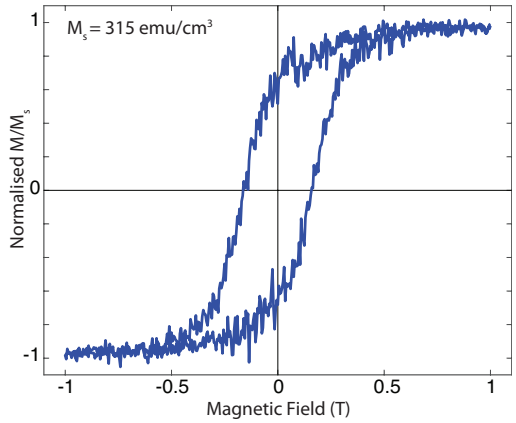

Figure 71 – Normalised in-plane magnetic hysteresis loop at room temperature of a 60 nm-thick $CoFe_2O_4$ film grown on $MgAl_2O_4$ (111). The paramagnetic contribution of the substrate has been subtracted from the measured signal and the hysteresis loop is normalised to the in-plane M_s value at 1 T.

The $CoFe_2O_4$ needs to have magnetic properties to actually act as spin-filter of charge currents, due to the lowering of the barrier below T_{Curie}. Room temperature magnetic properties of the $CoFe_2O_4$ films were investigated by means of VSM and are shown in Figure 71. The films exhibit

the characteristic magnetic hysteresis loop. The in-plane M_S at 1 T and the coercive field were 315 emu/cm^3 (or a magnetic moment of 2.5 μ_B per formula unit) and 150 mT, respectively. This magnetic value compares well with the maximum 3 μ_B theoretically obtained for bulk $CoFe_2O_4$ with an inverse spinel structure [103] and for PLD grown $CoFe_2O_4$ thin films [171,172].

In conclusion, high quality single-phase $CoFe_2O_4$ thin films were grown by PLD on single crystal substrates of $MgAl_2O_4$ cut along the (111) crystallographic orientation. The films show the insulating and ferromagnetic properties necessary to be integrated as a barrier in a spin-filter tunnel junction.

7.3 Growth of $CoFe_2O_4/LiTi_2O_4$ bilayers

Once the $LiTi_2O_4$ and $CoFe_2O_4$ single thin films growth was optimised, the research focused on the growth of these two spinel oxides in the form of heterostructures, such as $LiTi_2O_4/CoFe_2O_4/LiTi_2O_4$ (SIS) and $LaNiO_3/CoFe_2O_4/LiTi_2O_4$ (SIN) tunnel junctions. Firstly though, an optimisation of the growth of these two oxides in the form of $CoFe_2O_4/LiTi_2O_4$ bilayers was carried out. This growth optimisation process was required as the characterisation of $CoFe_2O_4/LiTi_2O_4$ bilayers deposited by simply following the same growth conditions for high quality $LiTi_2O_4$ and $CoFe_2O_4$ single thin films, described in the previous sections, showed poor conducting properties for the $LiTi_2O_4$ bottom layer. This was because the deposition of $CoFe_2O_4$ at 800 ˚C and at P_{O_2}=30 mTorr on a previously grown $LiTi_2O_4$ (P_{O_2}< 5x10^{-6} Torr and at 800 ˚C) had a deleterious effect on the latter, which did not show any metallic-superconducting properties, but instead had an insulating behaviour. The 4-wire resistance versus temperature measurement of such $CoFe_2O_4$(5 nm)/$LiTi_2O_4$(200 nm) bilayer grown on $MgAl_2O_4$ substrate, showing insulating behaviour, is depicted in Figure 72. Below ~120 K, the measured experimental resistance exceeded the measurement limit of the voltmeter.

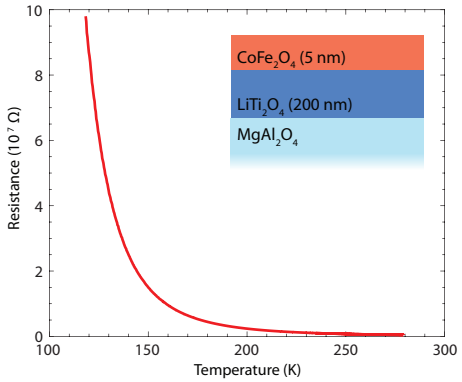

Figure 72 – Resistance versus temperature measurement of as-deposited $CoFe_2O_4$(5 nm)/$LiTi_2O_4$(200 nm) bilayer on $MgAl_2O_4$ substrate. The growth conditions of the two layers are those presented in the previous sections of this chapter for high quality metallic-superconducting single $LiTi_2O_4$ thin films (800 ˚C, P_{O2} < 1x10^{-6} Torr) and insulating ferromagnetic single $CoFe_2O_4$ (800 ˚C, P_{O2} =30 mTorr) thin films.

The detrimental effect of the growth of $CoFe_2O_4$ on top of $LiTi_2O_4$ is due to the high sensitivity of the metallic oxide to the P_{O_2} in the chamber. Conversely, oxygen deficiencies are deleterious to the magnetic properties of spinel ferrite thin films [173]. As presented in chapter 4, oxygen ions in the spinel structure produce an indirect exchange interaction between the magnetic ions, leading to a net magnetic moment in the ferrites. Thus any oxygen deficiency due to a growth at low P_{O_2}, reduces the exchange interaction between the magnetic ions, and hence, the saturation magnetisation of the $CoFe_2O_4$ films. This was confirmed by the deposition of bilayers deposited at the reduced oxygen environment (P_{O_2} ~ 10^{-6} Torr) favourable for high quality $LiTi_2O_4$ film. The results show that although Li-titanate has not lost its superconducting and metallic properties (Figure 73c), $CoFe_2O_4$ grows with more than one phase (Figure 73a) on the (111)-$MgAl_2O_4$ substrate. More importantly, the magnetic layer has a very low magnetic moment. Figure 73b shows the normalised hysteresis loop of a $CoFe_2O_4$ film grown at its optimal oxygen pressure P_{O_2}=30 mTorr compared to a $CoFe_2O_4$ thin film grown at P_{O_2}< 10^{-6} Torr. The in-plane M_s of the latter is only 9% of the first, i.e. 7.5% of the bulk value, which would be deleterious for spin-filtering.

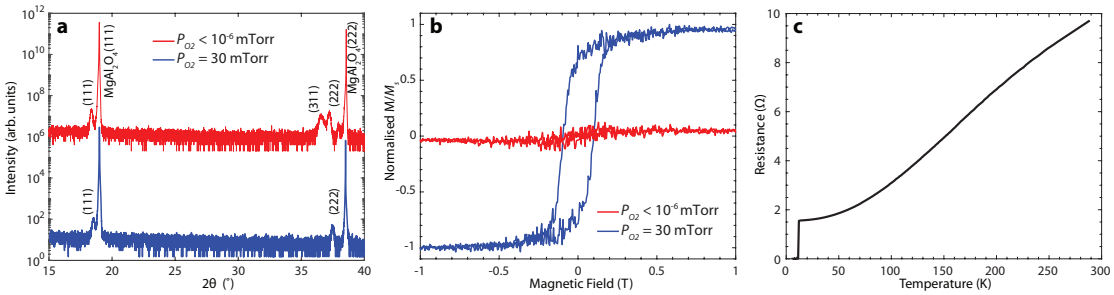

Figure 73 – Main properties of bilayer grown at P_{O2} < 10^{-6} Torr. (a) XRD pattern of a single $CoFe_2O_4$ film grown in reduced conditions showing multiphases peaks (red), compared to an XRD pattern of single $CoFe_2O_4$ grown at P_{O2}=30 mTorr showing mono (111)-orientation (blue). Curves are offset for clarity. (b) Magnetic hysteresis loop of the same $CoFe_2O_4$ layers showing poor Ms for the layer grown in reduced oxygen pressure due to oxygen deficiencies. (c) The underlying $LiTi_2O_4$ layer in a $CoFe_2O_4$/$LiTi_2O_4$ bilayer grown all in reduced oxygen conditions is still metallic and superconducting.

It was therefore clear that integrating $LiTi_2O_4$ into spinel ferrite-based spin-filter junction needed a fine tuning of the growth conditions of these two materials, requiring very different oxygen partial pressures. A few approaches were followed in order to combine $LiTi_2O_4$ and $CoFe_2O_4$ in a bilayer without detrimentally affect each other during growth: (i) For example, to compensate for the low M_s of $CoFe_2O_4$ in a bilayer grown in reduced oxygen environment, samples were annealed at different P_{O_2} and at different temperatures, in order to compensate for the oxygen deficiencies in the $CoFe_2O_4$ layer. The results are shown in Figure 74; (ii) A mixture of N_2O/O_2 instead of O_2 was used, as suggested by Hassan *et al.* [174], to reduce the chemical potential of the oxygen ions; (iii) A few capping monolayers of $CoFe_2O_4$ were grown at the same reduced P_{O_2} environment of $LiTi_2O_4$, in order to not expose the latter to oxygen during the growth of the subsequent monolayers of $CoFe_2O_4$ at higher P_{O_2}; In all cases, though an increased M_s of the $CoFe_2O_4$ layer could be observed, the underlying $LiTi_2O_4$ of the bilayers showed insulating behaviour indicating an oxidation of the Ti^{3+} ions and the formation of the unwanted insulating $Li_4Ti_5O_{12}$ phase.

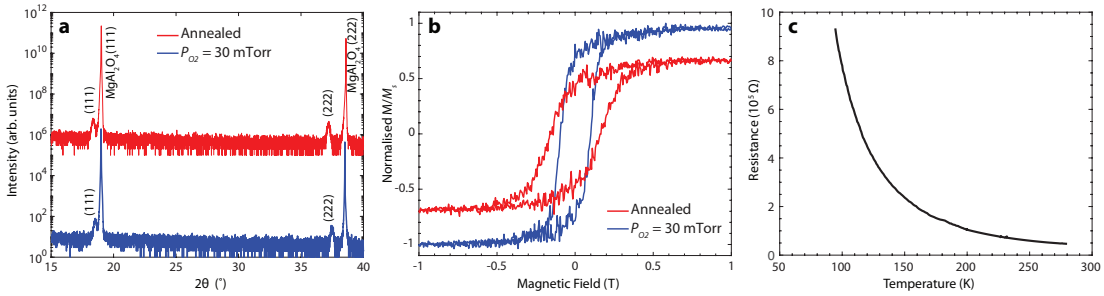

Figure 74 - Main properties of bilayer grown in reduced oxygen pressure and then annealed. (a) XRD pattern of a $CoFe_2O_4$ film grown in reduced conditions and then annealed showing single phase peaks (red), compared to an XRD pattern of $CoFe_2O_4$ grown in 30 mTorr showing single (111)-orientation (blue). Curves are offset for clarity. (b) Magnetic hysteresis loop of the same $CoFe_2O_4$ layers showing a restoration of M_s for the layer grown in reduced oxygen pressure and then annealed due to the decrease of oxygen deficiencies. (c) The underlying $LiTi_2O_4$ layer in a $CoFe_2O_4/LiTi_2O_4$ bilayer grown all in reduced oxygen conditions and then annealed is not metallic-superconducting and shows insulating behaviour.

From these attempts, it became clear that the successful growth of a $CoFe_2O_4/LiTi_2O_4$ bilayer showing metallic properties and good ferromagnetic properties would have required to compromise the saturation magnetisation of the $CoFe_2O_4$ layer by lowering P_{O_2} and the growth temperature, in order to preserve the metallic state of $LiTi_2O_4$. This was achieved by keeping the substrate temperature at 800 °C in a P_{O_2} better than $5x10^{-6}$ Torr during the growth of the $LiTi_2O_4$ layer in order to promote growth of the superconducting phase. This is also the optimal temperature to reduce Li segregation at the surface, as presented in section 7.1. Next, to avoid any unfavourable oxidation of deposited $LiTi_2O_4$ layer, during the subsequent growth of $CoFe_2O_4$, the temperature of the substrate was lowered to 450°C. Thereafter high purity oxygen was injected into the chamber and P_{O_2} was maintained at 20 mTorr, to limit formation of oxygen deficiencies in the magnetic layer. In this way, the chemical potential of oxygen ions was lower and the oxidation of Ti^{3+} into Ti^{4+} could be avoided, keeping $LiTi_2O_4$ in its metallic, superconducting phase.

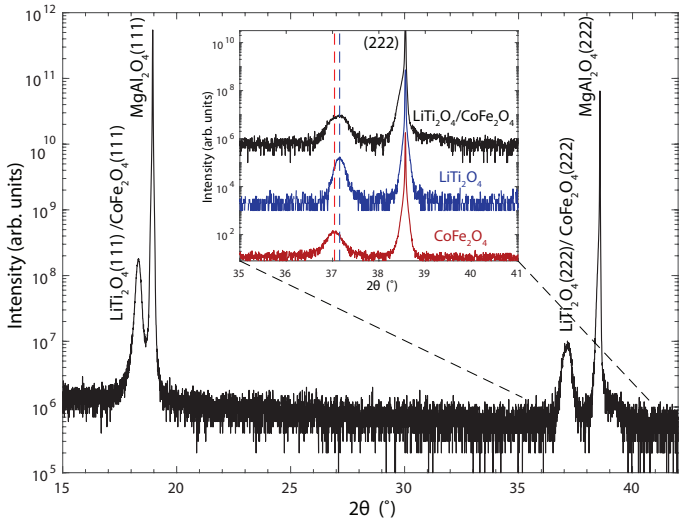

Figure 75 – XRD pattern for a $CoFe_2O_4$(60 nm)/$LiTi_2O_4$(200 nm) bilayer around the symmetric (111) $MgAl_2O_4$ reflection. Inset compares XRD pattern of the bilayer (black) with those of a 60 nm-thick $CoFe_2O_4$ (red) and 200 nm-thick $LiTi_2O_4$ (blue) single films. Curves are offset for clarity.

To verify lattice match and bulk phase purity of the deposited films, we measured out-of-plane XRD patterns for a $CoFe_2O_4$ (60 nm)/$LiTi_2O_4$ (200 nm) bilayer. The XRD pattern, shown in Figure 75, shows clear (111) and (222) Bragg's reflection peaks of the films and those of the underlying $MgAl_2O_4$ (111) substrate. No undesired phase or orientation of either $LiTi_2O_4$ or $CoFe_2O_4$ are observed in the pattern, pointing out that both layers are in single phase and highly oriented. The overlap of the two films' reflection peaks of the bilayer, due to their close lattice match, is clear in the inset of Figure 75 where the (222) reflection peak of the bilayer is compared with the reflections of a single $LiTi_2O_4$ (200 nm) film and a single $CoFe_2O_4$ (60 nm) film grown on $MgAl_2O_4$ (111).

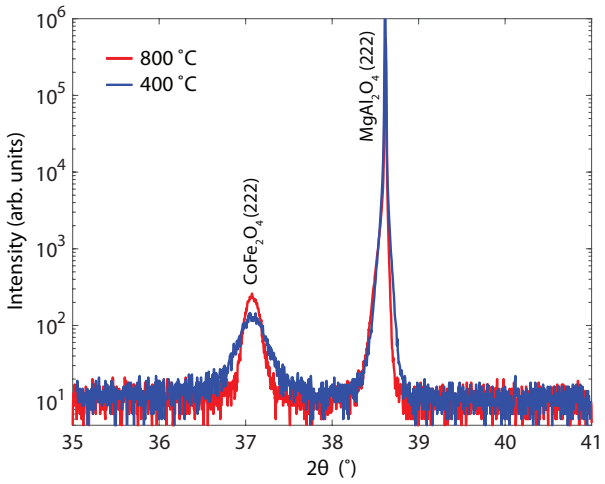

Figure 76 - XRD patterns for a 60 nm-thick $CoFe_2O_4$ grown at 800 ˚C (red) and at 450 ˚C (blue) around the symmetric (111) $MgAl_2O_4$ reflection

XRD was also used to determine the effect of the growth of $CoFe_2O_4$ at 450 ˚C instead of 800 ˚C. Figure 76 illustrates the comparison between the XRD pattern of a $CoFe_2O_4$ thin film grown at 800 ˚C and one grown at 400 ˚C and shows that the full-width at half-maximum of the (222) peak decreases with the temperature, indicating the $CoFe_2O_4$ is still single-phase while its grains grow larger.

Temperature-dependent resistivity measurement of a $CoFe_2O_4$(10 nm)/$LiTi_2O_4$(50 nm) bilayer shows metallic behaviour (Figure 77). Moreover, the bilayer undergoes a superconducting transition at $T_C = 11.5\ K$, confirming that the bottom layer has kept its metallic-superconducting phase and did not suffer any oxidation due to the growth of $CoFe_2O_4$. The T_C is in good agreement with that of single $LiTi_2O_4$ films. The width of the superconducting transition is less than 0.4 K (inset Figure 77). The Fermi liquid behaviour of the bilayer is confirmed by the variation of resistivity as T^2 at lower temperatures (blue-dashed line). The residual resistivity ρ_0 and the residual resistivity ratio $RRR = \rho_{300K}/\rho_{25K}$ of the films were $463\ \mu\Omega cm$ and 1.5, respectively, in accordance with recent

publications [121–124,160] and with single $LiTi_2O_4$ films. At temperatures below 20 K the bilayer exhibits an increase in resistance, characteristic of weak localization in disordered 2D films [175].

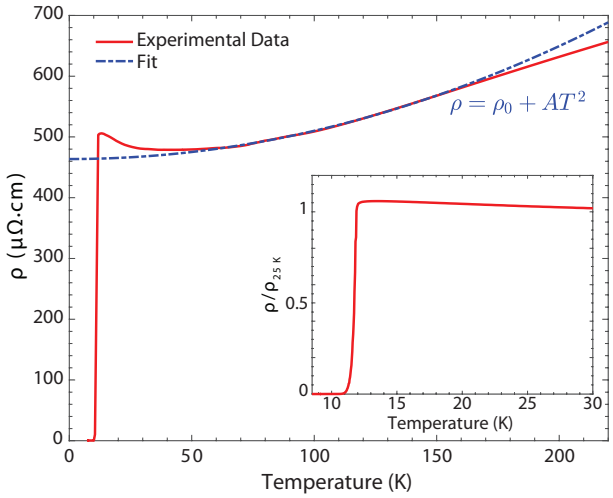

Figure 77 - Temperature dependence of resistivity for $CoFe_2O_4$(10 nm)/$LiTi_2O_4$(50 nm) bilayer. The blue-dotted line is the quadratic $\rho = \rho_0 + AT^2$ fit in the temperature range 50-150 K. The inset shows the superconducting transition at $T_c = 11.5\ K$.

The magnetic hysteresis loops measured by VSM at room temperature of a $CoFe_2O_4$(60 nm)/$LiTi_2O_4$(50 nm) bilayer grown on $MgAl_2O_4$(111) substrate are shown in Figure 78. The hysteresis loops are normalized to the in-plane magnetisation value at 1 T and the paramagnetic contribution of the substrate was subtracted from the measured signals. The magnetic layer of the $CoFe_2O_4$/$LiTi_2O_4$ shows ferromagnetic-like behaviour. The in-plane M_s at 1 T and the coercive field were 200 emu/cm^3 (or a magnetic moment of 1.6 μ_B per formula unit) and 95 mT, respectively. This magnetic moment value is lower than the maximum 3 μ_B theoretically obtained for bulk $CoFe_2O_4$ with an inverse spinel structure [103] and lower than the one obtained for single $CoFe_2O_4$ films (2.5 μ_B per formula unit).

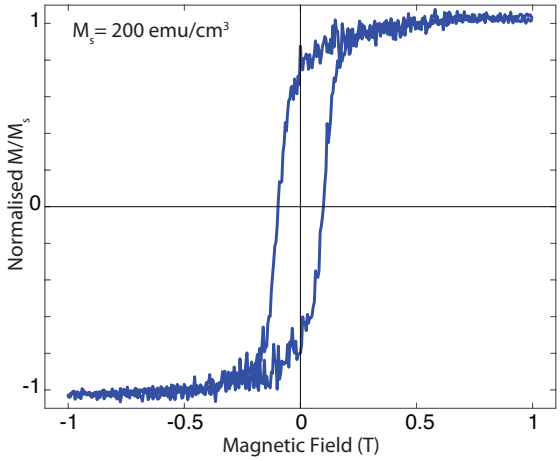

Figure 78 - Normalised in-plane magnetic hysteresis loop at room temperature of a $CoFe_2O_4$ (60 nm)/$LiTi_2O_4$ (50 nm) bilayer grown on $MgAl_2O_4$ (111). The paramagnetic contribution of the substrates has been subtracted from the measured signal and the hysteresis loop is normalised to the in-plane M_s value at 1 T.

The decreased M_s is consistent with previous reports [173] on $CoFe_2O_4$ grown at low P_{O_2} and low temperature, and was expected due to the conditions required to avoid any oxidation of the underlying $LiTi_2O_4$. Also the decreased coercive field with respect to single $CoFe_2O_4$ thin films, due to the growth at lower temperatures, is in agreement with previous findings [173]. In a spin-filter device, the tunnelling spin currents depend exponentially on the barrier height difference between the two spins, so a lower than expected exchange energy of the FI, due to the lower M_s values, can still produce a high polarisation of the current.

In conclusion, $CoFe_2O_4$ and $LiTi_2O_4$ were successfully grown on $MgAl_2O_4$ substrates in the form of bilayers, under growth conditions that did not oxidise the $LiTi_2O_4$ into its insulating phase, and that did not have a deleterious effect on the magnetic properties of $CoFe_2O_4$. This $CoFe_2O_4/LiTi_2O_4$ bilayer is the building block from which tunnel junction heterostructures can be grown.

Chapter 8. Devices experimental results

In the previous chapter the successful growth on $MgAl_2O_4$ substrates of metallic superconducting $LiTi_2O_4$ and ferromagnetic insulating $CoFe_2O_4$ in the form of bilayers has been presented. To prove that $LiTi_2O_4$ can be used as oxide electrode in a tunnel junction, a third top electrode layer is required. For this purpose, the growth of another $LiTi_2O_4$ layer on top of the $CoFe_2O_4/LiTi_2O_4$ bilayer has been explored for the fabrication of a symmetric SIS junction. Additionally, the growth of $LaNiO_3$, a paramagnetic conducting perovskite oxide, to be used as a non-magnetic metallic electrode in a SIN tunnel junction, has been explored too. In the next chapter are presented the experimental transport measurement results of $LaNiO_3/CoFe_2O_4/LiTi_2O_4$ (SIN) junctions and $LiTi_2O_4/CoFe_2O_4/LiTi_2O_4$ (SIS) junctions, microfabricated by FIB and by 3-step conventional lithography process.

8.1 $LaNiO_3/CoFe_2O_4/LiTi_2O_4$ SIN devices

The integration of a non-magnetic metallic $LaNiO_3$ electrode in $CoFe_2O_4/LiTi_2O_4$-based SIN junctions has the potential to allow TM measurements and thus to probing the superconducting DoSs of the $LiTi_2O_4$ electrode. $LaNiO_3$ has served this purpose in other oxide-based electronic devices [86,176,177] and recently also in spin-filter tunnel junctions [178,87,88]. The deposition of $LaNiO_3$ thin films exhibiting metallic conductivity requires a very high oxygen pressure P_{O_2} during growth. This is because the conductance depends on the degree of oxidation of the Ni^{3+} ions, which are thermodynamically highly unstable [176]. N_2O has been proven to be an alternative to oxygen for the correct oxidation of Ni during growth of $LaNiO_3$ thin films [179]. Thus, for the deposition of the $LaNiO_3/CoFe_2O_4/LiTi_2O_4$ tunnel junction, the growth of $LaNiO_3$ films was first optimised.

In Figure 79a the structural characterisation by XRD of a 200 nm-thick film of $LaNiO_3$ grown on (110)-oriented $SrTiO_3$ substrates at 650 ˚C at a P_{N2O} of 200 mTorr is shown. Clear single-phase reflections corresponding to those of the substrate are present, suggesting a unidirectional growth of the single phase $LaNiO_3$ film. Moreover, transport measurements on the same film reveal a $\rho(T)$ curve (Figure 79b) with a clear monotonic decrease of the resistivity with decreasing temperature, typical of a conductive behaviour. At temperatures below 80 K, ρ saturates to a constant value near 4.2 K, which is in agreement with previous findings [177,180,181]. In this range of temperatures the experimental curve finds agreement with a Fermi Liquid model fit. The residual resistivity ρ_0 and residual resistivity ratio RRR of the films were 1.8 mΩcm and 1.6, respectively. In addition, the room temperature resistivity was as low as ρ(290 K)=2.8 mΩcm confirming that $LaNiO_3$ can be used as a low-resistance contact material in tunnel junctions.

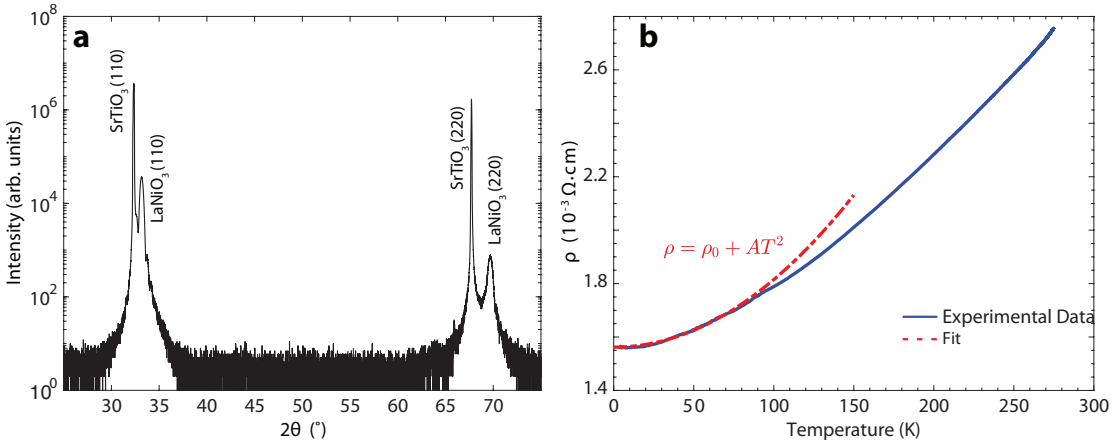

Figure 79 – (a) $LaNiO_3$ XRD diffraction pattern grown on $SrTiO_3$ (110)-oriented substrate. (b) Temperature dependence of resistivity for a 100 nm-thick $LaNiO_3$ film (red-solid line). Blue-dotted line is the $\rho = \rho_0 + AT^2$ fit in the temperature range 4-80 K.

Once the $LaNiO_3$ growth conditions were optimised a 200 nm-thick film was grown on a $CoFe_2O_4$(1-3 nm)/$LiTi_2O_4$(200 nm) bilayer and the entire heterostructure was then microfabricated into tunnel junctions by means of lithography, ion milling and FIB milling, as described in chapter 6. Figure 80a illustrates the SEM image of the central part of the sample after lithography showing the micron-scale tracks connected to the millimetre-scale contact pads. A cross sectional image of the fabricated tri-layer SIN system is shown in Figure 80b.

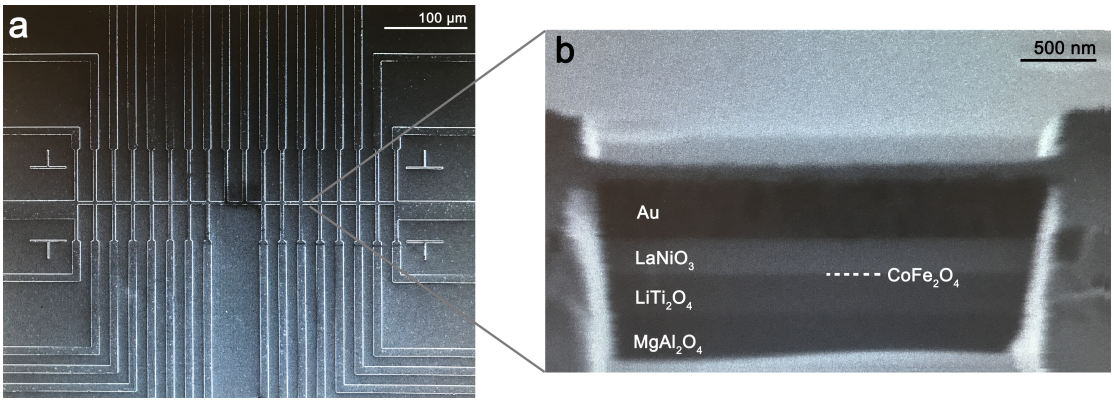

Figure 80 – (a) SEM image of the central part of the sample after lithography and ion-milling process showing the micron-scale tracks. (b) Cross-sectional SEM image of a $LaNiO_3$(200 nm)/$CoFe_2O_4$(2 nm)/$LiTi_2O_4$(200 nm) SIN heterostructure.

The measurement of any tunnelling current in the fabricated devices was unsuccessful for all the samples deposited. The measured tunnel resistance was in the range of ~10^2 MΩ. This was most likely due to $LiTi_2O_4$ readily oxidising into the insulating phase during the growth of the $LaNiO_3$ top electrode. Resistance measurement of the $LiTi_2O_4$ electrode in a $LaNiO_3$/$CoFe_2O_4$/$LiTi_2O_4$ heterostructure, by direct wire bonding through vias opened with a simple lithography and milling run, showed insulating behaviour (Figure 81). The same procedure of fine tuning the growth conditions between $LiTi_2O_4$ and $CoFe_2O_4$ followed, this time including the $LaNiO_3$ layer, in order to

determine an optimal P_{O_2} and P_{N_2O} for all the three layers. The high P_{N_2O} required to favour the metallic state of $LaNiO_3$ could not be overcome and a working SIN tunnel junction of the form $LaNiO_3/CoFe_2O_4/LiTi_2O_4$ could not be achieved.

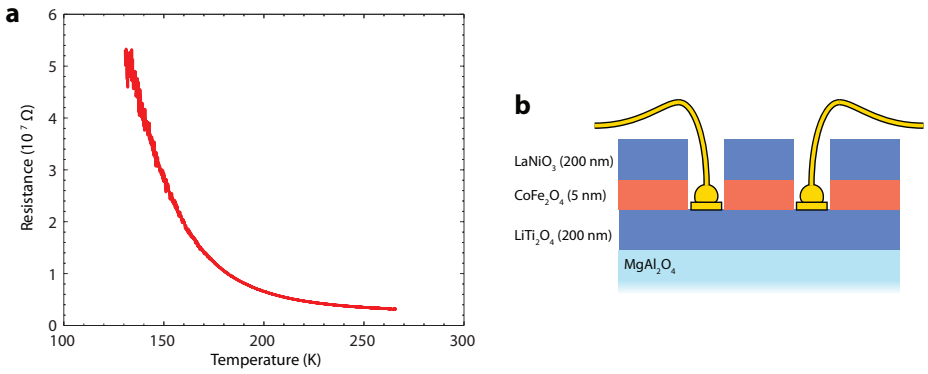

Figure 81 – (a) Resistivity versus temperature measurement of the $LiTi_2O_4$ electrode in a $LaNiO_3/CoFe_2O_4/LiTi_2O_4$ heterostructure by (b) direct wire bonding through vias opened with a simple lithography and milling run.

8.2 $LiTi_2O_4/CoFe_2O_4/LiTi_2O_4$ SIS devices

To prove the suitability of $LiTi_2O_4$ as an electrode in an almost defect-free all-spinel oxide spin-filter junction a symmetric superconducting tunnel junction of the form $LiTi_2O_4$(50 nm)/$CoFe_2O_4$(1-3 nm)/$LiTi_2O_4$(50 nm) was grown. For this purpose, a second layer of $LiTi_2O_4$ was grown on top of the $CoFe_2O_4$(1-3 nm)/$LiTi_2O_4$(50 nm) bilayers. These oxide heterostructures were then patterned into tunnel junctions.

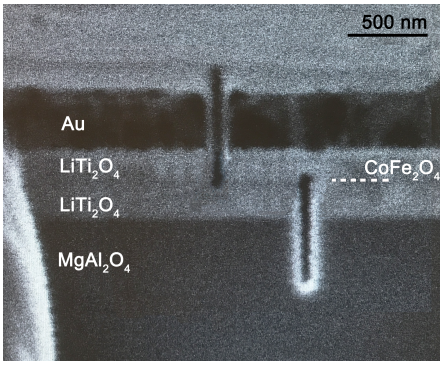

Figure 82 – Cross-sectional SEM image of a $LiTi_2O_4$(200 nm)/$CoFe_2O_4$(2 nm)/ $LiTi_2O_4$(200 nm) SIS heterostructure.

First, $LiTi_2O_4$(200 nm)/$CoFe_2O_4$(1-3 nm)/$LiTi_2O_4$(200 nm) heterostructures were grown on $MgAl_2O_4$ substrates and then microfabricated by FIB. A cross sectional SEM image of such devices is shown in Figure 82. In this case, as the two electrodes are both $LiTi_2O_4$ (i.e. the secondary electron are the same) and the $CoFe_2O_4$ is very thin, the contrast is not sufficient to reveal where to perform the isolating cuts in the heterostructures in order to obtain vertical transport. Though the issue can be overcome by oversizing the cuts, if the electrode thicknesses are well know, the processing of

these junction was difficult. Consequently, the yield of functional devices was very low. In addition, the devices fabricated with success showed very high R_j~10^2 MΩ. This may have been due to the known disadvantages of FIB patterning of potentially Ga ion [182] and of resputtering, which may detrimentally effect the sensitive metallic phase of $LiTi_2O_4$.

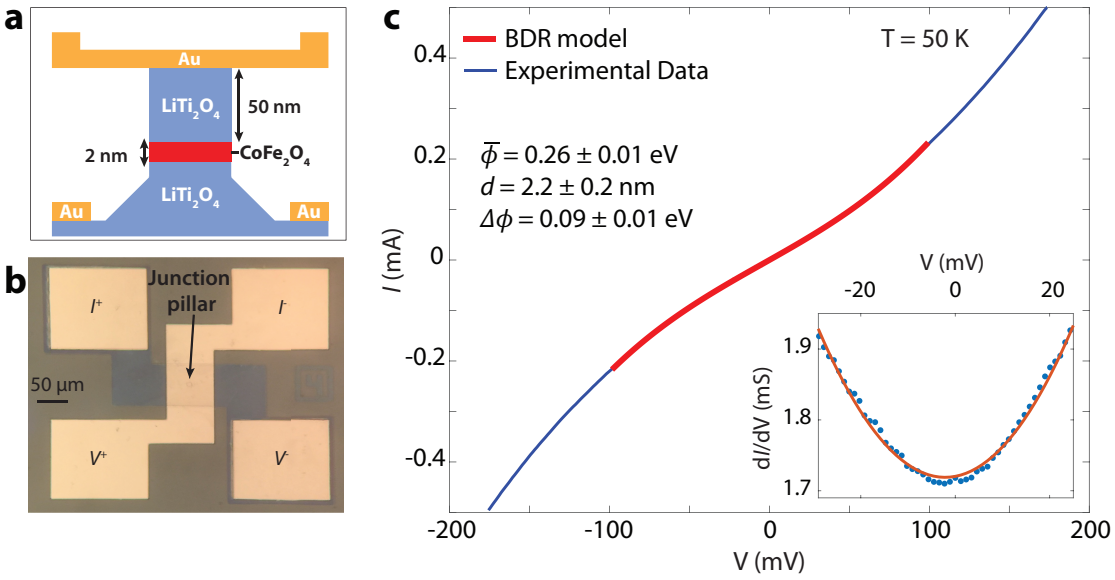

Figure 83 –(a) Schematic cross section of the side view of the micro-tunnel junction with bottom and top electrode. (b) Optical microscope image of a microfabricated tunnel junction device. (c) Current versus voltage (blue circles) of a $LiTi_2O_4$ (50 nm)/$CoFe_2O_4$(2 nm)/$LiTi_2O_4$(50 nm) junction measured at 50 K. The size of the junction is 3x3 µm^2. The inset shows the schematic cross section of the side view of the micro-tunnel junction with bottom and top electrode. The solid red-line is the Simmons fitting. The inset shows the parabolic shape (solid red-line) of the dI/dV curve (blue dots) indicating a tunnelling behaviour of the junction.

To increase the yield of functional devices and avoid any damaging effect of the $LiTi_2O_4$ electrodes, the grown symmetric superconducting heterostructure of the form $LiTi_2O_4$(50 nm)/$CoFe_2O_4$(1-3 nm)/$LiTi_2O_4$(50 nm) was patterned into tunnel junctions by means of conventional 3-step optical lithography process, described in chapter 6. The patterned micro-pillars (Figure 83a,b) fabricated with this method showed low R_j~kΩ. Moreover, the $I(V)$ curve of a $LiTi_2O_4$(50 nm)/$CoFe_2O_4$(2 nm)/$LiTi_2O_4$(50 nm) tunnel junction measured at temperatures above T_c (Figure 83c) showed strong non-linear shape, suggesting electron tunnelling across the barrier. The nearly parabolic shape of the dynamic conductance curve (Figure 83c, inset) confirms that electron transport through tunnelling across the junction is the dominant transport mode. The offset of the parabola suggests a barrier asymmetry. From fitting the measured tunnelling data after BDR model (see chapter 2), which includes the term corresponding to the barrier asymmetry, an average barrier height of 0.26±0.01 eV was obtained. The latter is lower than the theoretical band gap (0.80 eV) for $CoFe_2O_4$ but is in agreement with previous tunnelling studies on $CoFe_2O_4$. The barrier asymmetry was estimated to be 0.09±0.01 eV and is an indication that the two $LiTi_2O_4$ might have slightly different stoichiometries. The fitted barrier thickness of the $CoFe_2O_4$ layer and effective tunnelling area agreed well with the estimates. In detail, the estimated barrier thickness (2.2±0.2 nm) is within

a reasonable range of nominal thickness of the barrier layer taking into consideration ~1 nm roughness of the electrode, showing the uniform coverage of the barrier.

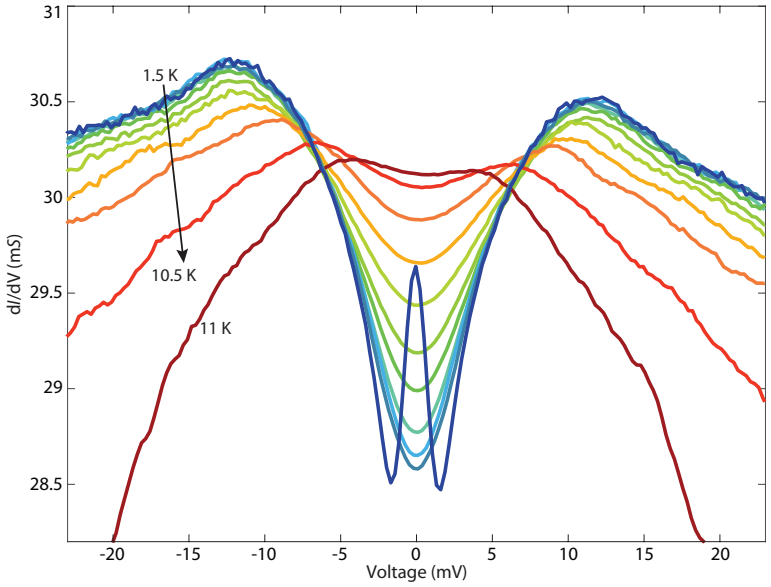

Figure 84 - Differential conductance dI/dV versus bias voltage from 1.5 to 10.5 K with 1 K increments and at 11 K in zero field for a $LiTi_2O_4$ (50 nm)/$CoFe_2O_4$(1.5 nm)/$LiTi_2O_4$(50 nm) junction. The size of the junction is 3x3 μm^2.

The dynamic conductance of a representative sample measured at low temperature is depicted in Figure 84: the $\mathrm{dI/dV}$ spectrum exhibits a characteristic superconducting energy gap structure with a dip around the zero bias and strongly smeared coherence peaks. At temperatures approaching the T_c of $LiTi_2O_4$, the gap decreases until it disappears for higher temperatures. The decrease of the conductance observed at voltages above 2Δ is most likely due to flux flow and heating in the electrodes at high current densities ~15 kA/cm^{-2}. Similar behaviours are common in tunnel junctions based on high T_C superconductors [183]. The broadening of the coherence peaks is an evidence for the smearing of the interfacial density of states due to the proximity effect of a ferromagnetic Mott insulator, which shortens the quasiparticle lifetime [59,184,185]. Another contributing factor to the smearing of the $\mathrm{dI/dV}$ curves could be the possible stoichiometric inhomogeneity between two $LiTi_2O_4$ electrodes as a consequence of their different growth conditions. The form of the $\mathrm{dI/dV}$ spectra implies that at least one of the $LiTi_2O_4$ electrodes preserves a superconducting density of states at the $CoFe_2O_4$ interface. We will begin by assuming that both electrodes are superconducting and then justify this in the light of the available information.

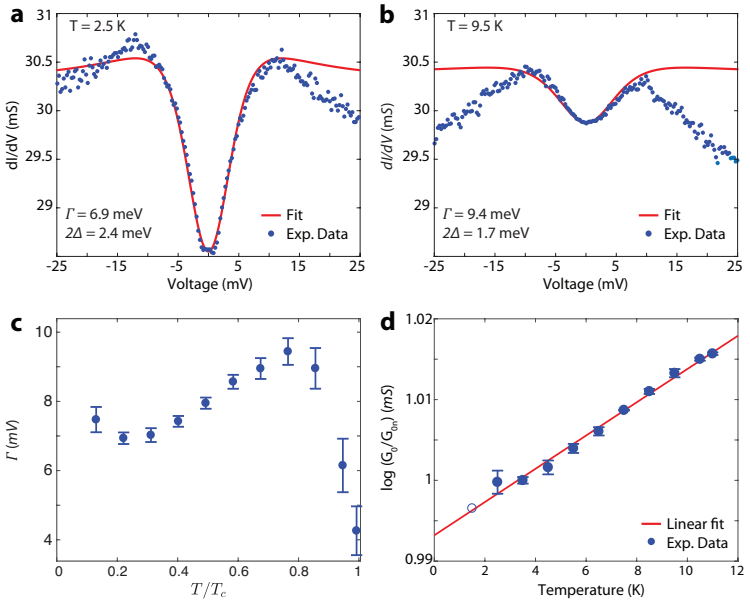

Figure 85 – (a) Temperature dependence of the zero bias conductance G_0 normalised to the value at 2.5 K (G_{0n}), except for the curve showing superconducting peak. The open circle is the normalised G_0 for the curve at 1.5 K evaluated without the superconducting peak. The smeared BCS s-wave model fit to the dI/dV versus bias voltage characteristic (a) at 2.5 K. (with $2\Delta = 2.4$ meV and $\Gamma = 6.9$ meV) and (b) at 9.5 K (with $2\Delta = 1.7$ meV and $\Gamma = 9.4$ meV) (d) Normalised temperature evolution of the Dynes fitting parameter Γ. The error bars represent the s.e. in the fit to the $\partial I/\partial V$ data.

The experimental $\mathrm{dI/dV}$ curves were fitted using a modified version of Equation (51) with a complex energy $E' = E + i\Gamma$, that takes into account sample inhomogeneity and a finite quasi-particle lifetime by scattering. According to this simplified smeared BCS model for SIN junctions, in the limit of low bias voltages and for low temperatures and by adding the phenomenological Dynes parameter Γ [59,184], the dynamic conductance can be rewritten as:

$$\frac{dI}{dV} \propto \mathrm{Re}\left[\frac{(|E - eV| - i\Gamma)}{((E - eV)^2 - \Delta^2)^{1/2}}\right]. \tag{94}$$

With these assumptions, and for large values of Γ in both electrodes, this model can also model SIS quasiparticle conductance spectra if Δ is replaced by 2Δ. In Figure 85a and Figure 85b are shown the fit to $\mathrm{dI/dV}$ curves collected at 2.5 K, with 2Δ=2.47 meV and Γ=6.9 meV, and at 9.5 K, with 2Δ=1.7 meV and Γ =9.4 meV. The peak height and the gap structure of the raw data are quite accurately reproduced by the fit. The fitting values of Γ are depicited in Figure 85c and show a clear increase with increasing temperature for temperatures below 8.5 K, i.e. $T/T_C = 0.8$. For higher temperatures a change in behaviour and an increase in the uncertainty on the estimation of the Γ parameters can be observed. This may be related to the enhancement of the quasiparticle scattering by fluctuations near the critical temperature and to the expected decrease of the goodness of the fit at higher temperatures. The zero bias conductance G_0, estimated from the $\mathrm{dI/dV}$ fits, exponentially decreases at low temperatures, as expected for an intrinsic s-wave SIS junction [186] (Figure 85d).

The superconducting energy gap width 2Δ(T) was also determined from this data. The dependence of 2Δ on the temperature (shown in Figure 86) fits well with the BCS-type temperature dependence [39]

$$2\Delta(T) = 2\Delta_0 tanh(1.74\sqrt{\frac{(T_c - T)}{T}}\ , \tag{95}$$

confirming a superconducting behaviour. The fitting parameters are $2\Delta_0$ = (2.6±0.1) meV, which is lower than the one reported in previous findings [118,124,187], and T_C = (11.0±0.3) K, in accordance with the value measured in our bilayers. Consequently, we find a $2\Delta_0/K_bT_c$ ratio of 2.8±0.2, which is less than the typical values ranging between 3 and 4.5 for BCS like superconductors but in agreement with recent scanning tunnelling spectroscopy on $LiTi_2O_4$ films [125] suggesting a modified superconductivity on the surface due to a non-stoichiometric surface layer. Another contributing factor to the reduced gap value is the suppression of the order parameter in the $LiTi_2O_4$ electrodes due to the proximity with the $CoFe_2O_4$ magnetic barrier; this is also presumably responsible for the large value of Γ. If we assumed SIN behaviour, our estimate for 2Δ would be doubled to 5 meV which is significantly larger than reported previously and so appears unreasonable.

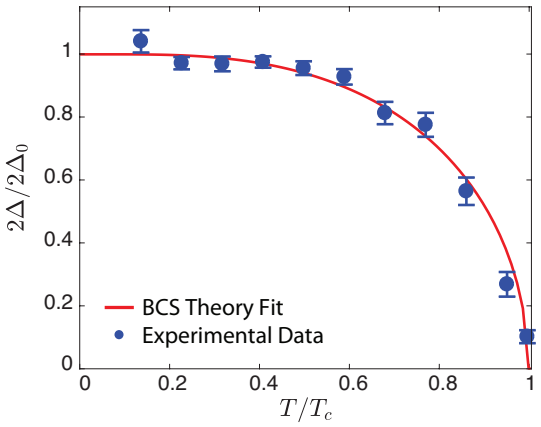

Figure 86 - Temperature dependence of normalised energy gap 2Δ and BCS fit. The error bars represent the s.e. in the fit to the dI/dV data.

SIS junctions would normally be expected to show a Josephson supercurrent with a maximum value of $\pi\Delta/(2R_j)$ where R_j is the junction normal state resistance, but for strongly spin-filtering barriers, this is expected to be substantially reduced because the tunnelling of conventional singlet Cooper pairs is blocked [188]. At the lowest temperatures a zero bias peak (ZBP) appears in low-resistance junctions ($R_j \sim 0.05\ k\Omega$) while in medium-resistance junctions ($R_j \sim 0.9\ k\Omega$) this feature is not observed – as might be expected given the experimental noise. Although this feature might be related to the flow of a Josephson supercurrent in the junction, its

disappearance at temperatures well below T_C is inconsistent with standard behaviour. Similarly, the dependence of the ZBP on an in-plane external applied field (shown in Figure 87) does not show any characteristic Fraunhofer-like modulation. In particular, the observed behaviour is not suppressed with periodic zeros at field values that introduce a flux quantum into the junction region, which in our wide (L = 3 μm) squared junctions should be multiple values of $\frac{\phi_0}{(2\lambda_{LTO}+t)L} \approx 2$ mT. The ZBP is eventually suppressed at very high external applied fields (7.5 T), which would imply an effective junction lateral size of 0.8 nm. As the latter value is unrealistic, the lack of spatial uniformity of the critical current is unknown.

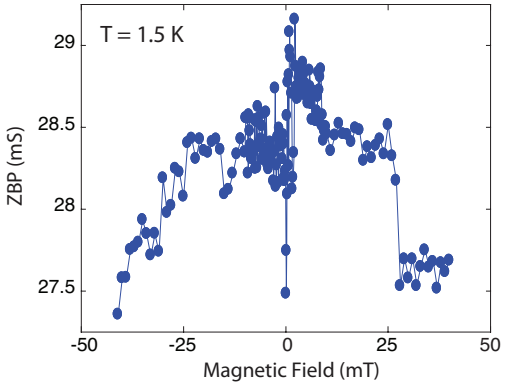

Figure 87 - Field dependence of the zero bias peak appearing at T = 1.5 K.

The dI/dV curves collected at higher biases (Figure 88) reveal an interesting midpoint state between the low bias SIS-state (i.e. both electrodes are superconducting) and the state in which the electrodes are metallic (normal state) at high bias. This conductance midpoint state is related to bias voltages at which one of the $LiTi_2O_4$ electrodes is superconducting while the other is metallic. The midpoint state, identified by the dashed arrow in Figure 88, indicates that the electrodes are in different superconducting states. For high biases the two electrodes are in their normal state and the conductance of the junction is equal to that measured at temperatures above T_C(12 K). At higher temperatures, lower biases are needed to turn the electrodes from the superconducting state to the metallic-normal state. This confirms the SIS-nature of the junctions, while the presence of two distinct conductance-states is another validation of a stoichiometric inhomogeneity between two superconducting $LiTi_2O_4$ electrodes.

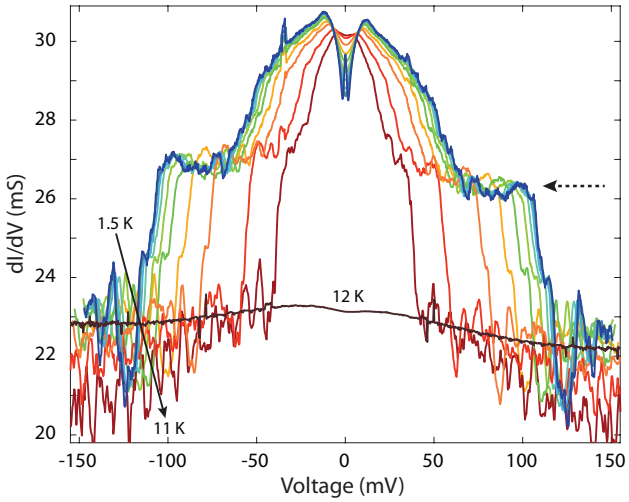

Figure 88 – Differential conductance dI/dV versus bias voltage from 1.5 to 10.5 K with 1 K increments and at 11 K and 12 K in zero field for a $LiTi_2O_4$(50 nm)/$CoFe_2O_4$(1.5 nm)/$LiTi_2O_4$(50 nm) junction collected at higher bias voltages. The dashed arrow identifies the midpoint states.

dI/dV spectra collected at 1.5 K at different out-of-plane applied magnetic fields are shown in Figure 89. The closing of the peak position along with the closing of the gap and the suppression of the superconducting peak for values approaching the $LiTi_2O_4$ upper critical field H_{c2}, are clearly visible. The scaling law follows a field quadratic-dependence $\Delta(B,T) \sim \Delta 0 - [H/H_{c2}(T)]^2$, as recently reported in point contact spectra [124]. The fit, shown in the inset of Figure 89, gives an extracted value of H_{c2} at 2 K of ~10.8 T, which is consistent with previous results [118,187].

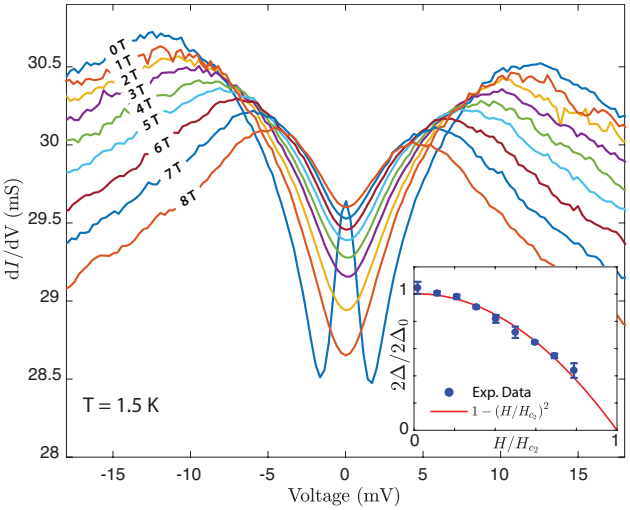

Figure 89 - Differential conductance dI/dV versus bias voltage at 1.5 K from 0 T to 8 T with 1 T increments for a $LiTi_2O_4$(50 nm)/$CoFe_2O_4$(1.5 nm)/$LiTi_2O_4$(50 nm) junction. Inset, Normalised energy gap $2\Delta/2\Delta_0$, at 1.5 K, decreasing as $1 - [H/H_{c2}(T)]^2$. The error bars represent the s.e. in the fit to the $\partial I/\partial V$ data.

Figure 90 shows the temperature dependence of a typical $LiTi_2O_4$/$CoFe_2O_4$/$LiTi_2O_4$ junction resistance with 1.5 nm $CoFe_2O_4$ barrier measured by applying a 0.1 mA current. A sharp drop on in resistance is seen at the $LiTi_2O_4$ superconducting transition due to the disappearance of the in-series resistance of the leads. At higher temperatures the resistance is not exponentially increasing with decreasing temperature, which is the behaviour for a semiconducting non-magnetic barrier [189],

but is instead continuously dropping with temperature. The temperature dependence of the resistance of the $LiTi_2O_4$ bottom lead of the same junction was measured (inset b, Figure 89) to verify that the decreasing behaviour of R_j is attributable to tunnelling current flowing across the tunnel junction and not across any series resistances, which would explain the decreasing behaviour. This is confirmed by difference in the order of magnitude between the resistance of junction $\sim 10^1\ \Omega$ and the resistance of the bottom-lead $\sim 10^2\ \Omega$. In addition, large contributions of non-tunnelling (leakage) conductance to the dominant tunnel conductance due to shorts between the two electrodes can be also ruled out since R_j is non-zero for temperature below T_C, as opposed to the two $LiTi_2O_4$ superconducting electrodes which show zero resistance.

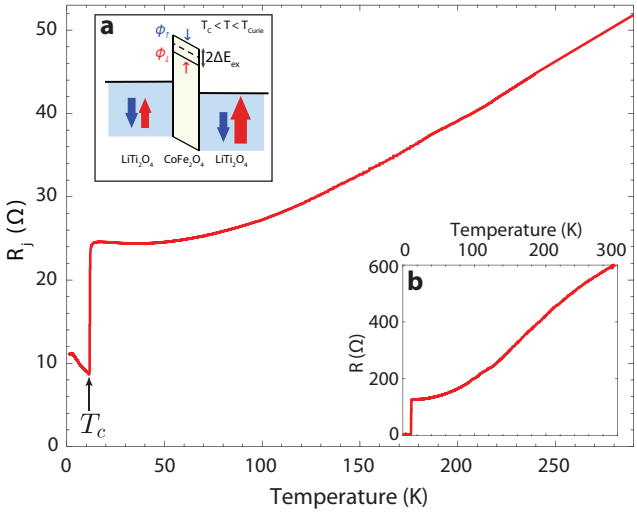

Figure 90 – Junction resistance versus temperature dependence of a $LiTi_2O_4$(50 nm)/$CoFe_2O_4$(1.5 nm)/$LiTi_2O_4$(50 nm) junction measured at a constant dc bias of 0.1 mA in a 2-wire configuration. Inset a, band diagram for a spin-filter device. Inset b, resistance versus temperature of the bottom $LiTi_2O_4$-lead of the same junction and measured in the same 2-wire configuration.

Moreover, the resistance increases with decreasing temperature below T_C, due to the fact that there are no available states for tunnelling at the Fermi energy level for measurements voltages much less than Δ. In this case the conductance is dominated by thermal excitation of quasi-particles across the gap and, as temperature decreases, the number of thermally excited quasi-particle states decreases exponentially, resulting in an increases of the sub-gap resistance for decreasing temperature. These behaviours confirm that the mechanism of charge transport in the junctions is predominantly tunnelling in nature and thus, the drop in $R_j$with decreasing temperature observed across the entire temperature range above T_C may be a consequence of the exchange splitting of the magnetic tunnel barrier, leading to a temperature dependent reduction the barrier height of one spin (inset, Figure 90). The T_{Curie} of $CoFe_2O_4$-barrier is assumed to be above room temperature, so the absence of the typical change from semiconducting behaviour to metallic-like behaviour at T_{Curie}, due to onset of spin-filtering, reported in spin-filtering devices of this type [87,190] is expected in our range of measurement.

In conclusion, the successful superconducting tunnel process in an all-spinel SIS tunnel junctions with $CoFe_2O_4$ as FI barrier and $LiTi_2O_4$ as electrodes grown on $MgAl_2O_4$ substrates was demonstrated. An estimation of the polarisation of the current could not be performed by extrapolating the temperature dependence of R_j from the high temperature ($> T_{\text{Curie}}$) regime as T_{Curie} in this case was well above room temperature.

Chapter 9. Conclusion and Future Work

In this thesis, all-spinel oxide tunnel junctions have been studied comprehensively. In particular, the capability of the metallic and superconducting $LiTi_2O_4$ spinel oxide to be integrated as electrode in ferrite-based tunnel junctions for spin-filtering applications has been demonstrated. $LiTi_2O_4$ is a promising alternative to address the problems affecting the commonly used thin film materials for top and/or bottom electrodes in spin-filtering devices, such as metals (Au, Pt, etc.) and metallic oxides ($LaNiO_3$, $La_{2/3}Sr_{1/3}MnO_3$, etc.). These films are not considered as good electrode materials for ferrite-based devices mainly because of the deterioration of the magnetic properties of oxide films by APBs introduced at the interface due to structural mismatch. $LiTi_2O_4$ has the capability of addressing these issues as it has a better structural and chemical compatibility with the functional ferrite oxide layer.

Prior to the fabrication of spinel spin-filter devices, the barrier and the electrode materials have been extensively characterised with respect to their structural, surface, magnetic and transport properties by a number of ex-situ techniques. In particular AR-XPS measurements on high quality $LiTi_2O_4$ thin films have shown that the growth of metal oxide $LiTi_2O_4$ thin films by PLD is affected by Li out-diffusion towards the surface. The thickness of the Li-rich layer was found to vary with growth temperature and it is minimized for samples grown at 800 ˚C, as a result of a balance between Li out-diffusion from bulk and Li evaporation from the surface. In addition, the challenging deposition of $CoFe_2O_4/LiTi_2O_4$ bilayers due to their different growth conditions has been addressed. The successful growth of $CoFe_2O_4/LiTi_2O_4$ bilayers in which $LiTi_2O_4$ maintains its metallic and superconducting properties, while $CoFe_2O_4$ its insulating ferromagnetic characteristics, proved that, even though the $LiTi_2O_4$ has a pronounced instability when exposed to high P_{O_2} environments during growth, it can be integrated into all-spinel structure spin-filter devices as an isostructural low-resistance contact material to most spinel oxide layers. This was also confirmed by the observation of tunnelling process in all-spinel symmetric SIS tunnel junctions with $CoFe_2O_4$ as FI barrier and $LiTi_2O_4$ as electrodes grown on $MgAl_2O_4$ substrates. The appearance in the measured current–voltage characteristics of the characteristic superconducting energy gap structure with a dip around the zero bias, and strongly smeared coherence peaks, are evidences of the tunnel nature of these junctions.

Having proven that $LiTi_2O_4$ is indeed a functioning oxide electrode, the next natural step would be to investigate the spin-filter efficiency of a spin-filter tunnel junction based on $LiTi_2O_4$. In fact, although the $CoFe_2O_4/LiTi_2O_4$ bilayer holds the potential for all-oxide magnetic tunnel junctions with efficient spin-filtering properties at room temperature, an estimation of the polarisation of the current could not be performed in this research. In particular, the SIS tunnel junctions didn't provide information on the spin-filtering efficiency of the $CoFe_2O_4/LiTi_2O_4$ bilayer due to the lack of data collected at temperatures above T_{Curie}. The spin-filtering efficiency could have been estimated by extrapolating the conductance G^* in the absence of exchange splitting

from the temperature dependence of R_j in high temperature ($> T_{Curie}$) regime measurements, as shown in chapter 3. Future work could therefore involve magnetic characterisation of $CoFe_2O_4/LiTi_2O_4$ bilayers in terms of magnetisation versus temperature in a VSM equipped with a sample heater to explore the magnetic properties of the bilayers up to 1000 K. This would allow estimating the effective T_{Curie} of the $CoFe_2O_4$ layer, which may be lower than bulk value. Consequently, transport measurements of the $LiTi_2O_4/CoFe_2O_4/LiTi_2O_4$ junctions in a physical property measurement system, capable of measurements in temperature ranges (1.9–400 K) higher than those of the CFS used in this research, could provide useful insights into the evaluation of the spin-filter efficiency.

A more ambitious path to investigate the spin-polarisation at room temperature of the $LiTi_2O_4/CoFe_2O_4/LiTi_2O_4$ would be by TMR-like experiments. These could be performed by replacing the top $LiTi_2O_4$ electrode with a spinel ferromagnet (Fe_3O_4) decoupled from the $CoFe_2O_4$ by a thin insulating layer of $MgAl_2O_4$, as suggested by promising tunnelling spectroscopy study on junctions with Au electrode [13]. The perfect epitaxy and lattice match between all the layers of such $Fe_3O_4/MgAl_2O_4/CoFe_2O_4/LiTi_2O_4$ devices grown on $MgAl_2O_4$ substrates could provide a direct measurement of the spin-filter efficiency of the isostructural $CoFe_2O_4/LiTi_2O_4$ bilayer. However, considering its proneness to oxidise, a fine control of the $LiTi_2O_4$ properties during the growth of the other oxide materials would be necessary.

The results presented throughout this thesis are merely a first crucial step towards the integration of high efficiency spin-filters into future spintronics devices. In fact, having demonstrated that $LiTi_2O_4$ can be used as an oxide electrode, one may now start thinking about the numerous more complex devices and applications that take advantage of its structural and chemical matching with the spinel ferrites, and how to integrate novel materials into these systems by also considering the careful control of cation diffusion of Li to preserve the metallic $LiTi_2O_4$ phase. The most promising future application of high efficiency spin-filter barrier at room temperature is the injection of spin-polarised currents into semiconductor materials. Although, the spin-degree of freedom of electrons has been exploited in many spintronics applications, the efficient injection of spin into semiconductors is still challenging. Combining the electronic readout capability of semiconductor devices with the magnetic storage of information by injecting and detecting spin-polarised currents is one of the prime objectives in the field of spintronics. Conventionally, the injection of spin into semiconductors is demonstrated by using ferromagnetic metals [191,192]. However, the spin injection efficiency in these systems is significantly low (<1%) and is mainly due to the large impedance mismatch between the semiconductors and the ferromagnetic metallic electrode [193,194]. Moreover the electrons passing through the metal-semiconductor interface are subject to various inelastic scatterings processes (magnons, phonons, crystal defects, etc.) due to the different electronic structure of the metal and the semiconductor, and thereby the spin injection efficiency. In order to address these problems, the insertion of a tunnel barrier between these two layers has been proposed. In fact, by inserting a FI barrier between a normal metallic electrode and a semiconductor, one can exploit the spin-filtering nature of the FI, and thus enhance

the spin injection dramatically [195]. $LiTi_2O_4$-based spin-filters could be thus integrated in room temperature semiconductor spintronics as the source and detector of spin-polarised currents [195,196] to achieve the spin-FET proposed by Datta *et al.* [197] in classic semiconductors, such as Si or GaAs. Also, organic semiconductors such as rubrene, sexithiophene or Alq_3 are of interest in this research field due to their low spin–orbit coupling guaranteeing a spin coherence higher than in inorganic semiconductors [198,199], which makes promising the injection and detection of spins in these materials [200–203].

Tunnel junctions consisting of two magnetic tunnel barriers, normal metal/Fl_1/Fl_2/normal metal, also called double spin-filters, are another interesting application of highly efficient room temperature spin-filters. In these junctions, due to the exponential dependence of the tunnelling current on the barrier height, very high MR should be observed when the two spin-filter layers are switched from the P to the AP alignment. In fact, large MR (10^5 %) has been predicted in double SF tunnel junctions [204–206]. Despite some experimental difficulties, Miao et al. [207] confirmed this concept in Al/EuS/Al_2O_3/EuS/Al MTJs with a TMR ratio of 50% at low temperatures and a bias voltage dependence confirming the spin-filtering effect. Given these promising results, it would be stimulating to study the potential of ferrites at room temperature in double spin-filter with $LiTi_2O_4$ electrodes that could avoid any MR reduction due to non-perfect interfaces.

Bibliography

[1] I. Žutić, J. Fabian, and S. Das Sarma, Rev. Mod. Phys. **76**, 323 (2004).

[2] M. Baibich, J. Broto, A. Fert, and F. Van Dau, Phys. Rev. Lett. **61**, 2472 (1988).

[3] G. Binasch and P. Grünberg, Phys. Rev. B **39**, 4828 (1989).

[4] P. Tedrow and R. Meservey, Phys. Rev. Lett. **44**, 8 (1971).

[5] P. Tedrow and R. Meservey, Phys. Rev. B **7**, 318 (1973).

[6] M. Julliere, Phys. Lett. A **54**, 225 (1975).

[7] J. S. Moodera, L. R. Kinder, T. M. Wong, and R. Meservey, Phys. Rev. Lett. **74**, 3273 (1995).

[8] J. Hayakawa, S. Ikeda, Y. M. Lee, F. Matsukura, and H. Ohno, Appl. Phys. Lett. **89**, 232510 (2006).

[9] S. A. Wolf, Science (80-.). **294**, 1488 (2001).

[10] J. S. Moodera, T. S. Santos, and T. Nagahama, J. Phys. Condens. Matter **19**, 165202 (2007).

[11] G. Schmidt and L. W. Molenkamp, Semicond. Sci. Technol. **17**, 310 (2002).

[12] J.-B. Moussy, J. Phys. D. Appl. Phys. **46**, 143001 (2013).

[13] M. Chapline and S. Wang, Phys. Rev. B **74**, 14418 (2006).

[14] U. Lüders, A. Barthélémy, M. Bibes, K. Bouzehouane, S. Fusil, E. Jacquet, J.-P. Contour, J.-F. Bobo, J. Fontcuberta, and A. Fert, Adv. Mater. **18**, 1733 (2006).

[15] S. Matzen, J.-B. Moussy, G. X. Miao, and J. S. Moodera, Phys. Rev. B **87**, 184422 (2013).

[16] A. V. Ramos, M.-J. Guittet, J.-B. Moussy, R. Mattana, C. Deranlot, F. Petroff, and C. Gatel, Appl. Phys. Lett. **91**, 122107 (2007).

[17] S. Matzen, J.-B. Moussy, R. Mattana, K. Bouzehouane, C. Deranlot, and F. Petroff, Appl. Phys. Lett. **101**, 42409 (2012).

[18] R. Datta, B. Loukya, N. Li, and a. Gupta, J. Cryst. Growth **345**, 44 (2012).

[19] J. X. Ma, D. Mazumdar, G. Kim, H. Sato, N. Z. Bao, and A. Gupta, J. Appl. Phys. **108**, 63917 (2010).

[20] D. Margulies, F. Parker, and M. Rudee, Phys. Rev. Lett. **953**, 2 (1997).

[21] J.-B. Moussy, S. Gota, a. Bataille, M.-J. Guittet, M. Gautier-Soyer, F. Delille, B. Dieny, F. Ott, T. Doan, P. Warin, P. Bayle-Guillemaud, C. Gatel, and E. Snoeck, Phys. Rev. B **70**, 174448 (2004).

[22] P. Weiss, J. Phys. Théorique Appliquée **6**, 661 (1907).

[23] W. Heisenberg, Zeitschrift Für Phys. **49**, 619 (1928).

[24] H. C. Stöhr, Joachim, Siegmann, *Magnetism: From Fundamentals to Nanoscale Dynamics* (Springer, 2006).

[25] S. Chikazumi and C. D. Graham, *Physics of Ferromagnetism* (Oxford University Press, 1997).

[26] L.-P. Lévy, *Magnetism and Superconductivity* (Springer, 2000).

[27] E. C. Stoner, Proc. R. Soc. A **154**, 656 (1936).

[28] E. C. Stoner, Proc. R. Soc. A **165**, 372 (1938).

[29] S. Blundell, *Magnetism in Condensed Matter* (Oxford University Press, 2001).

[30] K. H. Onnes, Comm. Phys. Lab. Univ. Leiden **120b**, (1911).

[31] W. Meissner and R. Ochsenfeld, Naturwissenschaften **21**, 787 (1933).

[32] D. Schoenberg, *Superconductivity* (Cambridge University Press, 1962).

[33] C. J. Gorter and G. B. Casimir, Phys. Z. **35**, 963 (1934).

[34] F. London and H. London, Proc. R. Soc. A Math. Phys. Eng. Sci. **149**, 71 (1935).

[35] V. L. Ginzburg and L. Landau, Zh. Eksp. Teor. Fiz. **20**, 1064 (1950).

[36] L. Landau and E. Lifshits, Phys. Zeitsch. Der Sow. **8**, 153 (1935).

[37] E. Maxwell, Phys. Rev. **78**, 477 (1950).

[38] C. A. Reynolds, B. Serin, and L. B. Nesbitt, Phys. Rev. **84**, 691 (1951).

[39] J. Bardeen, L. Cooper, and J. Schrieffer, Phys. Rev. **108**, 1175 (1957).

[40] J. Bardeen, L. N. Cooper, and J. R. Schrieffer, Phys. Rev. **106**, 162 (1957).

[41] L. N. Cooper, Phys. Rev. **104**, 1189 (1956).

[42] J. F. Annett, *Superconductivity, Superfluids, and Condensates* (Oxford University Press, 2004).

[43] J. R. Waldram, *Superconductivity of Metals and Cuprates* (Institute of Physics Publishing, 1996).

[44] M. Tinkham, *Introduction to Superconductivity* (Dover Publications, 2004).

[45] I. Giaever and K. Megerle, Phys. Rev. **122**, 1101 (1961).

[46] K. H. J. Buschow, *Concise Encyclopedia of Magnetic and Superconducting Materials* (Elsevier, 2005).

[47] E. L. Wolf, *Principles of Electron Tunneling SpectroscopySecond Edition* (Oxford University Press, 2011).

[48] J. Bardeen, Phys. Rev. Lett. **6**, 57 (1961).

[49] E. Burstein and S. Lundqvist, *Tunneling Phenomena in Solids* (Plenum Press, 1969).

[50] C. Cohen-Tannoudji, B. Diu, and F. Laloë, *Mécanique Quantique. Tome I* (Editions Hermann, 1997).

[51] P. A. M. Dirac, Proc. R. Soc. A Math. Phys. Eng. Sci. **114**, 243 (1927).

[52] R. B. Dingle, *Asymptotic Expansions: Their Derivation and Interpretation* (Academic Press, 1973).

[53] J. G. Simmons, J. Appl. Phys. **34**, 1793 (1963).
[54] W. F. Brinkman, R. C. Dynes, and J. M. Rowell, J. Appl. Phys. **41**, 1915 (1970).
[55] L. Esaki, Phys. Rev. **109**, 603 (1958).
[56] I. Giaever, Phys. Rev. Lett. **5**, 464 (1960).
[57] I. Giaever, Phys. Rev. Lett. **5**, 147 (1960).
[58] J. A. Appelbaum and W. F. Brinkman, Phys. Rev. B **2**, 907 (1970).
[59] R. C. C. Dynes, V. Na, V. Narayanamurti, and J. P. Garno, Phys. Rev. Lett. **41**, 1509 (1978).
[60] B. D. Josephson, Phys. Lett. **1**, 251 (1962).
[61] V. Ambegaokar and A. Baratoff, Phys. Rev. Lett. **11**, 104 (1963).
[62] P. A. M. Dirac, Proc. R. Soc. A Math. Phys. Eng. Sci. **117**, 610 (1928).
[63] N. F. Mott, Proc. R. Soc. A Math. Phys. Eng. Sci. **153**, 699 (1936).
[64] W. E. Pickett and J. S. Moodera, Phys. Today **54**, 39 (2001).
[65] R. Meservey and P. M. Tedrow, Phys. Rep. **238**, 173 (1994).
[66] J. Nogués and I. K. Schuller, J. Magn. Magn. Mater. **192**, 203 (1999).
[67] W. H. Butler, X.-G. Zhang, T. C. Schulthess, and J. M. MacLaren, Phys. Rev. B **63**, 54416 (2001).
[68] G.-X. Miao, G. Xiao, and A. Gupta, EPL **87**, (2009).
[69] T. Nagahama, Y. Matsuda, K. Tate, T. Kawai, N. Takahashi, S. Hiratani, Y. Watanabe, T. Yanase, and T. Shimada, Appl. Phys. Lett. **105**, 102410 (2014).
[70] L. Esaki, P. J. Stiles, and S. von Molnar, Phys. Rev. Lett. **19**, 852 (1967).
[71] A. Saffarzadeh, J. Magn. Magn. Mater. **269**, 327 (2004).
[72] T. S. Santos, J. S. Moodera, K. V. Raman, E. Negusse, J. Holroyd, J. Dvorak, M. Liberati, Y. U. Idzerda, and E. Arenholz, Phys. Rev. Lett. **101**, 147201 (2008).
[73] J. Moodera, X. Hao, G. Gibson, and R. Meservey, Phys. Rev. Lett. **61**, 637 (1988).
[74] P. LeClair, J. K. Ha, H. J. M. Swagten, J. T. Kohlhepp, C. H. van de Vin, and W. J. M. de Jonge, Appl. Phys. Lett. **80**, 625 (2002).
[75] T. Nagahama, T. Santos, and J. Moodera, Phys. Rev. Lett. **99**, 16602 (2007).
[76] R. Griessen, M. Landolt, and H. R. Ott, Solid State Commun. **9**, 2219 (1971).
[77] J. S. Moodera, R. Meservey, and X. Hao, Phys. Rev. Lett. **70**, 853 (1993).
[78] T. Santos and J. Moodera, Phys. Rev. B **69**, 241203 (2004).
[79] F. Natali, B. J. Ruck, N. O. V. Plank, H. J. Trodahl, S. Granville, C. Meyer, and W. R. L. Lambrecht, Prog. Mater. Sci. **58**, 1316 (2013).
[80] D. P. Schumacher and W. E. Wallace, J. Appl. Phys. **36**, 984 (1965).
[81] G. Busch, J. Appl. Phys. **38**, 1386 (1967).
[82] S. Granville, B. J. Ruck, F. Budde, A. Koo, D. J. Pringle, F. Kuchler, A. R. H. Preston, D. H. Housden, N. Lund, A. Bittar, G. V. M. Williams, and H. J. Trodahl, (n.d.).
[83] A. Pal, K. Senapati, Z. H. Barber, and M. G. Blamire, Adv. Mater. **25**, 5581 (2013).
[84] M. Bowen, M. Bibes, A. Barthélémy, J.-P. Contour, A. Anane, Y. Lemaître, and A. Fert, Appl. Phys. Lett. **82**, 233 (2003).
[85] M. Gajek, M. Bibes, A. Barthélémy, K. Bouzehouane, S. Fusil, M. Varela, J. Fontcuberta, and A. Fert, Phys. Rev. B **72**, 20406 (2005).
[86] T. Harada, I. Ohkubo, M. Lippmaa, Y. Sakurai, Y. Matsumoto, S. Muto, H. Koinuma, and M. Oshima, Phys. Rev. Lett. **109**, 76602 (2012).
[87] B. Prasad, M. Egilmez, F. Schoofs, T. Fix, M. E. Vickers, W. Zhang, J. Jian, H. Wang, and M. G. Blamire, Nano Lett. **14**, 2789 (2014).
[88] B. Prasad, W. Zhang, J. Jian, H. Wang, and M. G. Blamire, Adv. Mater. **27**, 3079 (2015).
[89] U. Lüders, M. Bibes, K. Bouzehouane, E. Jacquet, J.-P. Contour, S. Fusil, J.-F. Bobo, J. Fontcuberta, A. Barthélémy, and A. Fert, Appl. Phys. Lett. **88**, 82505 (2006).
[90] S. Matzen, J.-B. Moussy, R. Mattana, K. Bouzehouane, C. Deranlot, F. Petroff, J. C. Cezar, M. -a. Arrio, P. Sainctavit, C. Gatel, B. Warot-Fonrose, and Y. Zheng, Phys. Rev. B **83**, 184402 (2011).
[91] Y. K. Takahashi, S. Kasai, T. Furubayashi, S. Mitani, K. Inomata, and K. Hono, Appl. Phys. Lett. **96**, 72512 (2010).
[92] M. Foerster, D. F. Gutierrez, F. Rigato, J. M. Rebled, F. Peiro, and J. Fontcuberta, Appl. Phys. Lett. **97**, 242508 (2010).
[93] M. Foerster, D. F. Gutierrez, J. M. Rebled, E. Arbelo, F. Rigato, M. Jourdan, F. Peiró, J. Fontcuberta, F. Peiró, and J. Fontcuberta, J. Appl. Phys. **111**, 13904 (2012).
[94] F. C. Voogt, T. Fujii, P. J. M. Smulders, L. Niesen, M. A. James, and T. Hibma, Phys. Rev. B **60**, 11193 (1999).
[95] D. T. Margulies, F. T. Parker, M. L. Rudee, F. E. Spada, J. N. Chapman, P. R. Aitchison, and A. E. Berkowitz, Phys. Rev. Lett. **953**, 2 (1997).
[96] M. Ziese and H. J. Blythe, J. Phys. Condens. Matter **12**, 13 (2000).
[97] J. M. D. Coey, A. E. Berkowitz, L. Balcells, F. F. Putris, and F. T. Parker, Appl. Phys. Lett. **72**, 734 (1998).

[98] A. V Ramos, J.-B. Moussy, M.-J. Guittet, A. M. Bataille, M. Gautier-Soyer, M. Viret, C. Gatel, P. Bayle-Guillemaud, and E. Snoeck, J. Appl. Phys. **100**, (2006).
[99] A. V. Ramos, S. Matzen, J.-B. Moussy, F. Ott, and M. Viret, Phys. Rev. B **79**, 14401 (2009).
[100] W. Eerenstein, T. Palstra, T. Hibma, and S. Celotto, Phys. Rev. B **68**, 14428 (2003).
[101] D. Gilks, L. Lari, K. Matsuzaki, H. Hosono, T. Susaki, and V. K. Lazarov, J. Appl. Phys. **115**, (2014).
[102] S. Celotto, W. Eerenstein, and T. Hibma, Eur. Phys. J. B - Condens. Matter **36**, 271 (2003).
[103] Z. Szotek, W. Temmerman, D. Ködderitzsch, a. Svane, L. Petit, and H. Winter, Phys. Rev. B **74**, 174431 (2006).
[104] D. Johnston, H. Prakash, W. H. Zachariasen, and R. Viswanathan, Mater. Res. Bull. **8**, 777 (1973).
[105] D. C. Johnston, J. Low Temp. Phys. **25**, 145 (1976).
[106] J. Akimoto, Y. Gotoh, K. Kawaguchi, and Y. Oosawa, J. Solid State Chem. **96**, 446 (1992).
[107] R. J. J. Cava, D. W. W. Murphy, S. Zahurak, A. Santoro, and R. S. S. Roth, J. Solid State Chem. **53**, 64 (1984).
[108] S. Massidda, J. Yu, and A. J. Freeman, Phys. Rev. B **38**, 11352 (1988).
[109] S. Satpathy and R. M. Martin, Phys. Rev. B **36**, 7269 (1987).
[110] D. P. Tunstall, J. R. M. Todd, S. Arumugam, G. Dai, M. Dalton, and P. P. Edwards, Phys. Rev. B **50**, 16541 (1994).
[111] Y. Itoh, N. Moritsu, and K. Yoshimura, J. Phys. Soc. Japan **77**, 123713 (2008).
[112] P. W. Anderson, Phys. Rev. **102**, 1008 (1956).
[113] M. R. Harrison, P. P. Edwards, and J. B. Goodenough, J. Solid State Chem. **54**, 136 (1984).
[114] P. M. Lambert, P. P. Edwards, and M. R. Harrison, J. Solid State Chem. **89**, 345 (1990).
[115] M. Harrison, Philos. Mag. **52**, 679 (1985).
[116] P. Edwards, R. Egdell, I. Fragala, J. B. Goodenough, M. R. Harrison, A. F. Orchard, and E. G. Scott, J. Solid State Chem. **54**, 127 (1984).
[117] Y. Ueda, T. Tanaka, and K. Kosuge, J. Solid State Chem. **77**, 401 (1988).
[118] C. P. Sun, J.-Y. Lin, S. Mollah, P. L. Ho, H. D. Yang, F. C. Hsu, Y. C. Liao, and M. K. Wu, Phys. Rev. B **70**, 54519 (2004).
[119] E. Moshopoulou, J. Am. Ceram. Soc. **20**, 3317 (1999).
[120] T. Inukai, T. Inamura, N. Telegraph, and I. Introduction, Thin Solid Films **94**, 47 (1982).
[121] R. V. Chopdekar, F. J. Wong, Y. Takamura, E. Arenholz, and Y. Suzuki, Phys. C Supercond. **469**, 1885 (2009).
[122] A. Kumatani, T. Ohsawa, R. Shimizu, Y. Takagi, S. Shiraki, and T. Hitosugi, Appl. Phys. Lett. **101**, 123103 (2012).
[123] T. Oshima, K. Yokoyama, M. Niwa, and A. Ohtomo, J. Cryst. Growth **419**, 153 (2015).
[124] K. Jin, G. He, X. Zhang, S. Maruyama, S. Yasui, R. Suchoski, J. Shin, Y. Jiang, H. S. Yu, J. Yuan, L. Shan, F. V Kusmartsev, R. L. Greene, and I. Takeuchi, Nat. Commun. **6**, 7183 (2015).
[125] Y. Okada, Y. Ando, R. Shimizu, E. Minamitani, S. Shiraki, S. Watanabe, and T. Hitosugi, Nat. Commun. **8**, 15975 (2017).
[126] D. G. Schlom, L.-Q. Chen, X. Pan, A. Schmehl, and M. A. Zurbuchen, J. Am. Ceram. Soc. **91**, 2429 (2008).
[127] M. Opel, J. Phys. D. Appl. Phys. **45**, 33001 (2012).
[128] R. Eason, *Pulsed Laser Deposition of Thin Films Applications-Led Growth of Functional Materials* (Wiley-Interscience, 2007).
[129] H. M. Christen and G. Eres, J. Phys. Condens. Matter **20**, 264005 (2008).
[130] P. Eaton and P. West, *Atomic Force Microscopy* (Oxford University Press, 2010).
[131] T. J. Jackson and S. B. Palmer, J. Phys. D. Appl. Phys. **1581**, 1581 (1994).
[132] M. N. R. Ashfold, F. Claeyssens, G. M. Fuge, and S. J. Henley, Chem. Soc. Rev. **33**, 23 (2004).
[133] L. W. Martin, Y.-H. Chu, and R. Ramesh, Mater. Sci. Eng. R Reports **68**, 89 (2010).
[134] D. B. Chrisey and G. K. Hubler, *Pulsed Laser Deposition of Thin Films* (J. Wiley, 1994).
[135] W. L. Bragg, Proc. Camb. Philol. Soc. **17**, 43 (1913).
[136] B. D. Cullity and S. R. Stock, *Elements of X-Ray Diffraction*, Third Edition (Prentice-Hall, 2001).
[137] J. Daillant and A. Gibaud, *X-Ray and Neutron Reflectivity, Principles and Applications* (Springer, 2009).
[138] J. Als-Nielsen and D. McMorrow, *Elements of Modern X-Ray Physics* (Wiley, 2011).
[139] H. Kiessig, Ann. Phys. **402**, 769 (1931).
[140] B. Voigtländer, *Scanning Probe Microscopy : Atomic Force Microscopy and Scanning Tunneling Microscopy* (n.d.).
[141] I. Horcas, R. Fernández, J. M. Gómez-Rodríguez, J. Colchero, J. Gómez-Herrero, and A. M. Baro, Rev. Sci. Instrum. **78**, 13705 (2007).
[142] R. L. De Oliveira, D. a. C. Albuquerque, T. G. S. Cruz, and F. M. Leite, At. Force Microsc. - Imaging, Meas. Manip. Surfaces At. Scale 256 (2012).
[143] A. Einstein, Ann. Phys. (1921).
[144] M. Birkholz, *Thin Film Analysis by X-Ray Scattering* (Wiley-VCH Verlag GmbH & Co. KGaA, Weinheim, FRG, 2005).
[145] J. H. Lambert, *Photometria, Sive De Mensura Et Gradibus Luminis, Colorum Et Umbrae* (Leipzig : W. Engelmann, 1760).
[146] A. Beer, Ann. Der Phys. Und Chemie **162**, 78 (1852).

[147] M. P. Seah and W. A. Dench, Surf. Interface Anal. **1**, 2 (1979).
[148] C. R. Brundle and A. D. Baker, Surf. Interface Anal. **4**, (1982).
[149] J. Scofield, J. Electron Spectros. Relat. Phenomena **8**, 129.137 (1976).
[150] L. J. V. Van der Pauw, Philips Res. Reports **13**, 1 (1958).
[151] S. Kasap and P. Capper, *Springer Handbook of Electronic and Photonic Materials* (Springer, 2006).
[152] D. A. Glocker, S. I. Shah, and W. D. (William D. Westwood, *Handbook of Thin Film Process Technology* (Institute of Physics Pub, Bristol UK ;;Philadelphia, 1995).
[153] S. A. Campbell, *The Science and Engineering of Microelectronic Fabrication* (Oxford University Press, 2001).
[154] R. E. Somekh and Z. H. Barber, J. Phys. E. **21**, 1029 (1988).
[155] C. Bell, G. Burnell, D.-J. Kang, R. H. Hadfield, M. J. Kappers, and M. G. Blamire, Nanotechnology **14**, 630 (2003).
[156] M. C. Wu, a Aziz, J. D. S. Witt, M. C. Hickey, M. Ali, C. H. Marrows, B. J. Hickey, and M. G. Blamire, Nanotechnology **19**, 485305 (2008).
[157] D. C. Leitao, A. V Silva, R. Ferreira, E. Paz, F. L. Deepack, S. Cardoso, and P. P. Freitas, J. Appl. Phys. **115**, 17E526 (2014).
[158] M. Hirayama, K. Kim, T. Toujigamori, W. Cho, and R. Kanno, Dalton Trans. **40**, 2882 (2011).
[159] T. Dumont, T. Lippert, M. Döbeli, H. Grimmer, J. Ufheil, P. Novák, a. Würsig, U. Vogt, and a. Wokaun, Appl. Surf. Sci. **252**, 4902 (2006).
[160] S. Mesoraca, J. E. Kleibeuker, B. Prasad, J. L. MacManus-Driscoll, and M. G. Blamire, J. Cryst. Growth **454**, 134 (2016).
[161] NIST, Stand. Ref. Database Version 1.2 (2017).
[162] J. Sugiyama, H. Nozaki, I. Umegaki, K. Mukai, K. Miwa, S. Shiraki, T. Hitosugi, A. Suter, T. Prokscha, Z. Salman, J. S. Lord, and M. Månsson, Phys. Rev. B **92**, 14417 (2015).
[163] I. P. Kaminow, Appl. Phys. Lett. **22**, 326 (1973).
[164] J. R. Carruthers, I. P. Kaminow, and L. W. Stulz, Appl. Opt. **13**, 2333 (1974).
[165] D. L. Hildenbrand, W. F. Hall, and N. D. Potter, J. Chem. Phys. **39**, 296 (1963).
[166] Y. Ikeda, H. Ito, G. Matsumoto, and S. Nasu, J. Mass Spectrom. **27**, 263 (1979).
[167] J. J. Capponi, S. Billat, P. Bordet, B. Lambert-Andron, and B. Souletie, Phys. C Supercond. **185**–**189**, 2721 (1991).
[168] T. Inukai, T. Murakami, and T. Inamura, Jpn. J. Appl. Phys. **20**, L681 (1981).
[169] B. E. (Bertram E. Warren, *X-Ray Diffraction* (Dover Publications, 1990).
[170] D. C. Worledge, L. Miéville, T. H. Geballe, and L. Mié, J. Appl. Phys. **83**, (1998).
[171] P. C. Dorsey, P. Lubitz, D. B. Chrisey, and J. S. Horwitz, J. Appl. Phys. **79**, 6338 (1996).
[172] P. D. D. Thang, G. Rijnders, and D. H. A. H. A. Blank, J. Magn. Magn. Mater. **310**, 2621 (2007).
[173] J. Zhou, H. He, and C.-W. Nan, Appl. Surf. Sci. **253**, 7456 (2007).
[174] R. S. Hassan, N. Viart, C. Ulhaq-Bouillet, J. L. Loison, G. Versini, J. P. Vola, O. Crégut, G. Pourroy, D. Muller, and D. Chateigner, Thin Solid Films **515**, 2943 (2007).
[175] T. Li and P. Sheng, Phys. Rev. B **53**, R13268 (1996).
[176] K. Tsubouchi, I. Ohkubo, H. Kumigashira, Y. Matsumoto, T. Ohnishi, M. Lippmaa, H. Koinuma, and M. Oshima, Appl. Phys. Lett. **92**, 262109 (2008).
[177] G. P. Mambrini, E. R. Leite, M. T. Escote, A. J. Chiquito, E. Longo, J. A. Varela, and R. F. Jardim, J. Appl. Phys. **102**, 43708 (2007).
[178] T. Harada, I. Ohkubo, M. Lippmaa, Y. Sakurai, Y. Matsumoto, S. Muto, H. Koinuma, and M. Oshima, Adv. Funct. Mater. **22**, 4620 (2012).
[179] W. Prellier, P. Lecoeur, and B. Mercey, J. Phys. Condens. Matter **13**, R915 (2001).
[180] C. R. Cho, D. A. Payne, and S. L. Cho, Appl. Phys. Lett. **71**, 3013 (1997).
[181] X. Q. Xu, J. L. Peng, Z. Y. Li, H. L. Ju, R. L. Greene, and R. R. La, Phys. Rev. B **48**, 1112 (1993).
[182] W. M. Kaminsky, G. A. C. Jones, N. K. Patel, W. E. Booij, M. G. Blamire, S. M. Gardiner, Y. B. Xu, and J. A. C. Bland, Appl. Phys. Lett. **78**, 1589 (2001).
[183] S. A. Cybart, E. Y. Cho, T. J. Wong, B. H. Wehlin, M. K. Ma, C. Huynh, and R. C. Dynes, Nat. Nanotechnol. **10**, 598 (2015).
[184] L. Ozyuzer, J. F. Zasadzinski, C. Kendziora, and K. E. Gray, Phys. Rev. B **61**, 3629 (2000).
[185] A. Pal and M. G. Blamire, Phys. Rev. B **92**, 180510 (2015).
[186] S. I. Vedeneev and D. K. Maude, Phys. Rev. B **72**, 144519 (2005).
[187] L. Tang, P. Y. Zou, L. Shan, A. F. Dong, G. C. Che, and H. H. Wen, Phys. Rev. B **73**, 184521 (2006).
[188] F. S. Bergeret, A. Verso, and A. F. Volkov, Phys. Rev. B **86**, 60506 (2012).
[189] J. S. Moodera and G. Mathon, J. Magn. Magn. Mater. **200**, 248 (1999).
[190] K. Senapati, M. G. Blamire, and Z. H. Barber, Nat. Mater. **10**, 849 (2011).
[191] P. R. Hammar, B. R. Bennett, M. J. Yang, and M. Johnson, Phys. Rev. Lett. **83**, 203 (1999).
[192] W. Y. Lee, S. Gardelis, B.-C. Choi, Y. B. Xu, C. G. Smith, C. H. W. Barnes, D. A. Ritchie, E. H. Linfield, and J. A. C.

Bland, J. Appl. Phys. **85**, 6682 (1999).
[193] E. I. E. Rashba, Phys. Rev. B **62**, R16267 (2000).
[194] G. Schmidt, D. Ferrand, L. W. Molenkamp, A. T. Filip, and B. J. van Wees, Phys. Rev. B **62**, R4790 (2000).
[195] A. T. Filip, P. LeClair, C. J. P. Smits, J. T. Kohlhepp, H. J. M. Swagten, B. Koopmans, and W. J. M. de Jonge, Appl. Phys. Lett. **81**, 1815 (2002).
[196] S. Sugahara and M. Tanaka, Phys. E Low-Dimensional Syst. Nanostructures **21**, 996 (2004).
[197] S. Datta and B. Das, Appl. Phys. Lett. **56**, (1990).
[198] T. D. Nguyen, G. Hukic-Markosian, F. Wang, L. Wojcik, X.-G. Li, E. Ehrenfreund, and Z. V. Vardeny, Nat. Mater. **9**, 345 (2010).
[199] W. J. M. Naber, S. Faez, and W. G. van der Wiel, J. Phys. D. Appl. Phys. **40**, R205 (2007).
[200] Z. H. Xiong, D. Wu, Z. Valy Vardeny, and J. Shi, Nature **427**, 821 (2004).
[201] T. S. Santos, J. S. Lee, P. Migdal, I. C. Lekshmi, B. Satpati, and J. S. Moodera, Phys. Rev. Lett. **98**, 16601 (2007).
[202] V. A. Dediu, L. E. Hueso, I. Bergenti, and C. Taliani, Nat. Mater. **8**, 707 (2009).
[203] C. Barraud, P. Seneor, R. Mattana, S. Fusil, K. Bouzehouane, C. Deranlot, P. Graziosi, L. Hueso, I. Bergenti, V. Dediu, F. Petroff, and A. Fert, Nat. Phys. **6**, 615 (2010).
[204] D. Worledge and T. Geballe, J. Appl. Phys. **88**, 5277 (2000).
[205] Z.-W. Xie and B.-Z. Li, J. Appl. Phys. **93**, 9111 (2003).
[206] A. Saffarzadeh, J. Phys. Condens. Matter 3041 (2003).
[207] G.-X. Miao, M. Müller, and J. S. Moodera, Phys. Rev. Lett. **102**, 76601 (2009).